Millimeter-Wave Components and Antennas for Spatial and Polarization Diversity using PRGW Technology

Mohamed Mamdouh Mahmoud Ali

A Thesis

In the Department

of

Electrical and Computer Engineering

Presented in Partial Fulfillment of the Requirements

For the Degree of

Doctor of Philosophy (Electrical and Computer Engineering) at

Concordia University

Montréal, Québec, Canada

April, 2020

CONCORDIA UNIVERSITY

SCHOOL OF GRADUATE STUDIES

This is to certify that the thesis prepared

By: Mohamed Mamdouh Mahmoud Ali

Entitled: Millimeter-Wave Components and Antennas

for Spatial and Polarization Diversity using PRGW Technology

and submitted in partial fulfillment of the requirements for the degree of

Doctor of Philosophy (Electrical and Computer Engineering)

complies with the regulations of the University and meets the accepted standards with respect to originality and quality.

Signed by the final examining committee:

Chair

Dr. Roch Glitho

External Examiner

Dr.Yahia Antar

External to Program

Dr. Ali Nazemi

Examiner

Dr. Reza Soleymani

Examiner

Dr. Robert Paknys

Thesis Supervisor

Dr. Abdel Razik Sebak

Approved by:

Dr. Rastko Selmic, Graduate Program Director

May 24, 2018

Dr. Amir Asif, Dean, Faculty of Engineering & Computer Science

ABSTRACT

Millimeter-Wave Components and Antennas for Spatial and Polarization Diversity using PRGW Technology

Mohamed Mamdouh Mahmoud Ali, Ph.D.

Concordia University, 2020

The evolution of the wireless communication systems to the future generation is accompanied by a huge improvement in the system performance through providing a high data rate with low latency. These systems require access to millimeter wave (mmWave) bands, which offer several advantages such as physically smaller components and much wider bandwidth compared to microwave frequencies. However, mmWave components still need a significant improvement to follow the rapid variations in future technologies. Although mmWave frequencies can carry more data, they are limited in terms of their penetration capabilities and their coverage range. Moreover, these frequencies avoid deploying traditional guiding technologies such as microstrip lines due to high radiation and material losses. Hence, utilizing new guiding structure techniques such as Printed Ridge Gap Waveguide (PRGW) is essential in future mmWave systems implementation.

The main purpose of this thesis is to design mmWave components, antenna subsystems and utilize both in beam switching systems. The major mmWave components addressed in this thesis are hybrid coupler, crossover, and differential power divider where the host guiding structure is the PRGW. In addition, various designs for differential feeding PRGW antennas and antenna arrays are presented featuring wide bandwidth and high gain in mmWave band. Moreover, the integration of both the proposed components and the featured antennas is introduced. This can be considered as a significant step toward the requirements fulfillment of today's advanced communication systems enabling both space and polarization diversity. The proposed components are designed to meet the future ever-increasing consumer experience and technical requirements such as low loss, compact size, and low-cost fabrication. This directed the presented research to have a contribution into three major parts.

The first part highlights the feeding structures, where mmWave PRGW directional couplers and differential feeding power divider are designed and validated. These compo-

nents are among the most important passive elements of microwave circuits used in antenna beam-switching networks. Different 3-dB quadrature hybrid couplers and crossover prototypes are proposed, featured with a compact size and a wide bandwidth beyond 10 % at 30 GHz.

In the second part, a beam switching network implemented using hybrid couplers is presented. The proposed beam switching network is a 4 × 4 PRGW Butler matrix that used to feed a Magneto-electric (ME) dipole antenna array. As a result, a 2-D scanning antenna array with a compact size, wide bandwidth, and high radiation efficiency larger than 84 % is achieved. Further gain enhancement of 5 dBi is achieved through deploying a hybrid gain enhancement technique including AMC mushroom shapes around the antenna array with a dielectric superstrate located in the broadside direction. The proposed scanning antenna array can be considered as a step toward the desired improvement in the data rate and coverage through enabling the space diversity for the communication link.

The final activity is related to the development of high-gain wide-band mmWave antenna arrays for potential use in future mmWave applications. The first proposed configuration is a differential feeding circular polarized aperture antenna array implemented with PRGW technology. Differential feeding antenna designs offer more advantages than single- ended antennas for mmWave communications as they are easy to be integrated with differential mmWave monolithic ICs that have high common-mode rejection ratio providing an immunity of the environmental noise. The proposed differential feeding antenna array is designed and fabricated, which featured with a stable high gain and a high radiation efficiency over a wide bandwidth. Another proposed configuration is a dual-polarized ME-dipole PRGW antenna array for mmWave wireless communication. Dual polarization is considered one of the most important antenna solutions that can save costs and space for modern communication systems. In addition, it is an effective strategy for multiple-input and multiple-output systems that can reduce the size of multiple antennas systems by utilizing extra orthogonal polarization. The proposed dual- polarized antenna array is designed to achieve a stable gain of 15 ± 1 dBi with low cross- polarization less than -30 dB over a wide frequency range of 20 % at 30 GHz.

Acknowledgments

First and foremost, all praise and thanks are due to Allah for giving me the strength to keep trying, and for surrounding me with very supportive personals

I would like to express my deep gratitude to my supervisor, Dr. Abdel Razik Sebak for his guidance, patience, support, and invaluable comments.

Thanks, are also due to Dr.Yahia Antar, Dr. Robert Paknys, Dr. Ali Nazemi, Dr.Reza Soleymani, for their priceless comments and discussion during my defense presentation.

I would also like to thank Dr. Shoukry Shams and Dr. Mahmoud Elsaadany for their assistance through our fruitful collaboration.

In addition, I offer my love, regards and blessings to my mother, my father, my sister for their limitless support during the compilation of this work. Finally, I dedicate my work to my wife and my daughter for the great inspiration within the journey toward my degree.

To my beloved wife, Hend Ahmed Safwat Mahmoud,
To my daughter Almas Mohamed Mamdouh Mahmoud Ali,
and to my parents

Contents

List of Figures

List of Tables

List of Acronyms

mmWave	Millimeter Wave
ICTs	Information and Communication Technologies
2G	Second Generation
6G	Third Generation
4G	Fourth Generation
6G	Fifth Generation
IMT-A	International Mobile Telecommunications- Advanced
MIMO	Multiple-Input-Multiple-Output
LTE	Long-Term Evolution
HIRFCs	Highly Integrated Radio Frequency Circuits
IOT	Internet of Things
WRC	World Radiocommunications Conference
SNR	Signal-to-Noise Ratio
SIW	Substrate Integrated Waveguide
GW	Gap Waveguide
PRGW	Printed Ridge Gap Waveguide
CP	Circular Polarized
ME	Magneto-electric
2-D	Two-Dimensional
AMC	Artificial Magnetic Conductor
PMC	Perfect Magnetic Conductor
PEC	Perfect Electric Conductor

CST	Computer Simulation Technology
EBG	Electromagnetic Band Gap

Chapter 1

Introduction

1.1 Millimeter Wave Wireless Communication

Lately, there has been an expanding interest in Millimeter Wave (mmWave) antennas and components for use in short-range communications, future mmWave mobile communication, sensors networks, and imaging systems. The inventive and compelling utilization of Information and Communication Technologies (ICTs) is becoming progressively critical to enhancing the economy of the world. Wireless communication networks are the most basic element in the worldwide ICT strategy supporting numerous industries. It is one of the fastest developing and most unique parts of the world [2]. The advancement of wireless technologies has significantly enhanced different people's aspect of life through the ability to communicate and live in both business operations and social functions [3]. The remarkable achievement of wireless communications is reflected by the rapid pace of technology development. Start with the Second Generation wireless communication system launched in 1991 to the 3G system in 2001, the wireless communication has transformed from a traditional telephony system to a technology that supports high data rates with expanded capabilities [4]. The 4G wireless systems were designed to satisfy the requirements of International Mobile Telecommunications- Advanced (IMT-A) through using advanced techniques [5]. In 4G systems, an advanced radio interface is used for Multiple-Input-Multiple-Output (MIMO) with Orthogonal frequency-division multiplexing. The 4G wireless networks can support high data rates with faster signal transmission. Long-Term Evolution (LTE) is the development of 4G systems that have been deployed around the globe introducing higher capacity and enhanced wireless communication. Fourth generation (4G) networks have been reached the theoretical limit on the data rate and therefore are not adequate to accommodate the challenges such as the spectrum crisis and

high-energy consumption. In this way, we need breaking through wireless technologies to overcome the problems associated with existing technologies such as Fifth Generation (5G) wireless technology [4].

With the improvement of wireless communication technologies and its broad applications, wireless communication will have a significant value to society. They will provide people with a variety of fundamental and high-value communication services, which are the key driving force of the next wireless communication technology. These services would be attractive to industry and of great value to society. These services include healthcare, connected homes, self- driving, smart homes, entertainment, and other applications [6]. To achieve such demands, many of the industry initiatives identify a set of requirements for future wireless technology. One of the main requirements of the future technology is the low latency providing high-reliable and high-speed communication system enabling the development of new applications. Also, providing the services for connected devices in the presence of many concurrent users is important to improve the quality of life. Furthermore, maintaining high quality at high mobility will enable the successful deployment of advanced applications. Enhanced multimedia services through providing significantly higher data rates will be considered a major concern for future mobile communication systems [7].Therefore new mmWave bands are emerged as the availability of much wider bandwidth compared to microwave frequencies can achieve the previously mentioned requirements for future wireless technology [1]. In addition, mmWave frequencies offer the advantage of physically smaller antennas and components result in practically realized large-scale phased arrays at higher frequency bands due to the corresponding smaller wavelength. Although millimeter waves open more spectrum, there are technical challenges need to overcome, which will be summarized in the following section.

1.2 Millimeter Wave Challenges

Challenges are the inherent part of the new development; so, like all technologies, the next wireless generation has also key challenges that need to be tackled to achieve the requirements discussed in the previous section. Numerous challenges are addressed in the literature, which can be identified in the following. With the massive growth in mobile data demand, the future wireless network is expected to be a very versatile technology,

capable of providing the services with a high data rate to a large number of connected devices, while maintaining a high quality of services [8]. In addition, increasing the capacity of the network without significantly increasing the operating cost is considered a key challenge for future wireless technology. Moreover, the hardware architecture for implementing the future communication systems will be different depending upon the band of operation. Highly Integrated Radio Frequency Circuits (HIRFCs) are required for providing the necessary performance in the future communication frequency bands [9]. Furthermore, atmospheric attenuation due to oxygen absorption or heavy rain is a significant challenge to the mmWave communications [10]. Besides, these frequencies affect the use of traditional guiding technologies as they suffer from radiation and material losses, which limit their operation [11]. Due to the difficulties associated with mmWave frequencies, the International Telecommunications Union's (ITU) reached agreements and identified new spectrum to be studied [12, 13].

The future wireless technology will use three frequency ranges to provide a wide coverage area and support for all applications. These ranges are Sub-1 GHz, 1-6 GHz and above 6 GHz [7]. Sub-1 GHz will support widespread coverage across urban, suburban, and enable the Internet of Things (IoT) services. Moreover, the 1-6 GHz band offers a good mixture of coverage and capacity benefits. While above 6 GHz will be utilized to provide the ultra-high broadband speeds envisioned for the next wireless generation [1]. According to the latest World Radiocommunications Conference (WRC-19 in Sharm el-Sheikh, Egypt), this band has been identified as a mmWave band starting from 24 GHz up to 86 GHz [13]. These bands are divided into several sub-bands with different bandwidths as graphically shown in Fig. 1.1. These frequency bands are proposed to be studied for consideration as a potential range that meets the ultra-high-speed expected for mmWave technology. Therefore, to achieve great improvements in the performance of future wireless communication systems, different technological directions are independently emerging. There are many approaches for improving the system capacity and coverage such as beam switching and massive MIMO. Beam switching can increase the link signal-to-noise ratio (SNR) through the coherent addition of the signal transmitted from the antenna array resulting in increased capacity and coverage. While MIMO can enable space multiplexing results from the existence of multiple antennas in a system.

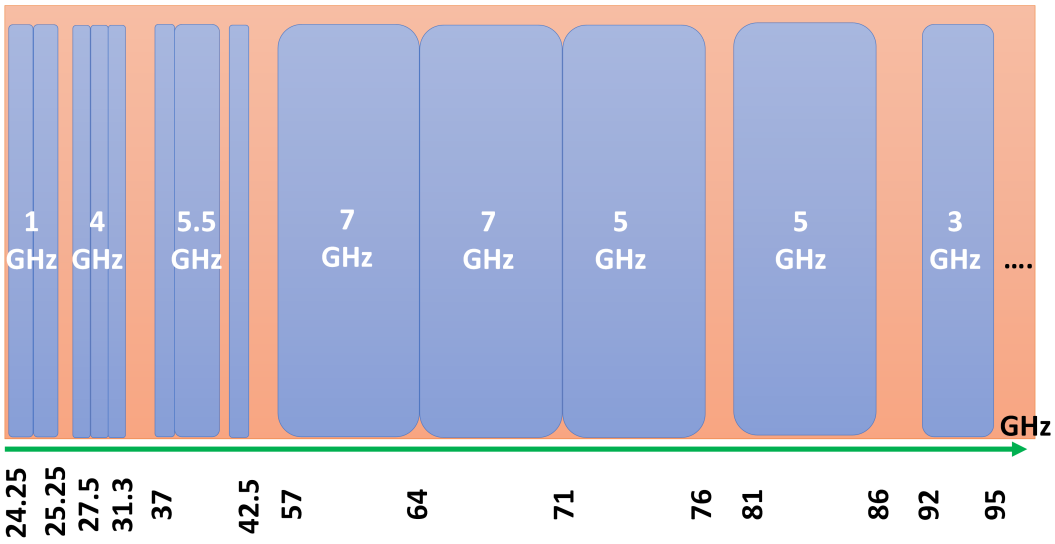

Figure 1.1: The expected frequency bands for mmWave research [1].

1.3 Motivation and Problem Statement

1.3.1 Motivation

The race for innovative solutions to enable the next generation era of wireless communications has recently featured and expanded all over the world. In early 2013, China is investing $180 billion in the development of future wireless technology by 2020 [14]. Three European leading universities are working collaboratively to bring the high-speed future wireless network into completion, namely, the University of Dresden in Germany, the Kings College of London, and the University of Surrey [15]. In addition, South Korea is quite aggressive to develop and deploy 5G systems investing $1.5 billion [14]. Once developed, the future wireless network will permit a peak data rate of 20 Gbit/s and 10 Gbit/s for downlink and uplink, respectively [16]. The future wireless communication network is expected to be roughly 10 times faster than an existing fourth generation and LTE networks [17]. In addition, low latency is expected to be lower than 4 ms that may be used in emerging applications such as self-driving cars, high-speed virtual reality videos, remote surgery and other tasks demanding quick response [16]. Furthermore, more capacity will be achieved, which means more devices will simultaneously be able to communicate enabling the Internet of Things (IoT). This can be accomplished by deploying different design approaches. One of them is enabling a space diversity, which provides simultaneous services to many connected devices [18]. This can be achieved by using a

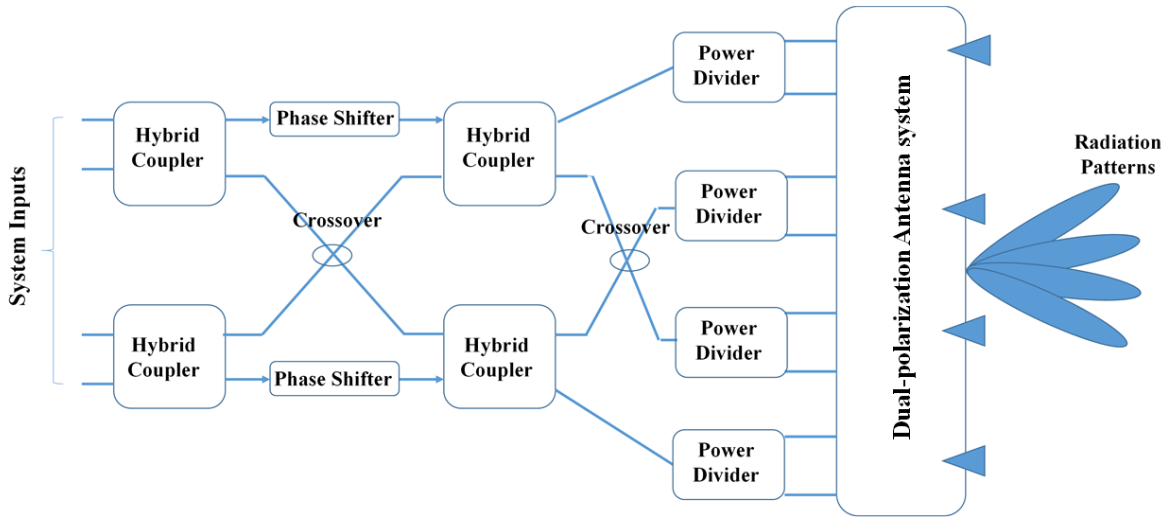

Figure 1.2: Block diagram of mmWave beam switching subsystem with polarization diversity.

smart and more cost-effective antenna array transceiver with beam steering capabilities. Another approach is deploying a massive MIMO system, which is one of the recommended techniques for future wireless communication systems that can increase spectral efficiency by using a very large number of transmit antennas [19]. However, utilizing many antennas will increase the size of the antenna array. Therefore, deploying a polarization diversity to implement a massive MIMO system is a cost-effective solution that can reduce the size of the MIMO system by providing extra orthogonal polarization [20, 21].

1.3.2 Problem Statement

The ultra-high-speed connections in the range of multi-gigabit per second could potentially be achieved through using an ultra-wide bandwidth system which may be implemented at higher frequency bands such as mmWave frequency band. These frequencies have been considered for the operation of the future wireless communication system. However, the aspects of the mmWave band pose several challenges as discussed in Section 1.2. Therefore, the utilization of a modern guiding structure to satisfy the future wireless technology requirements and match the continuous development of a communication system is necessary. Extensive work has been done in the literature to design mmWave components and antenna based on modern guiding structure such as Substrate Integrated Waveguide (SIW) [22, 23]. Although most of these designs have a low profile and a wide impedance bandwidth, they have a relatively high transmission loss and a low efficiency

of large mmWave structures. These losses result from the dielectric material where the wave propagates. Recently, several research groups have carried out research to implement mmWave components based on Gap Waveguide (GW) technology that achieved a high efficiency at the mmWave frequency band [24–26]. However, the main drawbacks are a narrow bandwidth, large profile, and high fabrication cost due to the tight associated fabrication tolerance. Therefore, a Printed Ridge Gap Waveguide (PRGW) technology has been introduced to overcome most of the previously mentioned challenges [27]. The use of this guiding structure to propose different types of mmWave components is considered a step toward the completion of future communications systems. These components should achieve compact size and a low loss as well as easy fabrication resulting in economic, energy-efficient, and high-performance components suitable for the massive future consumer market requirements. Although the implementation of mmWave components using PRGW technology has been recently introduced, they still need more development to match the requirement of future technology. Few mmWave components such as filters based on PRGW technology featured a wide bandwidth have been designed in the literature [27, 28]. However, other components such as hybrid directional couplers, crossover, and differential power dividers based on PRGW still need to be developed as they are essential components for scanning antenna array structures. In addition, several mmWave antennas based on PRGW technology featured a wide bandwidth and high gain have been designed and reported in the literature [29–31]. However, most of them are single-fed with linear or circular polarized.

The thesis work is focused on the design and implementation of several mmWave components and antennas that addressed the aforementioned drawbacks and challenges discussed in Section 1.2. In the first part of the thesis work, we are focused on the design and implementation of mmWave hybrid couplers and crossovers based on PRGW as they are essential components to implement beam switching networks as shown in Fig. 1.2. In addition, other components such as differential power dividers are presented as they are part of the feeding structure needed to realize and feed various types of antenna arrays. These components are designed to have superior characteristics including a compact size with wide bandwidth that can satisfy the requirements of the future wireless communication systems. Second, a compact size beam switching network is designed using hybrid couplers and integrated with antenna array to realize a beam scanning array. This ar-

ray features wide bandwidth, compact size, and high efficiency which can be considered as a valuable solution to enable the space diversity required for future communication technology. The third part is presented the differential feeding Circular Polarized (CP) antenna array based on PRGW. The antenna array is designed to be differentially fed that can be easily integrated with differential circuits having desirable characteristics such as high immunity toward environmental noise [32, 33]. Therefore, the deploying of differential circuits can be accomplished without the complexity that can introduce losses and lowers the radiation efficiency. In addition, being CP will improve the reliability of the communication link [34, 35]. Furthermore, the proposed antenna has a compact size with a high gain over a sufficient bandwidth. Finally, a wide bandwidth and high gain dual-polarized antenna based on PRGW is presented. A dual-polarized antenna is necessary for advanced wireless communication systems since it can reduce multipath fading losses, improves the reliability of the communication link and enables the development of massive MIMO antenna system [20, 36, 37].

1.4 Objective

The overall objective of this thesis is to design and implement mmWave components and antennas required to realize beam switching system such as shown in Fig. 1.2. This system will enable both space and polarization diversity to overcome the previously mentioned challenges associated with the future wireless communication systems. This objective is achieved by performing the following tasks:

- The first task is focused on the development of feeding structure, where practical mmWave hybrid directional couplers, crossovers, and differential power dividers are implemented with PRGW technology. The proposed components have improved performance featuring a wide bandwidth to provide a high data rate required for future wireless communication systems. Furthermore, the proposed compact size couplers enable the integration with other components and reduce the overall system cost. In addition, the proposed power divider is designed to provide an equal power division with a stable 180^o phase difference over a wide bandwidth. Such power dividers is allowed the realization of the antenna array with a stable gain over a wide bandwidth.

- In the second task, a PRGW beam switching feeding network to form a scanning antenna array is designed. A wide bandwidth and compact magneto-electric dipole antennas is developed for integration with the feed switching network. The beam switching network is designed using wide bandwidth hybrid couplers to achieve a compact size and high radiation efficiency scanning antenna array enabling the space diversity for future communication systems. In addition, several gain enhancement techniques are proposed to improve the antenna array gain and extend the coverage area.

- The third task is focused on the development of high gain and broadband mmWave antenna array. A circularly polarized antenna is designed, which is a good solution for reducing multipath fading problem as well as resilience to polarization mismatch due to misalignment between transmitting and receiving antennas. In addition, the proposed CP antenna is differentially fed instead of a single-ended fed for potential integration with differential mmWave monolithic ICs and enjoy low-noise, high-linearity, and large-dynamic range.

- Finally, a high gain and wide bandwidth dual-polarized antenna is designed, which is an attractive antenna solution to provide two orthogonal polarizations and reducing the size of the MIMO antenna system. Although mmWave frequencies can provide a huge bandwidth enough for high data rate applications, they are subject to high attenuation which limits the coverage range of operation. Therefore, to compensate for the losses in such higher frequencies, we are presented a design of antenna array featuring the previous characteristics with a high gain.

1.5 Contributions

The reported work in this thesis can be considered another step toward exploring and developing mmWave subsystems based on PRGW technology that's aimed to enable both space and polarization diversity for future wireless communication systems. Several prototypes of mmWave components and antenna subsystems are developed and resulted in five published articles [38–43]. The work contributions can be summarized as follows:

- **PRGW Hybrid Couplers**: to the best of our knowledge, two different prototypes for 3-dB hybrid couplers based on PRGW technology are designed for the first time in the literature. The main contribution of [39] is to introduce a coupling mechanism that provides a flat 3 dB forward coupling with superior electrical characteristics in the mmWave frequency band. This coupler improved the performance based on different design criteria, where a remarkable improvement in the performance is achieved compared with the work done in [38]. The proposed coupler in [39] is achieved a 26% relative bandwidth , which is more than four times the percentage bandwidth presented in [38]. Although this work shows a wide operating bandwidth, it has a relatively large size compared with the coupler designed in [38]. Therefore, another coupler is designed, which is focusing on achieving better performance with a compact size.

- **PRGW Crossover**: a prototype for a crossover device based on PRGW technology is provided for the first time in the literature [40]. The main contribution in [40] is to introduce the design and implementation of compact size and a wide bandwidth crossover for mmWave applications based on PRGW technology. The proposed crossover is achieved a compact size with a 13.33 % relative bandwidth and a matching and isolation level of -13.5 dB.

- **PRGW Beam Scanning Antenna Array**: Since the beam switching network based on PRGW technology has not been visited in the literature, a prototype of 2-D scanning magneto-electric (ME) dipole antenna array fed by PRGW technology Butler matrix is provided [41]. In this work, we are investigating the use of PRGW technology as low signal distortion, low loss, and wide bandwidth in a beam switching network can be achieved. The main contribution of this work is to introduce the design and implementation of a 2-D scanning antenna array fed by 4×4 PRGW butler matrix at mmWave bands. This PRGW butler matrix is used to feed a 2×2 ME dipole antenna array to construct a 2-D scanning antenna array features with a wide bandwidth of 20% and radiation efficiency higher than 84%.

- **PRGW Differential Fed Circularly Polarized Antenna Array**: a prototype of a differential feeding circular polarized antenna array implemented with PRGW technology is provided [42]. As the design of differential feeding circularly polarized

antenna based on PRGW technology is not addressed yet in literature, this work is focused on the design and implementation of PRGW differential feeding antenna array for future wireless communications at 30 GHz. Based on the requirements of the future communication system at 30 GHz, a differential-fed antenna array with CP radiation characteristics is designed, where a deep matching level over a 16% at 30 GHz is achieved. Furthermore, a 3 dB AR bandwidth over a 10% bandwidth is achieved, which is enough for future wireless applications at 30 GHz. Finally, a high gain of 14 dB with a 3-dB gain bandwidth of 16% is achieved.

- **PRGW Dual Polarized Antenna Array**: a prototype of a dual-polarized antenna implemented with PRGW technology is developed [43]. Although several mmWave antennas based on PRGW technology featured a wide bandwidth and high gain have been designed in the literature, however, most of them are linear or circular polarized. Therefore, a PRGW is adopted in the proposed work to implement a dual-polarized antenna for mmWave applications. The proposed antenna has a 20 % relative impedance bandwidth with isolation better than 20 dB at 30 GHz. In addition, the proposed antenna has achieved a gain of 10 dB with a stable radiation pattern over the operating bandwidth.

1.6 Thesis Organization

This thesis is organized in six chapters as follows: The literature review of guiding structures as well as the mmWave components implemented with these guiding structures is presented in Chapter two. Chapter three focuses on the design of PRGW directional couplers, where different designs of mmWave hybrid directional couplers and crossovers are presented. Chapter four presents the design of linear polarized 2-D scanning magneto-electric dipole antenna array fed by the PRGW Butler matrix implemented using PRGW directional coupler designed in Chapter three. While, chapter five presents different polarization antenna techniques, which include circular and dual-polarization. In chapter five, a differential feeding circularly polarized antenna array implemented with PRGW technology for mmWave applications is proposed. The same chapter also presents the design of a dual-polarized antenna based on PRGW. Chapter six concludes the results achieved in this thesis and summarizes the suggested future work.

Chapter 2

Literature Review

Microwave circuits and components have been increasingly adopted in many applications such as radio astronomy, long-distance communications, space navigation, radar systems, and medical equipment. As a result, the microwave industry paid considerable attention to develop the mmWave components to match the accelerating rate of microwave technology growth and communication system as well. The success of future wireless communications technology can be achieved through supporting high data rates by deploying diversity schemes as well as investigation of a new frequency band such as mmWave bands to provide more applications. Hence, the research community needs to develop more and more mmWave beam switching networks and its associated mmWave components such as couplers, dividers, crossover, and antennas. These microwave components can be implemented using a microwave guiding structure such as microchip line, stripline, rectangular waveguide, and modern technology as substrate integrated waveguide (SIW), packaged microstrip line, and ridge gap waveguide (RGW). The coming section will provide a review of the different types of microwave guiding structures. This is followed by a description of the state of art guiding structures which based on gap waveguide technology. Afterward, a brief review of the major components deployed in the beam switching networks is presented.

2.1 Microwave Guiding Structures

Electromagnetic guiding structures are fundamental components of the radio wave, microwave, and optical circuits [44]. The purpose of these structures is to guide the electromagnetic wave through a channel or a path with little attenuation. Understanding the principle operation of these guiding structure requires the excellent conception of the electromagnetic theory that was completely formulated by James Clerk Maxwell into four

equations describing the wave propagation. Wave equation was obtained by Helmholtz from the four Maxwell's equations, which is partial differential equation that govern the solutions of electromagnetic fields inside any guiding structure. Finding a unique solution to a partial differential equation cannot be done without applying the boundary conditions of the structure. Solving the wave equations will result in a full description of the electric and magnetic fields which come in the form of transverse electric (TE), transverse magnetic (TM), transverse electromagnetic (TEM) and hybrid models have both electric and magnetic field components in the direction of propagation. These solutions address the propagation of the wave inside many different guiding structures such as a rectangular waveguide, coaxial line, microstrip line, and stripline [45, 46].

Among all implementation technologies, the rectangular waveguide has superior electrical characteristics in terms of losses, power handling and compliance with international standard systems. Thus, this type of guiding structure is frequently deployed in many systems such as satellite communications and wireless transmit or receive radar systems. However, they can support only TE or TM mode which subjects to large dispersion. Moreover, the inability to be integrated with monolithic- microwave integrated circuits (MMICs). Furthermore, a complex process is required to assure good joints during the fabrication process. As a result, new types of printed microwave guiding structures using different technologies are investigated [24, 45, 46].

One of the modern guiding structure technologies is the microstrip line, which is cheaper, easier in fabrication, and supports a Q-TEM mode [45]. The benefit of TEM is that the media is non-dispersive, where the phase velocity and characteristic impedance are constants over a wide band. This means the signal will be transmitted through the guiding structure without distortion, which is preferred in communication systems [47]. However, at high microwave frequencies (30 GHz to 300 GHz), these traditional guiding structures suffer from high radiation and material loss which limits its applications. Therefore, a new guiding structure called a substrate integrated waveguide (SIW) has emerged.

SIW can be considered as a dielectric-filled waveguide but in printed form. Although this type of guiding structure has very small radiation losses compared to the microstrip line configuration, it carries a TE mode as it is very close to the traditional rectangular waveguide which leads to more signal distortion [24]. Moreover, the dielectric loss leads

to an unacceptable ohmic loss which considers a major drawback of this technology.

All the aforementioned challenges concerning microstrip and SIW technologies lead to discovering a new promising guiding structure for millimeter-wave application entitled gap waveguide technology. This guiding structure has a low loss, which results in developing components with featured characteristics [48].

2.1.1 Gap Waveguide Guiding Structures

Recently, artificial electromagnetic materials have been carefully studied and investigated in the literature. Such materials are often referred to metamaterials which exhibit properties not found in nature. One of the most desirable properties is to achieve an artificial magnetic conductor material, which is useful in many microwave components. The first conceptual attempt to realize magnetic conductivity (in the form of high surface impedance) was the so-called soft and hard surfaces. The concept of soft and hard surfaces realized by corrugated surfaces was introduced by Cutler in 1944 [49]. This concept based on the propagation along the corrugated surface that made up of parallel grooves, separated by metal walls as shown in Fig.2.1. The direction of the wave propagation relative to the direction of the corrugation determines whether it enables (hard surfaces) or prevents (stop surfaces) the wave propagation at the surface [50]. Nowadays, these corrugated surfaces most conveniently described as a periodic PEC/PMC surface. The PMC strips can be realized as metal grooves with effectively quarter-wavelengths depth. The soft surface is a kind of corrugation that stops the electromagnetic wave propagation. The reason behind this feature is that this kind of corrugation eliminates both the transverse electric field and the transverse magnetic field [24]. On the other hand, the hard surfaces allow waves of arbitrary polarization to propagate along the strips and eliminate only the longitudinal field components which result in the propagation of the only TEM mode. These kinds of surfaces are considered as a 1-D periodic structure where the PEC/PMC strips are repeated in one direction.

Other periodic structures implement the periodicity in two dimensions. These structures called Electromagnetic Band Gap (EBG) structures that stop wave propagation along its surface in a similar way as the soft surface but for all directions [24]. These structures prevent the wave propagation of all polarization and in all directions within the stopband that defined by the unit cell dimension. There is a different realization for

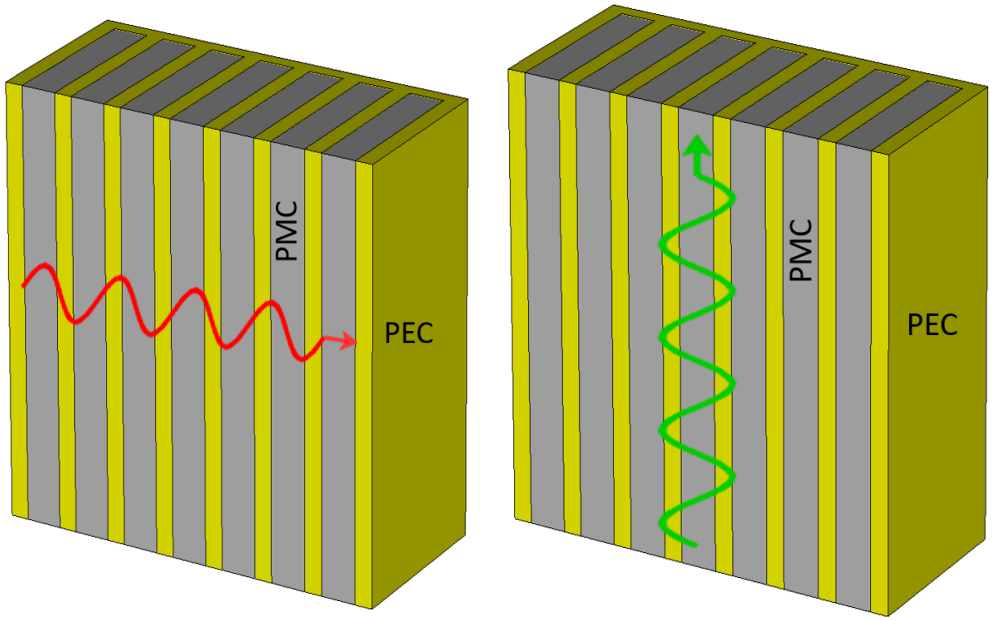

(a) (b)

Figure 2.1: Corrugated surfaces: (a) Soft surface. (b) Hard surface

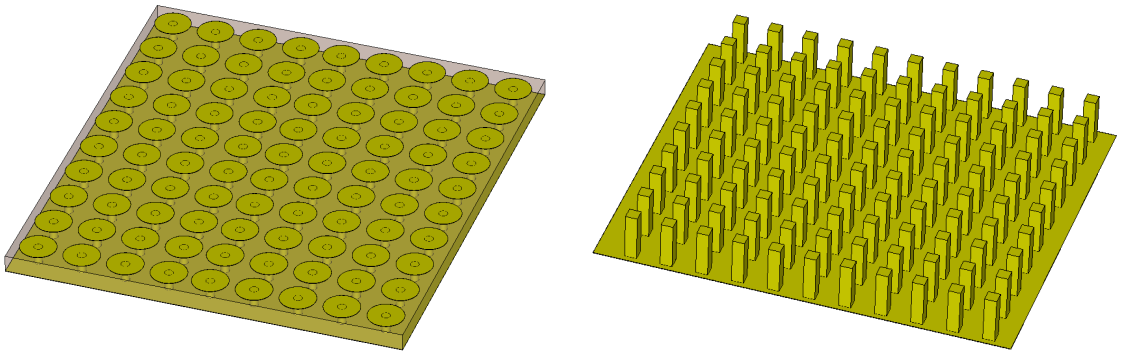

(a) (b)

Figure 2.2: Electromagnetic band gap structures: (a) Bed of nails. (b) mushroom-shape

EBG surfaces such as quarter wavelength bed of nails or mushroom-like EBG. Fig.2.2 shows several types of EBG surfaces.

Gap waveguides were introduced by Kildal in 2009 [51] as a quasi TEM guiding structure. This technology can be considered as an application of the soft and hard surfaces but in two-dimensional using periodic EBG structures. Firstly, gap waveguide can be realized by inserting a conducting ridge into the bed of nails structure bounded by the upper ground plate which referred to ridge gap waveguide (RGW) [52, 53]. These bed of nails forms an artificial magnetic (AMC) surface where a ridge located between the nails used to guide the signal [24, 54]. The basic geometry of the ridge gap waveguide is shown

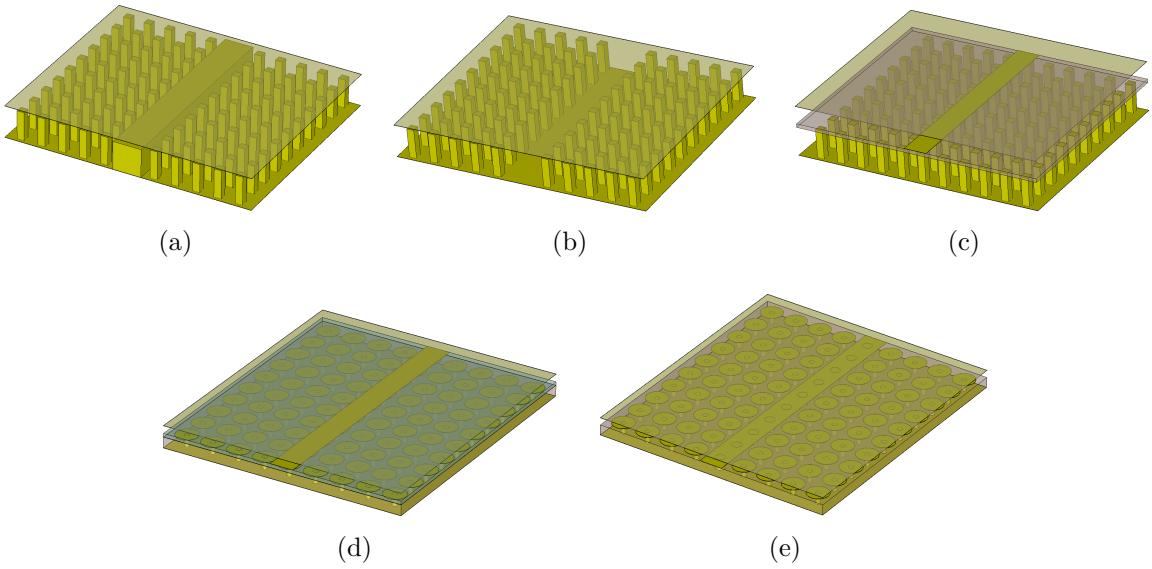

Figure 2.3: Gap waveguide structure: (a) Ridge gap waveguide. (b) Groove gap waveguide. (c) Inverted microstrip gap waveguide. (d) Inverted microstrip printed gap waveguide. (e) Printed ridge gap waveguide.

in Fig.2.3(a).

An analytic solution for the fundamental quasi-TEM mode of a ridge-gap waveguide is proposed in 2011 [55]. This analysis based on simplifying the complexity of the analysis of periodic structures by using appropriate boundary conditions. The basic assumption is that the periodicity of the considered structure approaches zero. By this, a simple and rigorous model suitable for the initial design of the structure can be obtained. This means that the properties of EBG structures, soft and hard surfaces, and gap-waveguide components can accurately be predicted in this way [56].

Other types of gap waveguides were proposed based on the same principle of RGW such as a groove gap waveguide (GGW) shown in Fig. 2.3(b). It considers as a rectangular waveguide between contactless metal plates [57]. With this structure, the different modes can be supported as a function of the cross-sectional dimensions of the groove, in the same way as in a conventional rectangular waveguide [58] . The bed of nails provides the cut-off of the parallel plate modes of the structure, and within this cut-off bandwidth, the allowed modes of the groove propagate [59]. As a result, the field is quite confined to the groove which some of these waveguides are manufactured sharing the same plates with high isolation.

Inverted microstrip gap waveguide (IMGW) [60] is considered as a development of RGW which based on the presence of a thin substrate that lies over the bed of nails

where the ridge is printed as shown in Fig.2.3(c). This gap waveguide technology can facilitate the design process since the arrangement of the bed of nails around the resonators and lines in RGW technology is complicated [27, 28]. On the other hand, the existence of a substrate will increase the losses and the size of the structure. Furthermore, the substrate layer above the nails adds more space between the bed of nails and the upper ground plate which results in decreasing the stopband [27, 61, 62]. Replacing the bed of nails with EBG mushroom structure to construct a printed type ridge gap waveguide is shown in Fig.2.3(d). This printed ridge gap waveguide (PRGW) enables the microwave components implemented based on RGW technology to be integrated easily with monolithic- microwave integrated circuits (MMICs) and fabricated using traditionally printed circuit board (PCB) techniques. The main drawback of this technology is the existence of a substrate will increase the losses [63, 64]. Also, the operating band (stopband) will be decreased since the substrate layer above the mushroom surface (and the pins) adds more space between the mushrooms (creating the high impedance condition) and the upper ground [61, 65]. Hence, another approach to overcome the previous challenges is that both mushrooms surface and microstrip line share the same substrate as shown in Fig .2.3(e). Although this guiding structure provides wider bandwidth and low loss, the circuit layout through alignment of the EBG units around the ridge will be complicated for complex designs.

Printed ridge gap waveguide shown in Fig.2.3(e) is considered one of the essential guiding structure technologies which used in this research work due to the recently reported advantages which can be summarized as:

- Enables the use of low cost printed circuit board (PCB) techniques.
- Supports the propagation of Q-TEM mode.
- Good electrical contact between the building blocks is not needed.
- The complexity in fabrication is reduced.
- Low loss at millimeter-wave frequencies.
- The ability to be integrated with monolithic- microwave integrated circuits (MMICs).

2.2 Beam Switching Butler Matrix Techniques and Components

The evolution of future communication technology will be through the improvement of the current technology, where new frequency bands below 6 GHz are attractive resources for future wireless communications [1, 7, 13]. On the other hand, the bands above 6 GHz are currently under study to test the viability of extending wireless services to support the exponentially growing demand in upcoming years. Furthermore, to meet the future wireless communication system requirements of more than 10 Gbps peak rate, two main techniques such as beam switching and MIMO are required. Beam switching can increase the signal-to-noise ratio (SNR) by pointing the transmitted power from the antenna array in any direction within a certain solid angle depending on the antenna pattern of the individual antenna elements. This not only can extend the range and coverage, but also reduce interference with other nearby transmissions [66]. Beam switching is an essential technique for different radio applications such as communications, surveillance, radar and, with different array sensors, in sonar and audio fields [19,67]. There are two types of beam switching, which can be categorized as analog and digital. In this section, we are focusing on analog beam switching, which can be classified into two main parts. One is an active beam switching system such as Phased Array Antenna (PAA) [68] and the other method is a passive beam switching system, which deploys passive components to implement passive beam switching networks.

2.2.1 Beam Switching Butler Matrix Techniques

Passive beam switching networks were introduced with many configurations, such as Blass matrices [69], Rotman lenses [70, 71], Nolen matrix [72] and Butler matrix [73]. Among all these types, the Butler matrix has a simple configuration which can be realized using a low number of components as shown in Fig. 1.2 [74–78]. In addition, it can be deployed to achieve two-dimensional beam scanning which can be realized using only directional couplers without any crossing which results in a compact structure with a wider coverage area [78]. Butler matrix can be implemented by traditional guiding structures such as microstrip lines and stripline [79, 80]. However, these guiding structures suffer from high material and radiation losses which greatly limits their usage at mmWave

frequency bands. Recently, the implementation of beam switching networks through deploying modern guiding structures such as SIW technology has attracted significant attention by the research community due to the ability to address the losses problems [74–77, 80]. Several realizations of Butler matrix using SIW have been proposed through the literature such as 1-D in [80], and 2-D switching beams [74–77]. Although these designs exhibited good performance in terms of bandwidth and radiation characteristics, they have a low radiation efficiency between 45% and 70% which may not be suitable for future applications.

On the other hand, few trails are performed to implement beam switching networks based on gap waveguide technology [81–84]. A Rotman lens with RGW technology is proposed in [83]. Although this lens shows a wide bandwidth performance, it needs a high fabrication tolerance that results in a much more expensive device. In [83], a multilayer inverted microstrip gap waveguide scanning antenna array based on Rotman Lens is reported. Although this design can cover a wide scanning range of $\pm 40^o$, it is a complicated structure implemented based on multilayer configuration. There aren't prototypes for all the previous mention Rotman lenses, where only simulated results are presented. Therefore, the investigation of beam switching networks based on other guiding structure including printed ridge gap waveguide deploying different techniques are necessary to satisfy the future communication system requirements. In the following, we will focus only on the passive mmWave components associated with the passive beam switching such as power dividers, directional couplers, crossovers, and antennas which can be implemented using different guiding structure.

2.2.2 Beam Switching Butler Matrix Components

Among all passive microwave components, directional couplers are essential components in microwave systems for power splitting, power combining, and measurement operations as they are one of the main components of a beam switching feeding network. The main purpose of these components is to extract a directive sample from the input power. They can be classified based on the coupling mechanisms as forward and backward couplers. They can be realized through a coupled line, branch lines, multi-hole, and patch configurations. They can be implemented using traditional guiding structures such as microstrip line [85–88], stripline [89], and rectangular waveguide [90, 91]. Also, they have been implemented based on modern guiding mechanisms such as substrate

integrated waveguides [92–98] which are suitable for high-frequency ranges. For example, traditional short-slot SIW hybrid couplers have been proposed in many articles before [96, 97]. They have an average size of $2.5\lambda_g \times 1.3\ \lambda_g$ with relative bandwidth between 3-13 % percentage bandwidth. In addition, the dominant mode is a TE mode, which has more dispersion. Furthermore, SIW has a large insertion loss which exceeds 1 dB due to dielectric losses [96]. Other coupler designs were introduced based on air-filled SIW (AFSIW) technology [93, 98]. In this case, the losses decreased closer to gap waveguide technology. The bandwidth is relatively wide which is exceeding 10 % at the expense of the complex fabrication process. Some other designs using RGW technology have been proposed to decrease the overall loss and support the signal transmission with minimal dispersion [99, 100]. In this design, the size of coupler is $1.6\lambda_g \times 1.6\ \lambda_g$ with a percentage bandwidth of 14%. Although this coupler achieves low loss and high-power handling, it has a big size and utilized an expensive fabrication process. Hence, it is difficult to integrate with a monolithic microwave integrated circuit. Based on PRGW technology, few trials have been presented in [101, 102]. Although the coupler presenting in [101] provides a 3-dB coupling over a wide bandwidth, it is implementing through multi-layer configuration that increases the size and the losses as well as the complexity of the design. Hence, it is not suitable to be integrated with a beam switching feeding network. A single layer PRGW coupler using a dielectric gap filled has been reported in [102]. In this design, the gap is filled with a dielectric to reduce the size of the coupler, however, more loss and limited performance are achieved. A microstrip ridge gap waveguide hybrid coupler at 60 GHz is reported in [63]. This coupler has a good phase imbalance 90 ± 2.5^o over a narrow bandwidth of 11 % with large insertion loss of 0.9 dB. There is still a chance to design a single layer, compact couplers, and wider bandwidth based on PRGW technology. In addition, they will have superior characteristics at higher frequency bands such as low loss since the wave propagates inside the air gap. Moreover, it supports a Q-TEM mode which results in minimum dispersion supporting wave propagation with minimal distortion.

Crossovers are essential components in any beam switching network for signal distribution and routing applications. They can be considered a 0-dB directional coupler that can be realized through many different configurations such as routing and multilayer configurations. Among all configurations, cascading two 3 dB hybrid couplers to realize a crossover is featured with simplicity and wide band of operation. Crossovers can be

implemented using traditional guiding structures such as microstrip line [103] as well as modern guiding mechanism such as substrate integrated waveguide [104–107] and packing microstrip line technology [108]. However, many of these designs suffer from either poor performance (i.e., narrow bandwidth, low isolation, large transmission loss and/or large size) or complex structure, which greatly limits their practical application use. Based on our knowledge, PRGW technology has been rarely used for crossover structures. One trail has been done to implement a crossover based on PRGW technology [109]. Although this design shows a wide bandwidth of operation of 26 %, it has a very large size with dimensions of $5.1\lambda_o \times 2.14\ \lambda_o$, where λ_o is the free space wavelength at 13 GHz. Hence, it is necessary to design, develop and test this device as it is an essential element in a beam switching feeding network.

Antenna are no less important as they are a necessary component of any wireless system. The main purpose of these components is to radiate and receive the input power. They were deployed in a variety of existing or future wireless communication networks such as wireless sensor networks, mobile communication systems, and wave automotive sensors. They were introduced in many configurations including wire antennas, slot antennas, microstrip patch antennas, dielectric resonator antennas, cavity antenna, and leaky-wave antennas [110–115, 118]. Much work has been done on the enhancement of the performance of the antenna in terms of bandwidth, multiband operation, size reduction, and the shaping of the radiation pattern [116–122]. Moreover, innovative antenna technologies, including dual-polarized antenna, differential feeding, and reconfigurable antennas have been presented to satisfy the future system requirements. Among all antenna technologies, differential feeding antennas are necessary to be easily integrated with differential mmWave monolithic ICs that enjoy low-noise, harmonic suppression, high-linearity, and large-dynamic range [123, 124]. Other advantages include low cross-polarization radiation, high polarization purity, and wide bandwidth [32, 125]. Recently, various differential feeding antenna designs have been reported in the literature which is either fed by traditional technologies such as microstrip line [126, 127] or modern technologies such as low-temperature cofired ceramic (LTCC) [128] and substrate integrated waveguide (SIW) [129, 130]. For example in [126], a 2× 2 patch antenna array is differentially fed using a rate race and power divider at 13 GHz, which achieved a 10-dB impedance bandwidth of 12.8% with a peak gain of 12.32 dB. A 4 × 4 differential-fed

patch antenna array using low-temperature cofired ceramic (LTCC) process was proposed in [128] at 60 GHz. The array is achieved impedance bandwidth of 11.7% with 18.62 dB and low aperture efficiency of 63%. In addition, some of the reported designs were shown a CP radiation capability at 60 GHz using a $\lambda_g/4$ height SIW opening-cavity structures, which were proposed in [129, 130]. In [129], an aperture antenna element with a rotationally symmetric windmill-shaped patch was proposed at 60 GHz, which achieved a 3-dB axial ratio (AR) bandwidth of 17.9% and a peak gain of 14.2 dB with a large aperture size of 2 $\lambda_o\times$ 1.8 λ_o. Although most of these designs having a wide impedance and axial ratio bandwidths with high gain at mmWave frequency bands, they are suffering from a relatively high transmission loss and low radiation efficiency due to the existence of dielectric where the wave propagates. On the other hand, feeding the antenna array using a printed ridge gap waveguide exhibited a large efficiency in many reported designs because the wave is propagating inside the air gap instead of dielectric as in other technologies [57, 131–136]. Another antenna technology that is very necessary for the future communication systems is a dual-polarization. The dual-polarized antenna is considered an effective antenna technique for the MIMIO system as a size reduction in the array size can be achieved through providing two orthogonal polarizations [21]. This gives dual polarization antennas a major advantage compared to spatially separated single-polarized ones. Other advantages include improvement for the communications link by reducing the multi-path fading loss and enabling the polarization diversity [20, 37]. Recently, various dual-polarized antenna designs have been investigated in the literature, which are implemented based on microstrip line, Substrate Integrated Waveguide (SIW) technologies, and Low-Temperature Co-fired Ceramics (LTCC) [137–140]. Although most of these designs have a low profile, wide impedance, and isolation bandwidth, they have a relatively high transmission loss and low efficiency of mmWave large array structures. These losses result from the existence of dielectric material where the wave propagates. On the other hand, few works have been done in the literature to implement dual-polarized antenna based on Gap Waveguide (GW) technology that achieved a high efficiency at the mmWave frequency band. However, the main drawbacks are a narrow bandwidth, large profile, and high fabrication cost due to the great fabrication tolerance needed [139, 140]. Therefore, PRGW technology has been deployed several times in the literature to overcome these challenges. Based on our knowledge, several mmWave antennas based on PRGW tech-

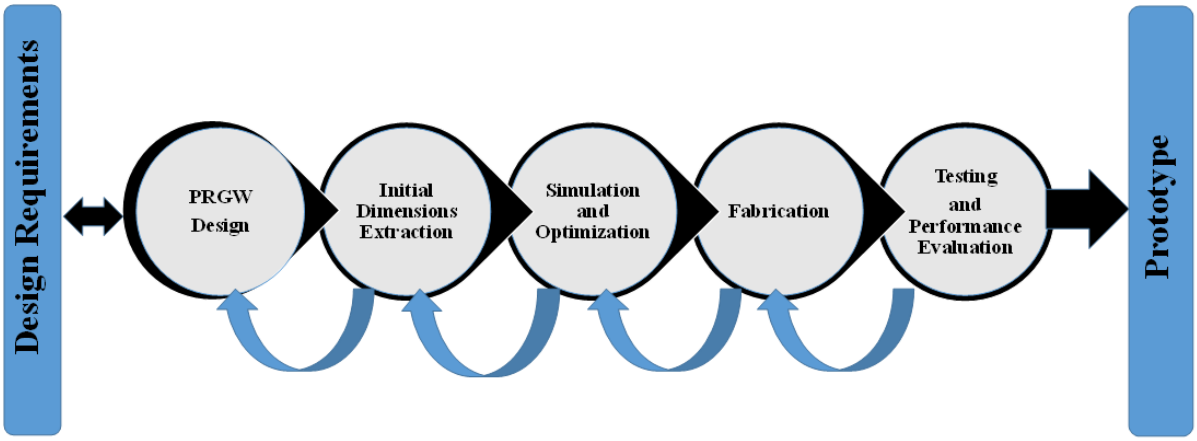

Figure 2.4: Thesis research methodology flow chart.

nology featured a wide bandwidth and high gain have been designed in the literature, however, most of them are linear or circular polarized [29–31].

2.3 Research Methodology

According to the previously discussed literature review, several mmWave components and antennas are still needed to be developed and designed based on a modern guiding structure such as printed ridge gap waveguide. This type of guiding structure has been used by the research society as it has superior characteristics at mmWave frequencies. Therefore, the following chapters will propose the design, implementation, and fabrication of essential mmWave components and antennas for future short-range and high-speed mmWave applications. These components will be implemented based on PRGW technology, where a common methodology is adopted to realize them, while detailed design procedure for each component will be presented in the following chapters. The common methodology is demonstrated in Fig. 2.4 and described as follow:

- **Design Requirements**: a 30 GHz is considered as the center operating frequency for all the designed components, where the target relative bandwidth is larger than 10 %.

- **PRGW Design**: the PRGW guiding structure is realized by designing the EBG unit cell operating at 30 GHz. The design of the EBG unit cell is performed using the Computer Simulation Technology (CST) Microwave Studio Eigenmode Solver [141]. This unit cell is printed on a substrate with a certain thickness and proper

dimensions to cover more than 10% bandwidth. Two types of substrate (Rogers RT6002 and RO 3003) are used in the thesis work, which is recommended by the fabrication agency.

- **Initial Dimensions Extraction**: detailed design procedures and guidelines in the subsequent chapters are used for each component to determine the initial dimensions.

- **Simulation and Optimization**: the simulation of the proposed components is performed using the CST, which is a high performance 3D EM analysis software for designing, analyzing and optimizing electromagnetic (EM) components and systems. Different CST solvers are used for simulation such as time domain and frequency domain. Time domain solver is based on the finite integration technique (FIT), where the Maxwell equations are numerically solved in their integral form. While frequency domain is solving numerically Maxwell equations in their differential form based on finite element method (FEM). The proposed components have been constructed using CST, where several parametric studies are performed using time domain solver to obtain preliminary results.

- **Fabrication**: the proposed components are fabricated using a standard Printed Circuit Board (PCB) process, where different layers are assembled and aligned together using plastic screws or glue with thermal pressure. A 2.92 mm end launch connectors are used to allow the connection between the device under test and the measurement equipment interface.

- **Testing and Performance Evaluation**: the S-parameters are measured using an N52271A phase network analyzer, where the gain and radiation pattern measurements were performed in the anechoic chamber system. These measurement setups are shwon in Fig. 2.5. The performance of the designed components is evaluated through a comparison between Both measurement and simulated resulted.

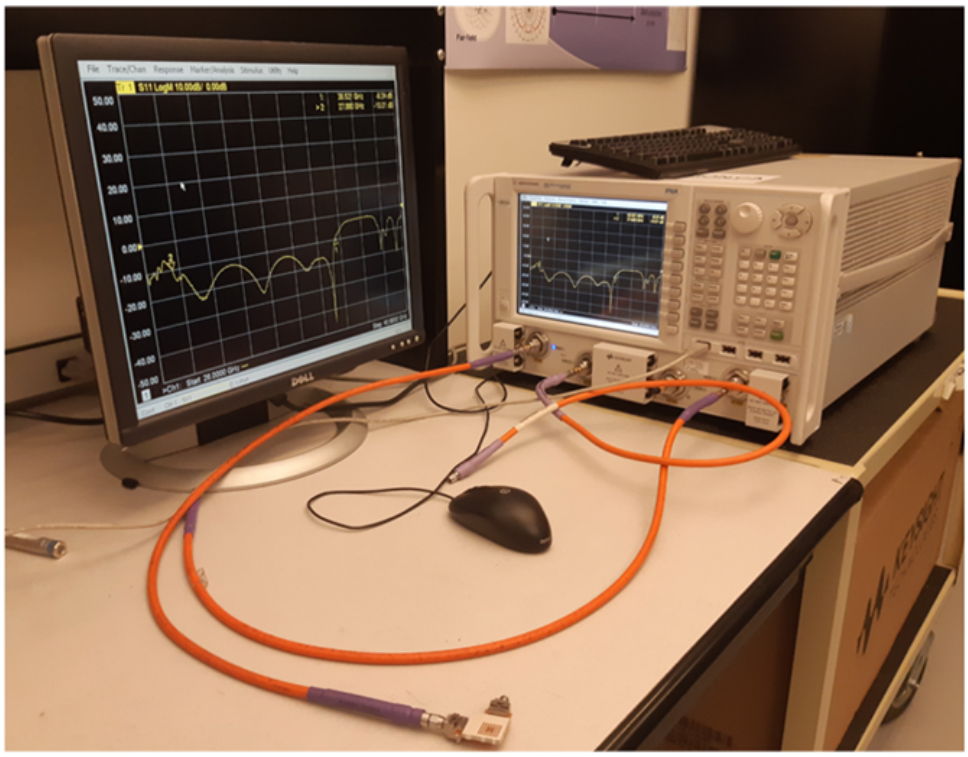

(a)

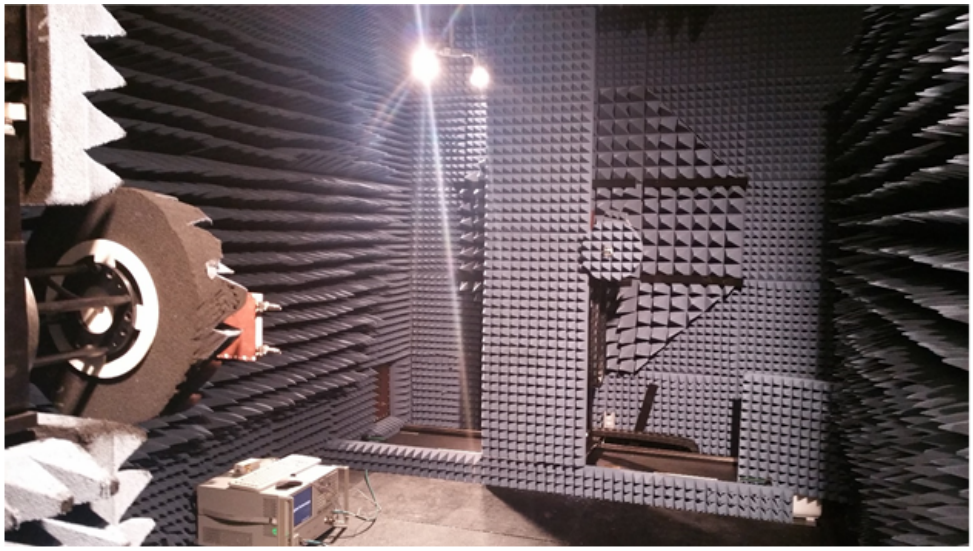

(b)

Figure 2.5: Measurement setups. (a) N52271A phase network analyzer. (b) Anechoic chamber system

Chapter 3

Millimeter Wave PRGW Hybrid Directional Coupler and Crossover

Communication systems are witnessing an outstanding revolution that has a clear impact on all aspects of life. The world technology is drifting towards high frequency and data rate solutions to accommodate future expansion in wireless applications. The future technology will offer advanced features in the mmWave frequency band which requires intelligent subsystems such as beam switching. Therefore, the microwave components, specially couplers, still need a significant improvement to follow the rapid variations in future technologies. Quadrature 3-dB hybrid microwave directional couplers are among the most important category of passive microwave circuits. The main purpose of these components is dividing or combining signal with appropriate phase as they are deployed in microwave smart beam switching subsystems. Beam switching networks are considered an important subsystem in the realization of the future wireless communication system. They are used specifically to improve the quality and reliability of the wireless communication through the improvement of the signal to noise ratio of the communication link. Another essential component required to realize the beam switching network is a crossover. Being low loss, wide bandwidth, and compact size will improve the performance of beam switching subsystems. Although the implementation of mmWave components using PRGW technology has been recently introduced, they still need more development to match the requirement of future technology. Few mmWave components based on PRGW technology featured a wide bandwidth have been designed in the literature. However, other components such as hybrid directional couplers and crossover based on PRGW still need to be implemented as they are essential components for scanning antenna array structures.

In this chapter, several feeding structure components such as couplers and crossovers are designed and validated based on PRGW technology. Two different prototypes for

3-dB hybrid couplers based on PRGW technology are proposed. The mathematical formulations and a systematic design procedure of the proposed couplers are presented. The proposed design approach is used to achieve a compact low-loss PRGW hybrid couplers able to cover wide bandwidth at 30 GHz. Also, a design of crossover based on PRGW technology is presented. The proposed crossover has a compact size and designed to cover a wide relative bandwidth and sufficient isolation levels. The proposed components are fabricated and tested where the measured and simulated are in good agreement.

•

3.1 Ultra-Wideband PRGW Hybrid Coupler

3.1.1 Mathematical Formulation for Coupling Structure

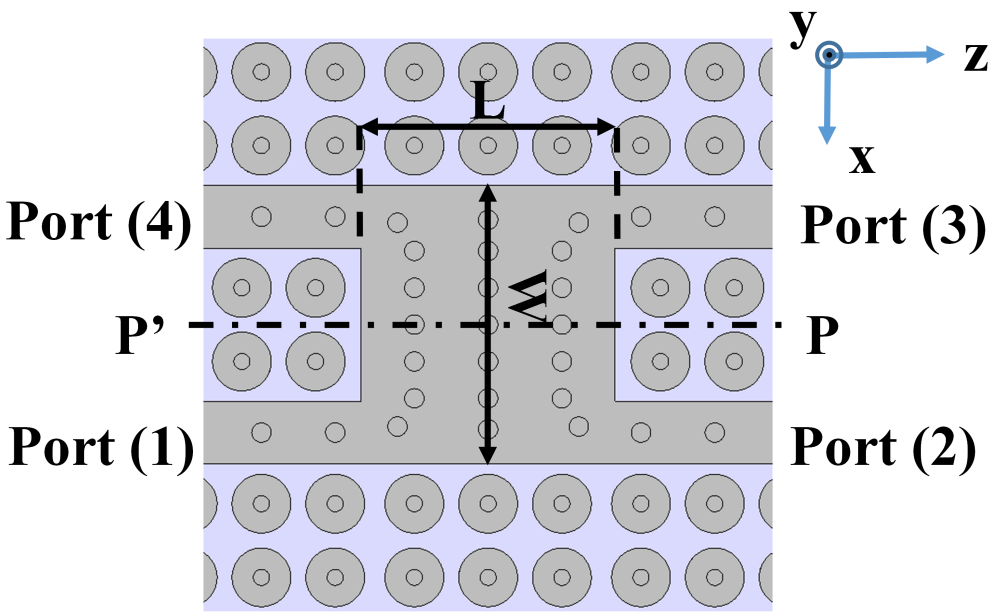

Figure 3.1: Configuration of a four-port rectangular-junction circuit.

Starting with the fact that any arbitrary junction connecting four transmission lines and satisfying certain conditions can work as a directional coupler [86,142,143]. Figure 3.1 shows a schematic of a four-port rectangular-junction structure with width W and length L. Since this circuit is symmetrical about the plane PP', it can be analyzed through the even/odd mode analysis methodology. Due to the symmetrical and reciprocal nature of our component, the elements of the scattering matrix of the four-port networks, shown in Figure 3.1, are given as follow [47]:

$$S_{11} = \frac{S_{11}^e + S_{11}^o}{2} \tag{3.1}$$

$$S_{21} = \frac{S_{21}^e + S_{21}^o}{2} \tag{3.2}$$

$$S_{31} = \frac{S_{21}^e - S_{21}^o}{2} \tag{3.3}$$

$$S_{41} = \frac{S_{11}^e - S_{11}^o}{2} \tag{3.4}$$

where S_{11}^e and S_{11}^o represent the reflection coefficients for the even and odd modes, respectively, while S_{21}^e and S_{21}^o are the transmission coefficients for the even and odd modes, respectively. The circuit can be completely matched under two possibilities. The first one is $S_{11}^e = S_{11}^o = 0$ and the second is $S_{11}^e = -S_{11}^o \neq 0$. Thus, if the field distribution in the connected junction satisfies one of the matching conditions, by optimizing the circuit parameters we can have a directional coupler.

Considering the first condition, $S_{11}^e = S_{11}^o = 0$, this leads to having internally matched network at the four ports, where S_{ii}=0, for i=1,2,3 and 4. Moreover, substituting in Equation 3.4, no coupling occurs between ports 1 and 4, implying that $S_{14} = S_{41} = 0$. Similarly, ports 2 and 3 will be decoupled. This means that the coupler works in the forward coupling mode, which is the objective design in this work. Hence, S_{11}^e and S_{11}^o can be given as follow [142]:

$$S_{11}^e = \frac{Z_{in}^e - Z_o}{Z_{in}^e + Z_o} \tag{3.5}$$

$$S_{11}^o = \frac{Z_{in}^o - Z_o}{Z_{in}^o + Z_o} \tag{3.6}$$

$$\tag{3.7}$$

where, Z_{ine} and Z_{ino} are the input even and odd impedances, respectively, which can be found as:

$$Z_{in}^e = Z_o^e \frac{Z_o + jZ_o^e tan(\Phi^e)}{Z_o^e + jZ_o tan(\Phi^e)} \tag{3.8}$$

$$Z_{in}^o = Z_o^o \frac{Z_o + jZ_o^o tan(\Phi^o)}{Z_o^o + jZ_o tan(\Phi^o)} \tag{3.9}$$

where,Z_o^e and Z_o^o are the even and odd mode characteristics impedances for the rectangular junction, respectively, while Z_o is the characteristics impedance of the connected PRGW line and $\Phi^e = \beta^e L$ and $\Phi^o = \beta^o L$, where β^e and β^o represent the propagation constants of the even and odd mode signal. Therefore, the forward wave coupling condition $S_{11}^e = S_{11}^o = 0$ can be satisfied if $Z_o^e = Z_o^o = Z_o$, independently of coupling section length L.

Considering both the even mode and the odd mode, we have no reflection as $S_{11}^e = S_{11}^o = 0$. As a result, the magnitude of the transmission coefficient will be equal to unity $\mid S_{21}^e \mid = \mid S_{21}^o \mid = 1$, where the circuit is lossless. Hence, in both cases the only difference will be the phase shift, where $S_{21}^e = e^{-j\Phi^e}$ and $S_{21}^o = e^{-j\Phi^o}$. Hence, by using (3.2) and (3.4), the scattering parameters of an ideal forward-wave directional coupler are given as follow:

$$S_{21} = \frac{e^{-j\Phi^e} + e^{-j\Phi^o}}{2} \tag{3.10}$$

$$S_{31} = \frac{e^{-j\Phi^e} - e^{-j\Phi^o}}{2} \tag{3.11}$$

Thus, the following equation can be derived:

$$S_{21}/S_{31} = -jcot(\frac{\Phi}{2}) \tag{3.12}$$

where, $\Phi = (\beta^e - \beta^o)L$. The above equation indicates that the phase difference between two outputs equals 90° , and the power-split ratio depends on Φ. In addition, the condition for equal power splitting is Φ equal to $\pm 90^\circ$.

The even and odd characteristics impedances for a four-port rectangular-junction integrated into PRGW environment are calculated through applying the magnetic wall (even mode) and the electric wall (odd mode) at the plane of symmetry PP'. These impedances are calculated using V/I model as the line impedance can be calculated by $Z = V/I$, where $V = \int E_y dy$ and $I = \int H_x dx$ are the voltage and current in the transverse plane defined by $x - y$ plane. Several E and H-field probes are located along a section of PRGW line and after integrating the fields by using the CST post processing we can obtain the impedance for the whole frequency band of interest. Figs. 3.2(a) and 3.2(b) show the

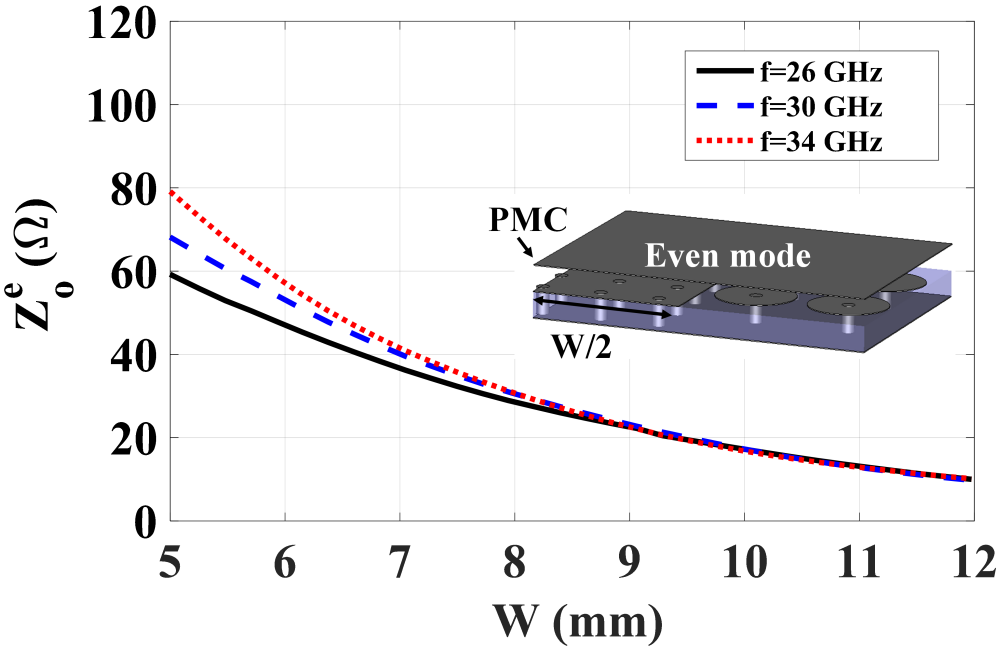

(a)

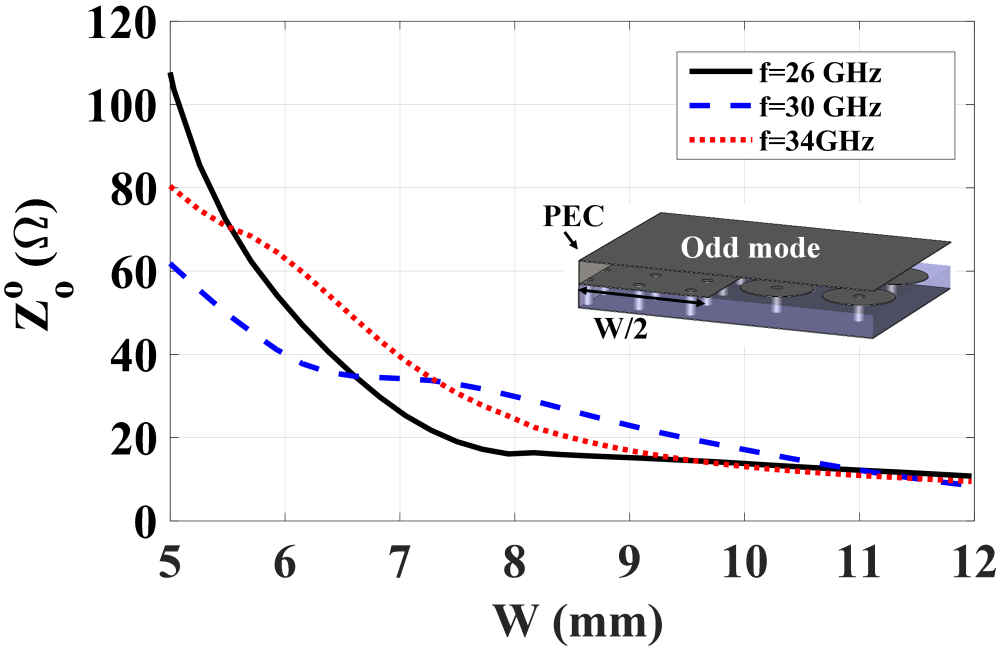

(b)

Figure 3.2: Mode analysis of the proposed PRGW hybrid coupler. (a) Even mode impedance. (b) Odd mode impedance.

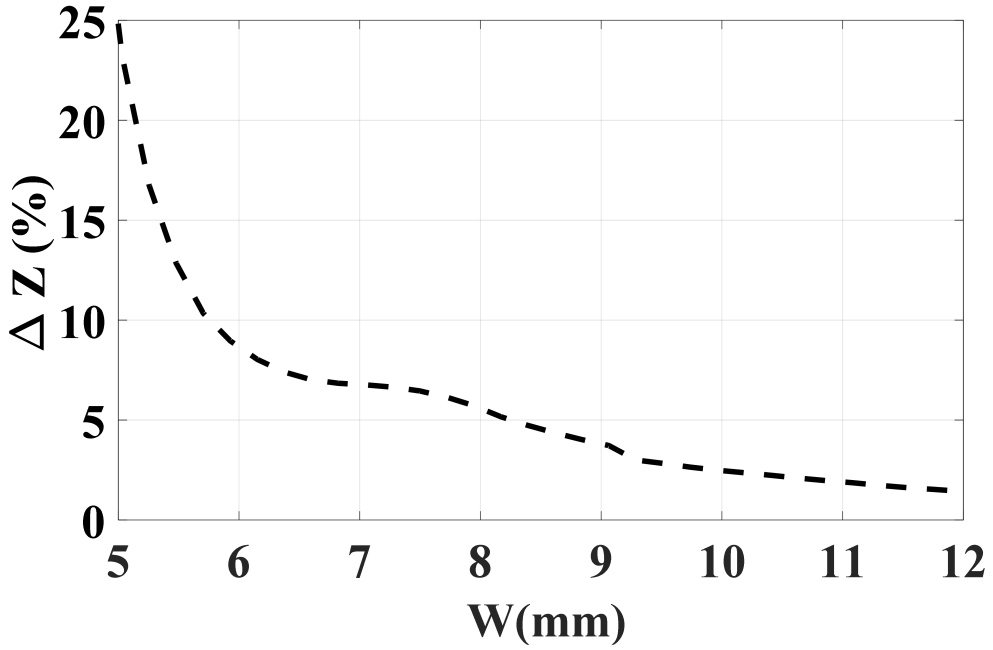

(a)

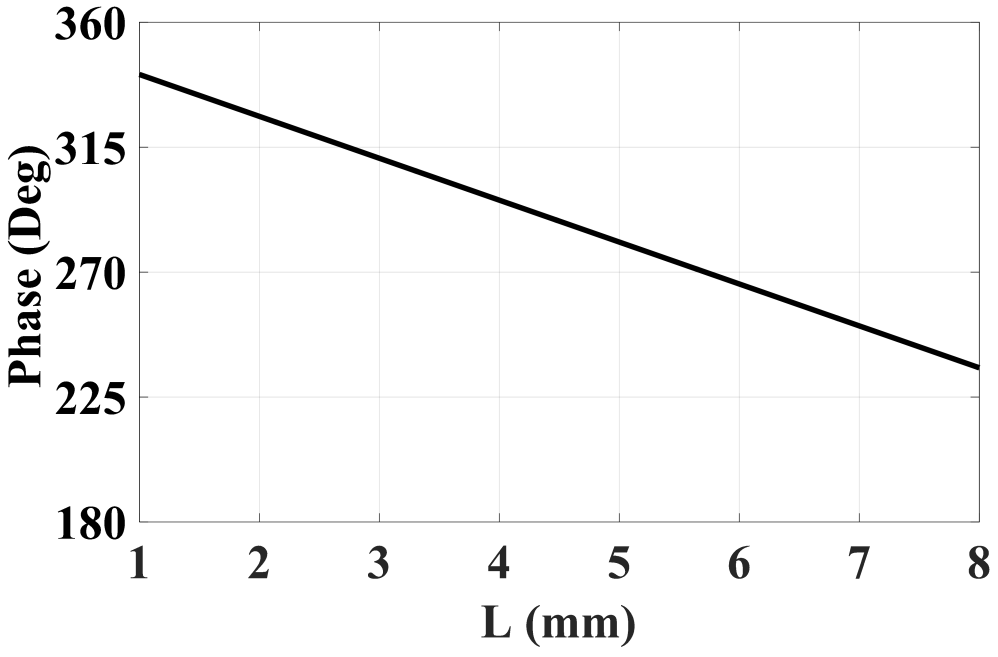

(b)

Figure 3.3: (a) Percentage error. (b) Phase difference between the propagation phase of the even and odd mode signal.

even and odd mode characteristics impedance for various coupling section width W over the frequency band of operation. Hence, for wide band operation, the width W should be selected to satisfy that Z_o^e and Z_o^o are very close over the whole frequency band of operation. Hence, the percentage impedances differences ΔZ between the even and odd mode characteristics impedance is plotted versus the coupling section width W in Fig.3.3(a). The coupling section width W= 8 mm is selected as initial value, where the percentage differences exactly goes below 5%. Applying the even and odd mode analysis, the phase difference Φ in the propagating phase of the even and odd mode are calculated for different coupling section length and at the center frequency of 30 GHz which is plotted in Fig. 3.3(b). It can be noticed that the 90° phase difference can be achieved at L= 5.9 mm. Hence, the dimensions obtained through the even and odd mode analysis for the coupling section W =8 mm and L = 5.9 mm are considered as initial values for the realization of the proposed coupler.

3.1.2 Design Procedure and Simulation Results

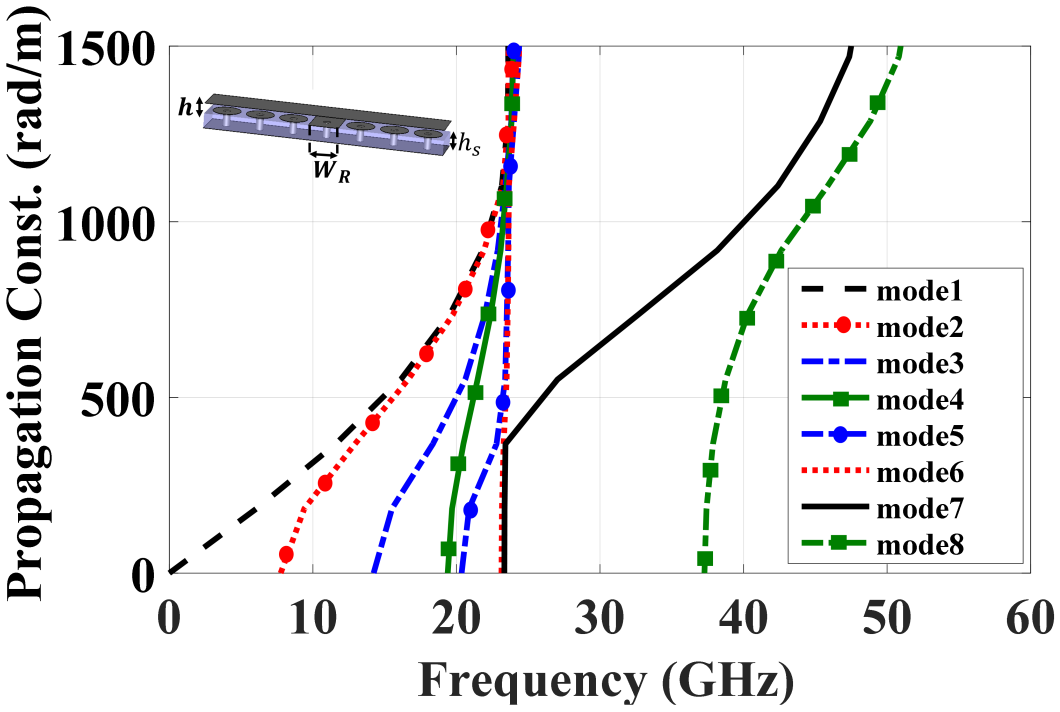

Figure 3.4: Dispersion diagram of PRGW section.

The design of a printed ridge gap waveguide and the EBG unit cell have been well studied in the literature [27,28,144]. The EBG unit cell used to design the PRGW feeding

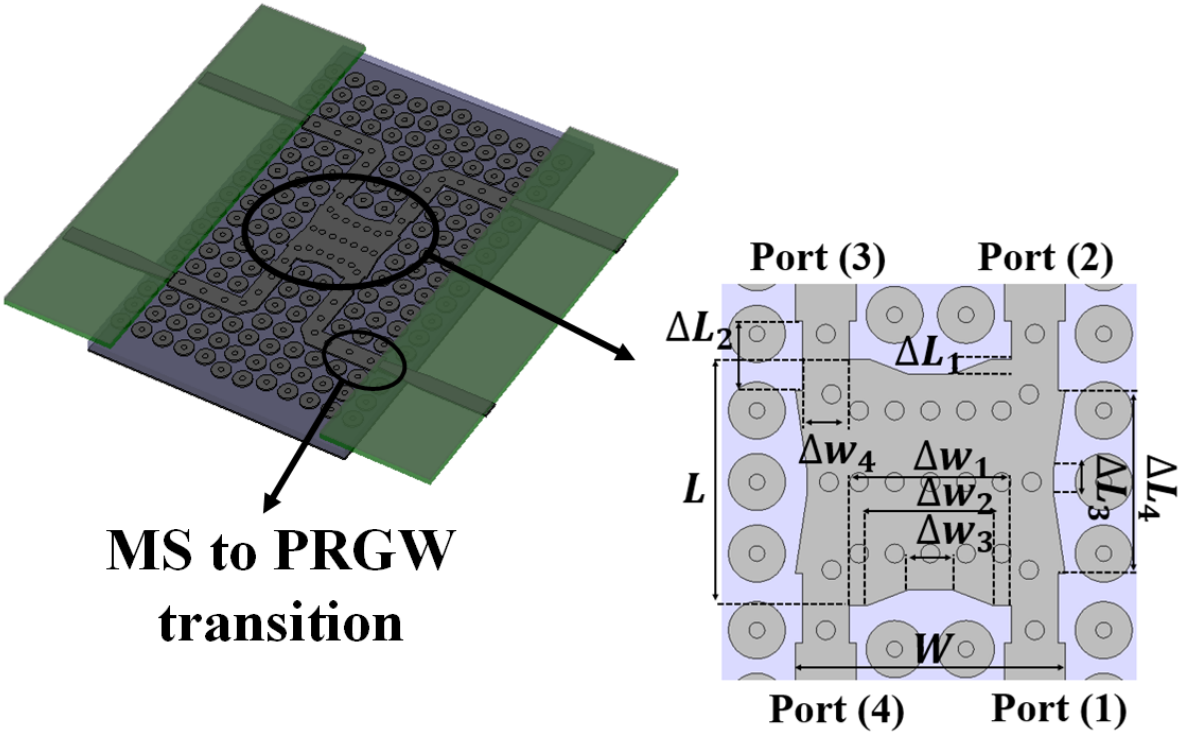

Figure 3.5: Configuration of the proposed coupler (Upper ground is removed for clear illustration).

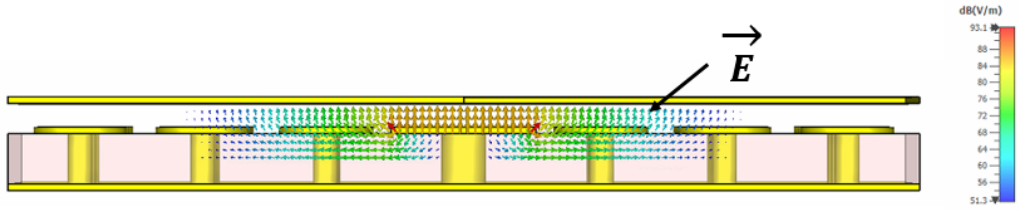

(a)

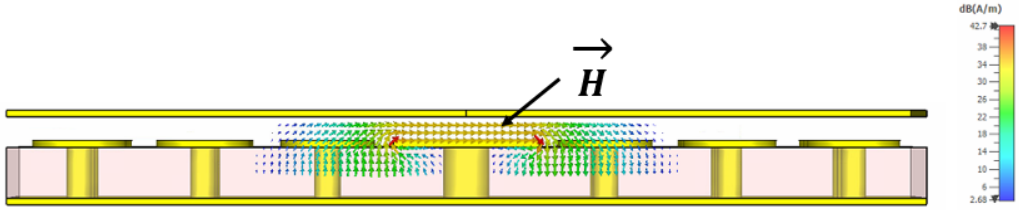

(b)

Figure 3.6: Electric and magnetic field distribution in the PRGW structure. (a) E-field. (b) H-field.

structure is printed on Roger RT 6002 with dielectric constant $\varepsilon_r = 2.94$ and thickness h_s= 0.762. The selected dimensions of the EBG unit cell are 1.5 and 0.508 mm for the

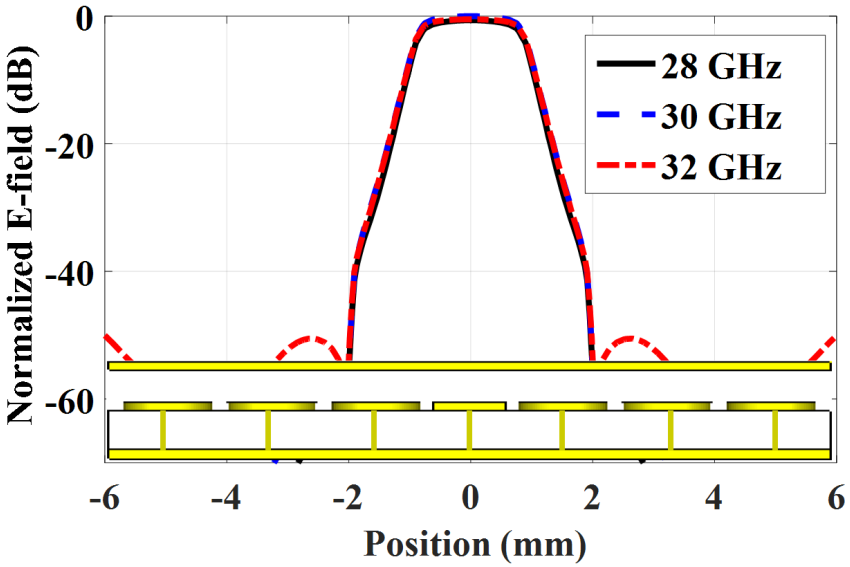

Figure 3.7: Simulated normalized field distribution of the gap waveguide in transverse plane for different frequencies within the operating bandwidth.

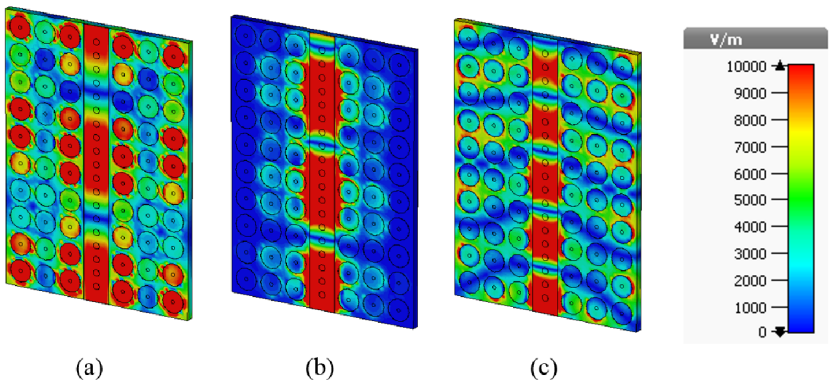

Figure 3.8: The E-field distribution in the PRGW at different frequencies. (a) F=20 GHz,(b) F=30 GHz, and (c) F=40 GHz.

cell size and gap height, respectively. The cell has a circular patch mushroom shape as indicated in Fig. 3.5, where the patch diameter and the via diameter is 1.4 mm and 0.4 mm, respectively. This yields to a band stop from 23 to 38 GHz which covers the operating frequency band of the proposed coupler as shown in Fig. 3.4. In addition, the electric and magnetic field distribution for the designed PRGW line are shown in Figs. 3.6(a) and 3.6(b), respectively. To show the designed cell can provide the field confinement above the ridge and suppress any leakage, the field distribution is plotted over the structure which is shown in Fig. 3.7. The E-field decays in the order of 60 dB/λ. As the second step of verification, the field distribution is calculated and plotted at different frequency bands in Fig. 3.8. It can be depicted from this figure that the field is confined within the designed band, while the leakage occurs below and above this bandwidth. The width of the ridge W_R=1.5 mm is selected to be approximately equal to the EBG unit cell dimension to simplify the alignment of the unit cell around the coupling section as well as the PRGW lines. This leads to having Z_R=79 Ω. Since $Z_o^e = Z_o^o \neq Z_R$, the PRGW line is connected to the coupling section through impedance transformer to match the line impedance with the coupling section impedance as shown in Fig. 3.5. In addition, the coupling section is designed in a tapered shape to provide a degree of freedom for the tuning process. Through the mathematical formulation and the design procedure discussed in the previous section, the initial dimensions of the proposed coupler at the design frequency are obtained. Afterward, an optimization process around 10% of the initial values is performed to obtained The final coupling section length L= 6.1 mm and width W= 6.7 mm are obtained through the optimization process to achieve a forward coupling, where the final dimensions are indicated in Table 3.1. The design procedure can be summarized as follows:

- Determination of the center frequency of the operating bandwidth.
- The coupling section width W and length L are initially calculated based on the even and odd mode analysis.
- Unit cell and PRGW line design.
- Design of impedance transformer.
- Optimization process for better matching level.

Table 3.1: Dimensions of the coupling section in millimeters

Section i	1	2	3	4
$\triangle L_i$	0.32	2.1	0.7	4.5
$\triangle W_i$	4.1	3	1.1	0.9

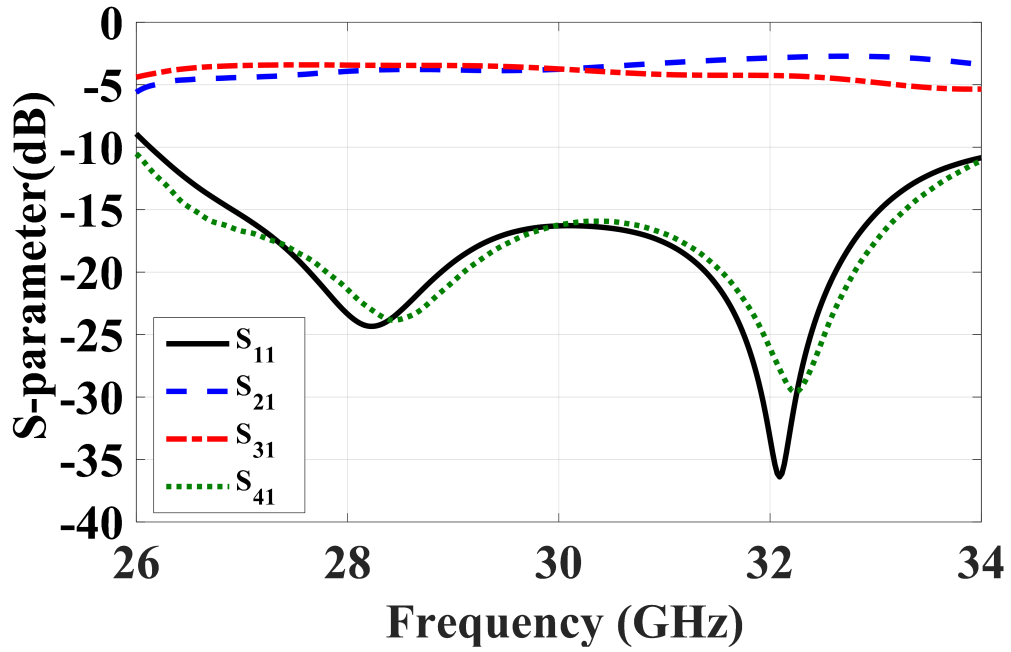

(a)

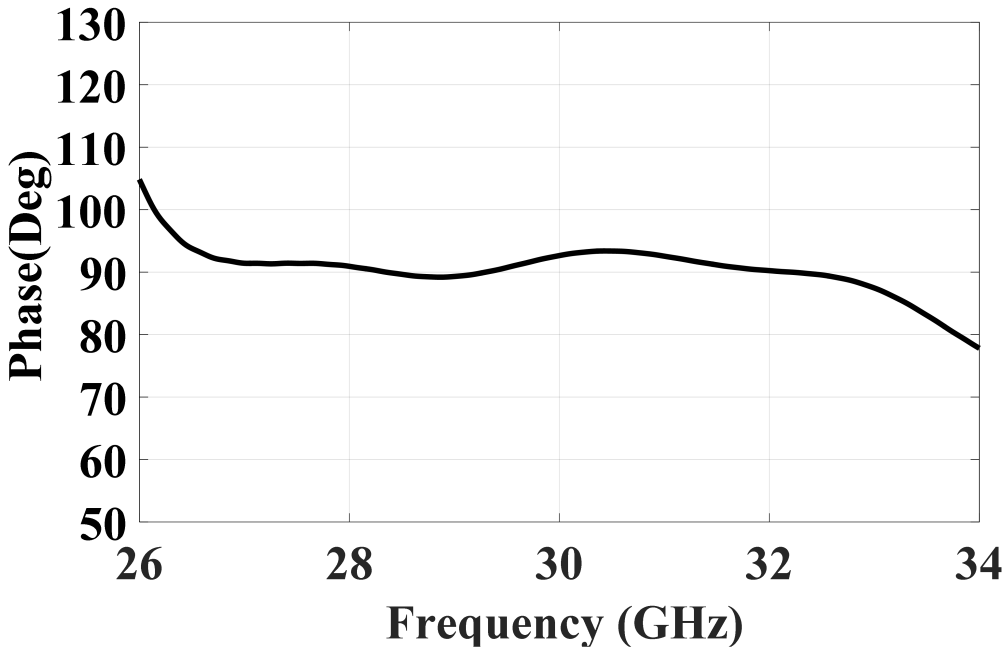

(b)

Figure 3.9: (a) Simulated PRGW hybrid coupler scattering parameters. (b) Phase response of the proposed coupler.

The simulation results of the proposed coupler are shown in Fig. 3.9(a). The proposed coupler has a wide impedance and isolation bandwidth of about 26.5 % at 30 GHz with -10 dB matching level. The phase difference between output ports is 90°± °5 over 23% relative bandwidth with amplitude imbalance of 3.5 ± 0.75 dB over a 13% of the operating frequency band as shown in Fig.3.9.

3.1.3 Microstrip Line to Printed Ridge Gap Waveguide Transition

The design of microstrip line to ridge gap waveguide transitions is studied extensively in the literature as they are essential parts to deploy the ridge gap waveguide technology in many communication systems [27, 28, 145]. Hence, the transition should be featured with wideband performance and deep matching level over the whole possible frequency band supported by the PRGW line. It is required to connect a 79 Ω PRGW to a standard 50 Ω microstrip line. The first step of the transition is connecting the ridge with a microstrip line through a taper transformer as shown in Figs. 3.10 (a) and (b). The second step in the transition design is reducing the input width of the PRGW line to provide a degree of freedom to adjust the matching level and the bandwidth as well. The taper transition initially starts with width W_t= 0.5 mm and linearly increase to the width of standard 50 Ω microstrip line. The length of this transformer is initially selected to be $L_t = \lambda_g/2$. A back to back configuration with a double bend is considered in the simulation of the transition. A tuning process is performed to achieve a -15 dB matching level over the whole possible frequency band supported by the ridge as shown in Figs. 3.10 (c).

3.1.4 Experimental Validation

The proposed hybrid coupler is fabricated, where the prototype and measurement setup are illustrated in Fig. 3.11(a) and 3.11(b). A TRL calibration kit is used to calibrate the (N52271A) PNA network analyzer through transferring the reference plane at the input of the PRGW line. The measured S-parameters are shown in Fig. 3.12(a) which demonstrates a good agreement with simulated results. This figure shows that the proposed hybrid coupler has a 26.5% measured relative impedance and isolation bandwidth centered at 30 GHz with matching level less than -10 dB. Fig. 3.12(b) illustrates a measured

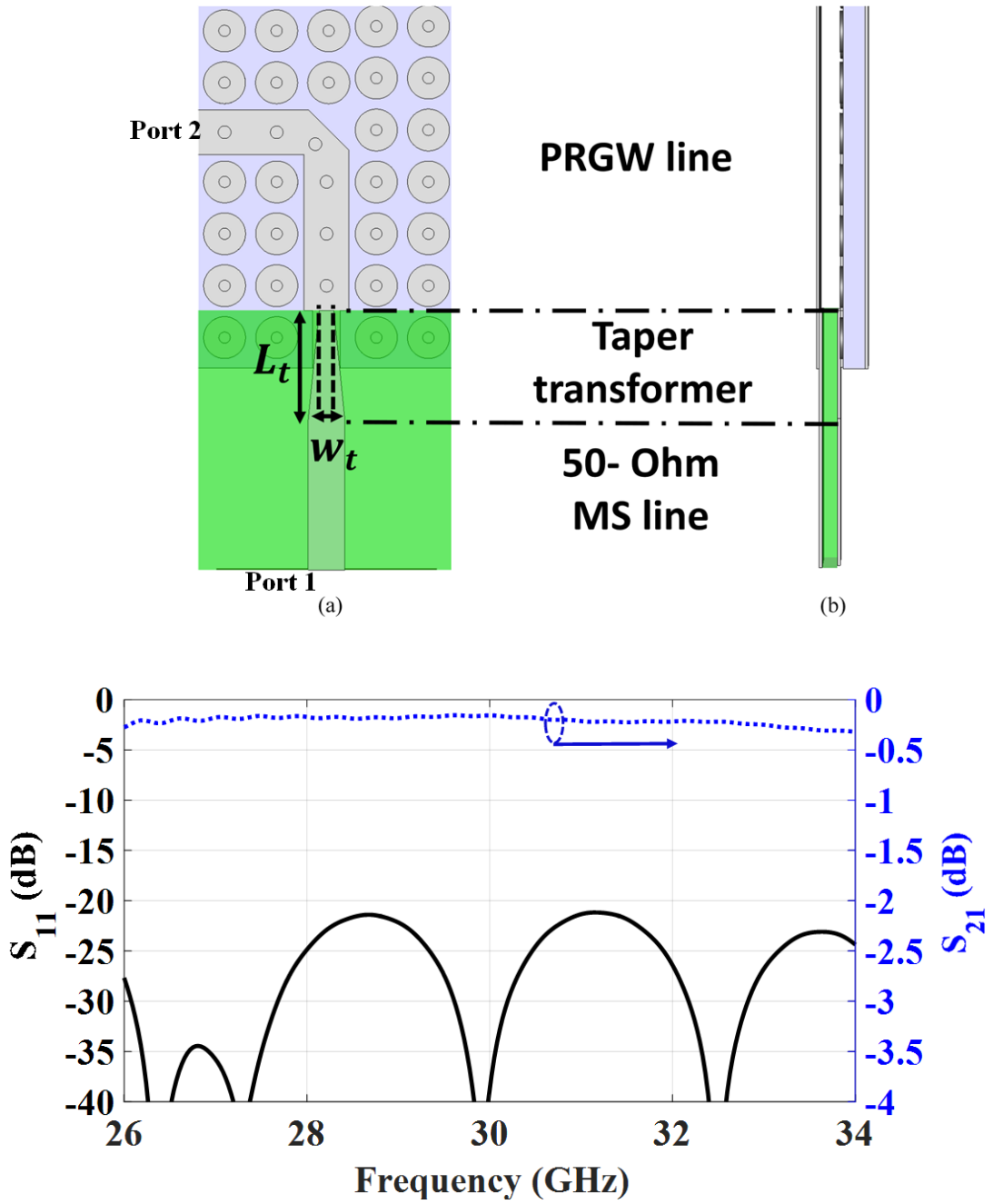

Figure 3.10: Block diagram of 90° bend PRGW with microstrip to PRGW transition. (a) Top view (b) Side view.(c) Simulated S-parameters

phase difference which shows a quadrature-phase between the output ports with ±5 ° over a 23% percentage bandwidth. The measured amplitude of the through and the coupled ports is balanced within ±0.75 dB in a percentage bandwidth of 13 % with an average measured the insertion loss of 0.7 dB at the center frequency of the operating bandwidth. These measured results are in a good agreement with simulation results, while the differences between both results may be attributed to the fabrication tolerances as well as the alignment of the multilayer structure.

3.1.5 Fabrication Tolerance Analysis

An analysis of the response of the coupler according to the tolerances of the manufacturing process is carried out by varying the substrates dielectric constant and the dimensions for both the transition and mushroom cell layers. Fig. 3.13 shows the effect of varying the dielectric constant ε_r as 2.94 ±0.25 on the response of the coupler. In addition, Fig. 3.14 shows the effect of varying the dimensions of the proposed coupler within ± 5% from the optimum values. It can be depicted from these figures that the tolerances of the manufacturing process slightly shifts the frequency response of the proposed coupler.

3.1.6 Performance Evaluation

In this section, we will present a comparison between the proposed coupler and other 3-dB coupling structures implemented with different guiding technologies such as a waveguide, microstrip line, substrate integrated waveguide, and ridge gap waveguide. This comparison assists in evaluating the potential of the proposed structure, which starts with summarizing the proposed 3-dB coupler performance. The introduced coupler is implemented using a printed ridge gap waveguide technology which demonstrated superior features at mm-wave frequencies including low loss and minimal dispersion since the propagating mode is a Q-TEM. The size of the introduced coupler is $1.3\lambda_o \times 1.3\lambda_o$, where λ_o is the free space wavelength at the center frequency. In addition, the proposed coupler has an ultra-wide bandwidth of a 26.5% with a matching level beyond -10 dB. Moreover, the coupler isolation level is less than -15 dB over a 20% relative bandwidth. Furthermore, the proposed component has a measured average insertion loss of 0.7 dB over the operating frequency band. Moreover, the phase difference between through and the coupled ports is balanced within ±5 ° in a percentage bandwidth of 23%. Many coupler configurations

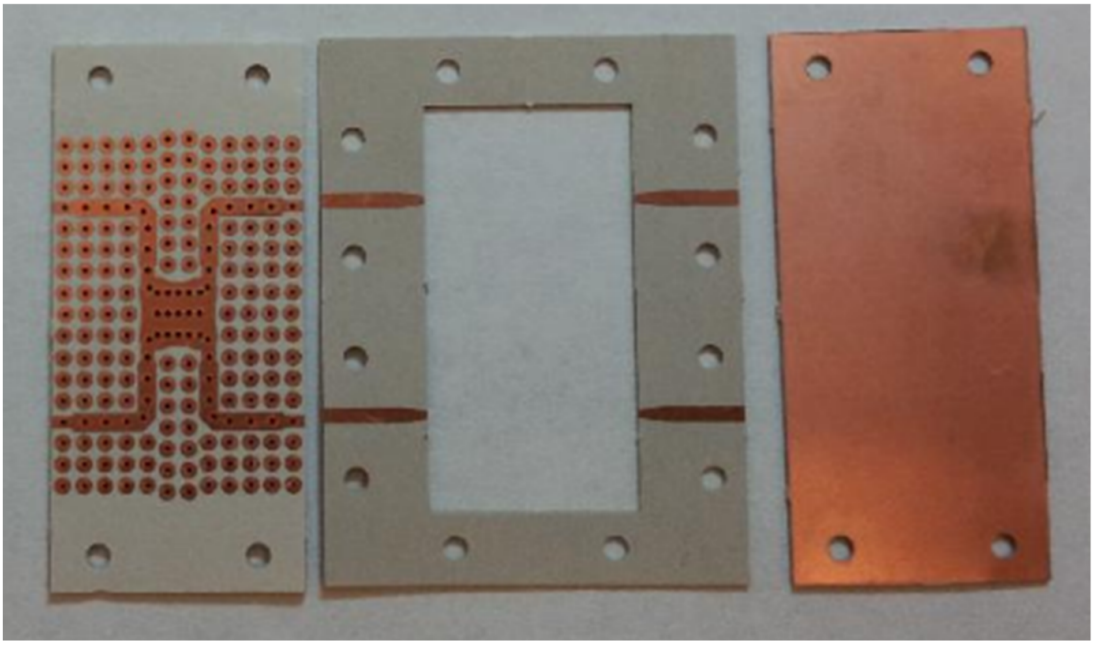

(a)

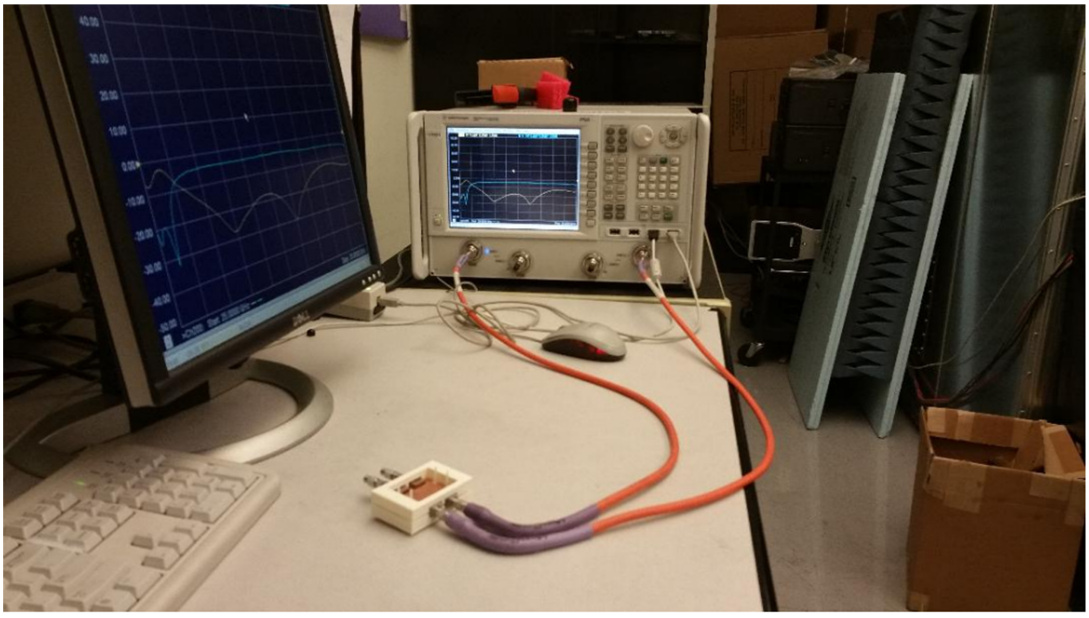

(b)

Figure 3.11: (a) Fabrication of the proposed coupler. (b) Measurement setup.

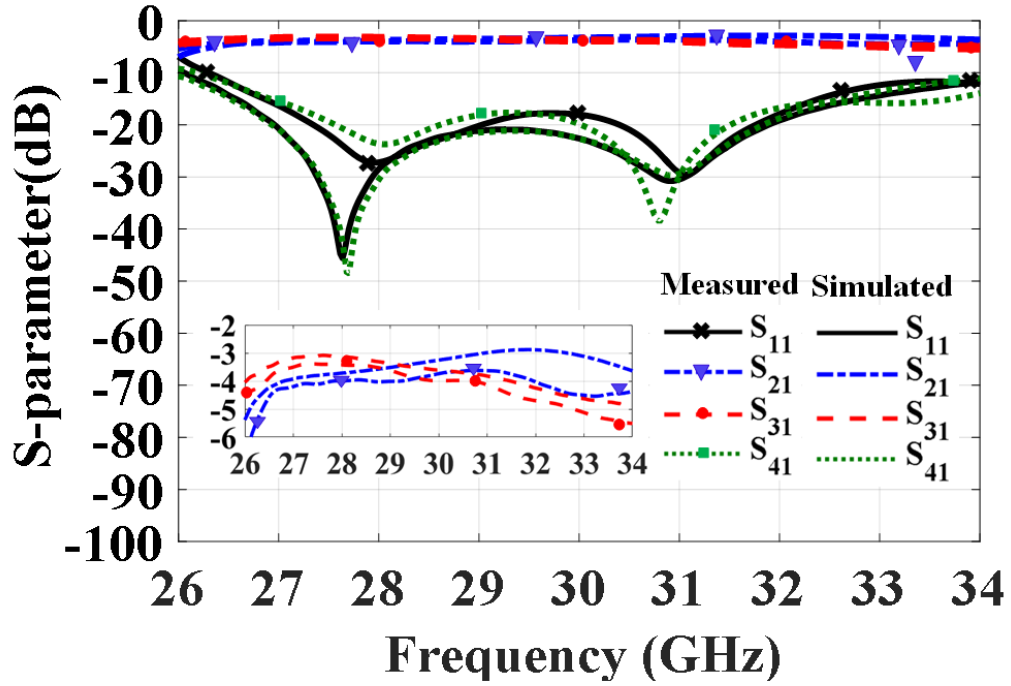

(a)

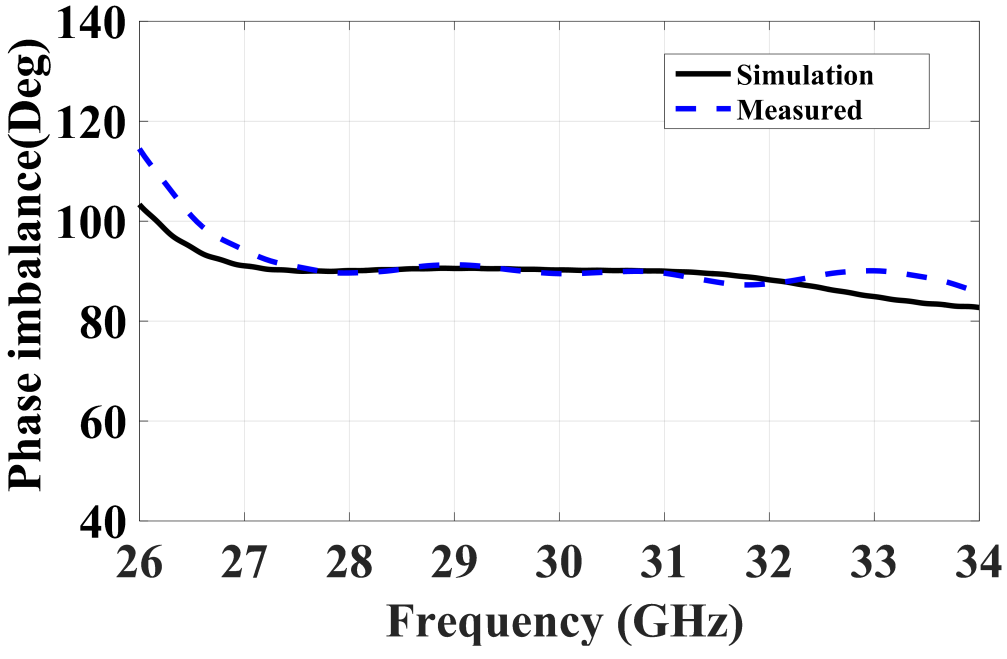

(b)

Figure 3.12: Simulated and measured (a) PRGW hybrid coupler scattering parameters. (b) Phase response of the proposed coupler.

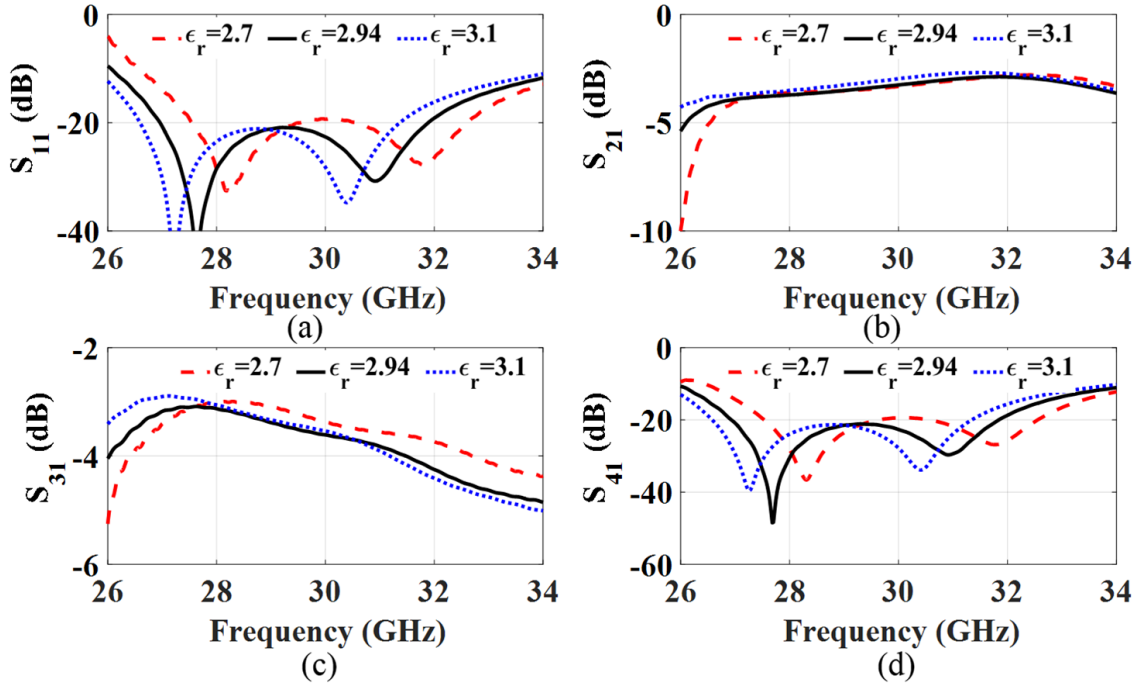

Figure 3.13: Simulated S-parameters at different value of material dielectric constant ε_r. (a) S_{11}, (b) S_{21}, (c) S_{31}, and (d) S_{41}.

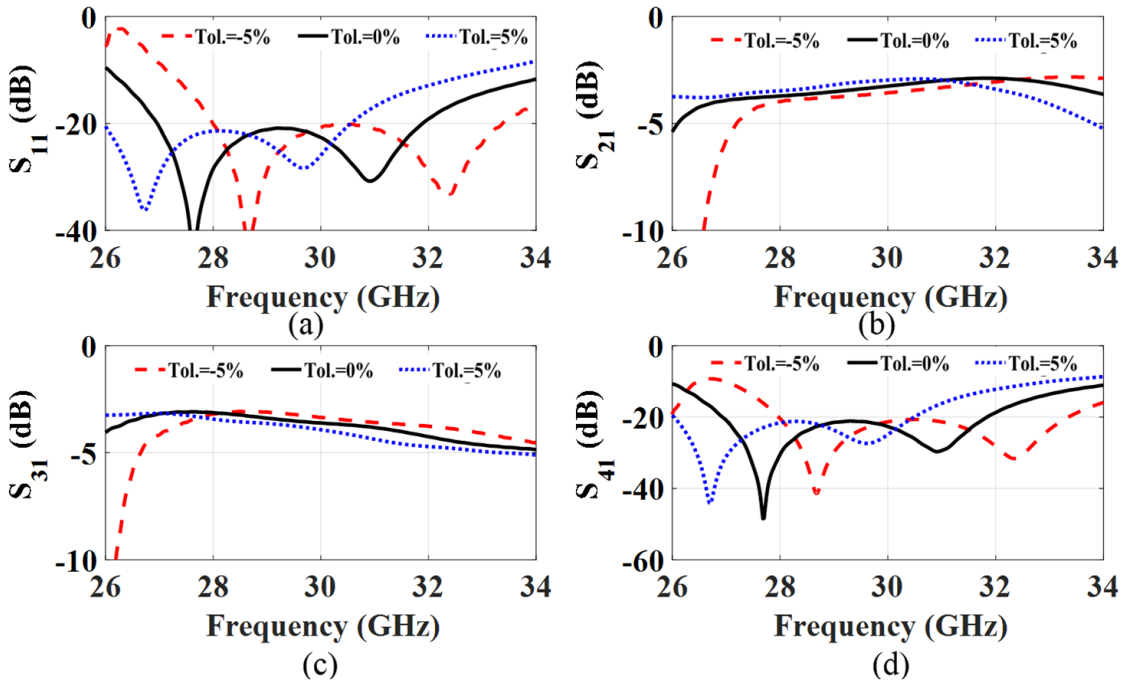

Figure 3.14: Simulated S-parameters at different different fabrication tolerance value. (a) S_{11}, (b) S_{21}, (c) S_{31}, and (d) S_{41}.

Table 3.2: Comparison between couplers configurations

Technology	Impedance BW (S_{11} < -10 dB), f_o	Amplitude balance (dB)	Phase balance	Size ($\lambda_o \times \lambda_o$)
Rectangular waveguide [90]	6.5% (14 GHz)	3.1±0.2 BW = 6.5%	90° ±0.3 BW = 6.5%	1.6 × 1.7
Groove gap waveguide [100]	14.3% (14 GHz)	3±0.75 BW = 7%	90° ±1 BW = 14.3%	2.7 × 5
Ridge gap waveguide [99]	14% (15 GHz)	3.5±0.75 BW = 7%	Not included	1.6 × 1.6
Substrate integrated waveguide [92]	18% (24 GHz)	4.7±0.5 BW ∼ 10%	92° ±2 BW ∼ 18%	1.4 × 1.5
Half mode substrate integrated waveguide [94]	11% (27.75 GHz)	4.08±0.25 BW ∼ 7%	180° ±10 BW ∼ 11%	Not included
Microstrip line [88]	11.2% (30 GHz)	4±1 BW ∼ 11.2%	90° ±1 BW ∼ 11.2%	1.3 × 1.1
Printed ridge gap waveguide [38]	6% (30 GHz)	3.6±1 BW = 6%	90° ±5 BW = 6%	1.1 × 1.1
Proposed work	26.5% (30 GHz)	3.7±0.75 BW = 13%	90° ±5 BW = 23%	1.3 × 1.3

implemented based on different guiding structures have been presented in the literature. Rectangular waveguide (WG) short slot couplers have an average size of $1.6\lambda_o \times 1.7\lambda_o$ with a narrow bandwidth [90, 91]. Although these designs have advantages of low insertion loss of less than 0.2 dB, they support a TE mode which is more dispersive. In addition, they are not preferred for mm-wave applications due to difficulties in ensuring good electrical contacts. Other coupler structures based on RGW technology have been introduced in [99, 100] to overcome the challenges associated with traditional waveguide technology. Although these coupler designs have an average large size of $1.6\lambda_o \times 1.6\lambda_o$, they are supporting a Q-TEM mode which considered an essential feature in many communication systems. One major disadvantage of RGW couplers is fabrication cost. Other coupler configurations implemented based on printed structures such as microstrip line (MS) have been introduced in [88]. Despite the fact that they having a wide bandwidth with the smallest size, they have high radiation and dielectric loss which are remarkable limitations for mm-wave applications. Several hybrid coupler configurations have been presented based on modern printed guiding structure such as SIW [92, 94]. These designs have a wide bandwidth, but they have a large size and high dispersion. In addition, these couplers have high losses due to the dielectric losses. Regarding the PRGW couplers, few

trials were performed before [38,101]. All these trials were limited in terms of bandwidth, while the proposed coupler has the same advantages with a much wider bandwidth. Table 3.2 summarizes the comparison between proposed hybrid couplers with samples of other coupler configurations implemented using other guiding structures. It worth mentioning that, other coupling structures have been extensively investigated in the literature based on different topologies other than the hybrid coupling mechanism, where most of these configurations implement week coupling. The week coupling structures give wider bandwidth for small coupling values of -20, -30 or -40 dB for broad-wall couplers [146, 147], where the structures are based on multi-hole coupling section with large size. On the other hand, compact structures were proposed for week coupling such as loop couplers [148], where the directivity is decreased compared with the broad-wall couplers.

3.2 Compact Ultra-Wideband 3-dB Hybrid Quadrature Coupler

In this section, we are proposing a hybrid coupler whose design is driven by three objectives. First, it should be implemented by PRGW technology to be a candidate for mmWave applications. Second, wide impedance and isolation bandwidth should be achieved at 30 GHz. Last, the proposed design should have a compact size so that compact beam switching systems can be achieved. The 3-D geometrical configuration of the proposed coupler is shown in Fig. 3.15(a). The coupler layer consists of two PRGW lines crossing each other at right angles connected by a square junction surrounded by electromagnetic bandgap (EBG) mushroom-like unit cells. Many articles have addressed the design of the EBG unit cell and PRGW structure [38, 99]. These cells are printed on 0.762 mm thick Roger RT 6002 with a dielectric constant of 2.94 and a loss tangent of 0.0012. The size of EBG unit cell is 0.18 $\lambda\times$ 0.18 λ with 0.508 mm air gap, where λ is the free space wavelength at 30 GHz. These dimensions give a bandgap in the frequency range from 23 to 38 GHz. The microstrip line transition is designed in the transition layer having a 0.508 mm thickness and the same dielectric constant as the coupler layer. The transition layer is used to excite the proposed coupler as well as a spacer between the upper ground layer and the mushroom-like surface.

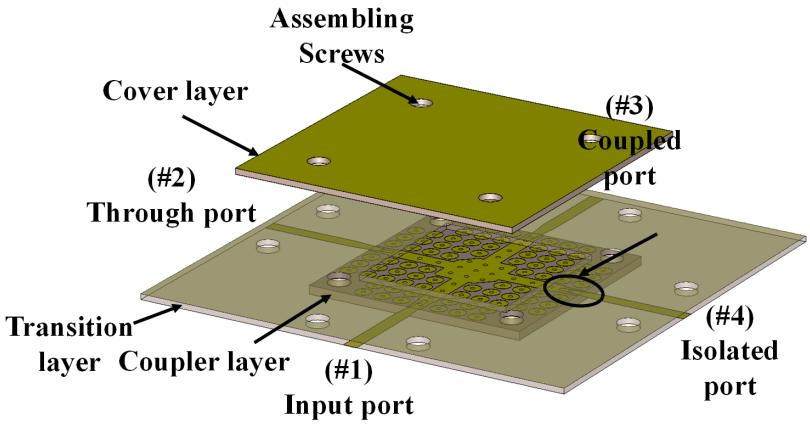

(a)

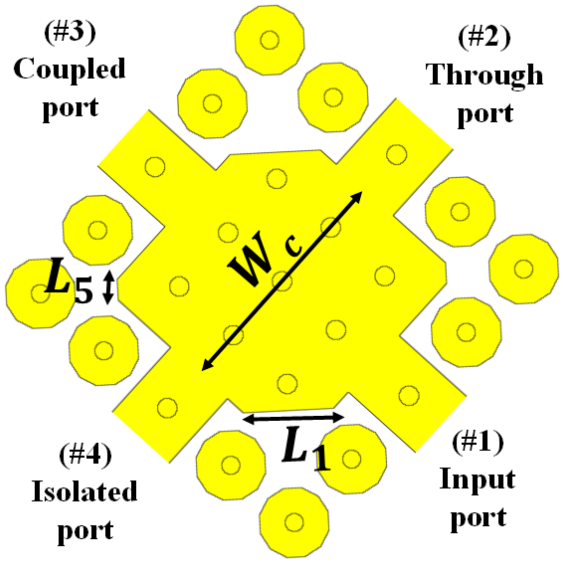

(b)

Figure 3.15: (a) 3-D geometrical configuration of proposed coupler(Upper ground is removed for clear illustration). (b) The coupling section.

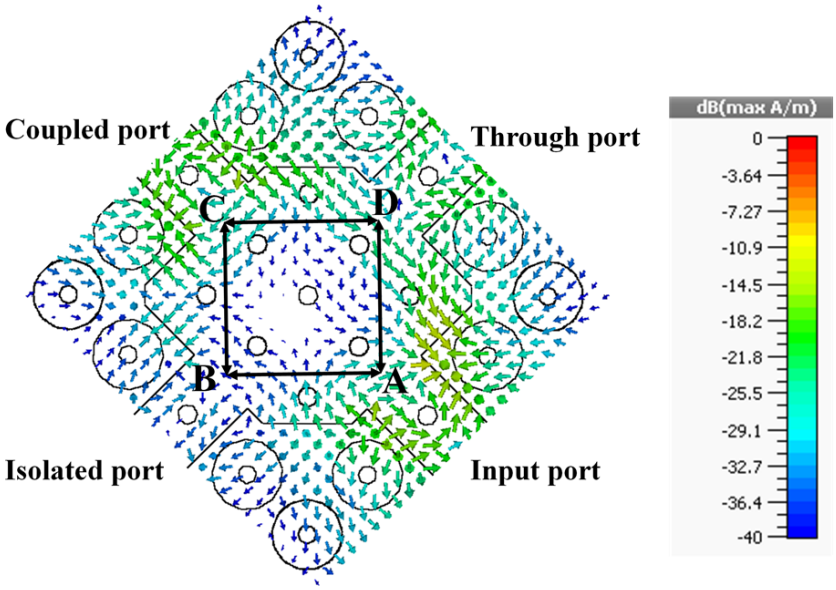

Figure 3.16: The H-field distribution of the proposed coupler.

3.2.1 Design Concept

In order to clarify the operating principle and the design of the proposed coupler, the magnetic field (H-field) distribution in the middle of the air gap region is presented in Fig. 5.17(a). It is worth mentioning that the proposed coupler can be modeled as a branch line coupler since the H-field intensity is reaching the minimum in the center of the patch and the maximum intensity is concentrated on the outer portion of the patch. In other words, if the area where the H-field minimum removed, the resulted configuration can act as a branch line coupler, where the removed portion is not affecting the response. Therefore, the length of the cuts L_1, L_5 and the size of the coupling section W_c that indicated in Fig. 3.15(b) should be adjusted to achieve the quarter wavelength and proper impedances to operate similarly as a branch coupler. Also, the input power is divided equally between the coupled and through ports only at the center operating frequency, where the dimensions (A-B, B-C, C-D, and D-A) are selected to be equivalent to the quarter wavelength at 30 GHz. The reason for the appearance of two resonances in the S-parameters that are shown in the simulation and experimental validation section may come from the fact that the cuts L_1 and L_5 produces two resonance modes that are separated from each other and located approximately at 27 GHz and 32 GHz. Hence, the optimum dimensions of the coupling section are selected to be W_c =5 mm, L_1 = 1.9 mm, and L_5 =0.4 mm This results from the asymmetry of the coupling section that can be

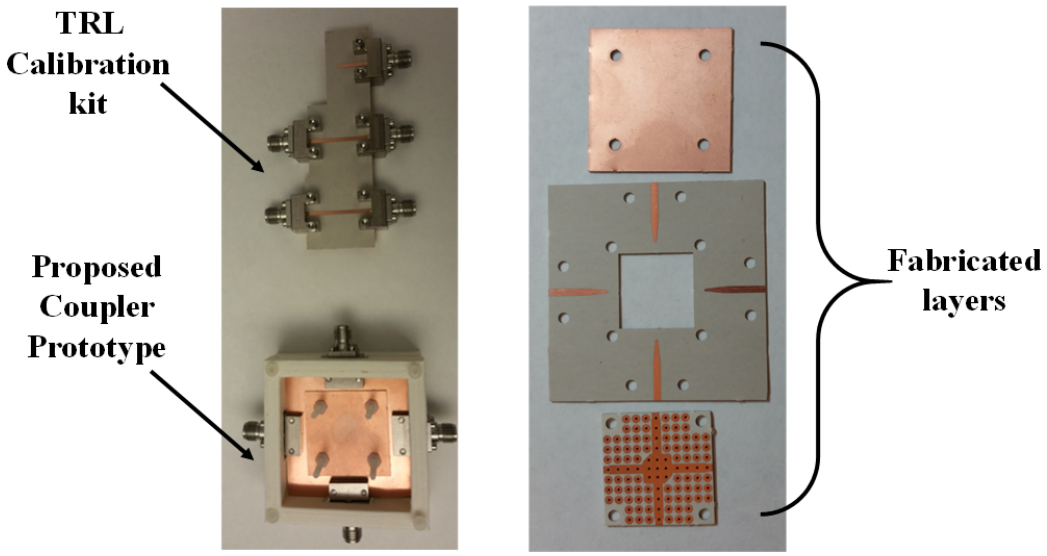

Figure 3.17: Fabrication of the proposed coupler.

modeled as a single cavity resonator operates at two resonance frequencies. This working principle is similar to that presented in [107], where two modes are employed to enhance the bandwidth of a crossover component.

3.2.2 Simulation and Experimental Validation

The proposed coupler is fabricated using standard PCB process and assembled using plastic screws as shown in Fig. 3.17. Since the connectors and the transitions yield more insertion loss, the Thru-Reflect-Line (TRL) calibration is done to de-embed the effects of end launch connectors and transitions in measurements. The S-parameters measurements were taken sequentially by connecting two ports to the Vector Network Analyzer (VNA) and the two other ports to 50 Ω matching loads. The measured and simulated S-parameters of the proposed coupler are shown in Fig. 3.18(a), which demonstrates that the proposed hybrid coupler has a 26.5% measured relative impedance bandwidth centered at 30 GHz with a return loss and isolation better than 15 dB over the operating frequency band. Fig. 3.18(b) illustrates a measured phase difference which shows a quadrature-phase between the output ports with ±5° over a 23% percentage bandwidth. The measured amplitude of through and the coupled ports is balanced within ±0.75 dB in a percentage bandwidth of 13 % with a measured insertion loss of 0.6 dB at the center frequency of the operating bandwidth. These measured results are in a good agreement with simulation results, while the differences between both results may be attributed to

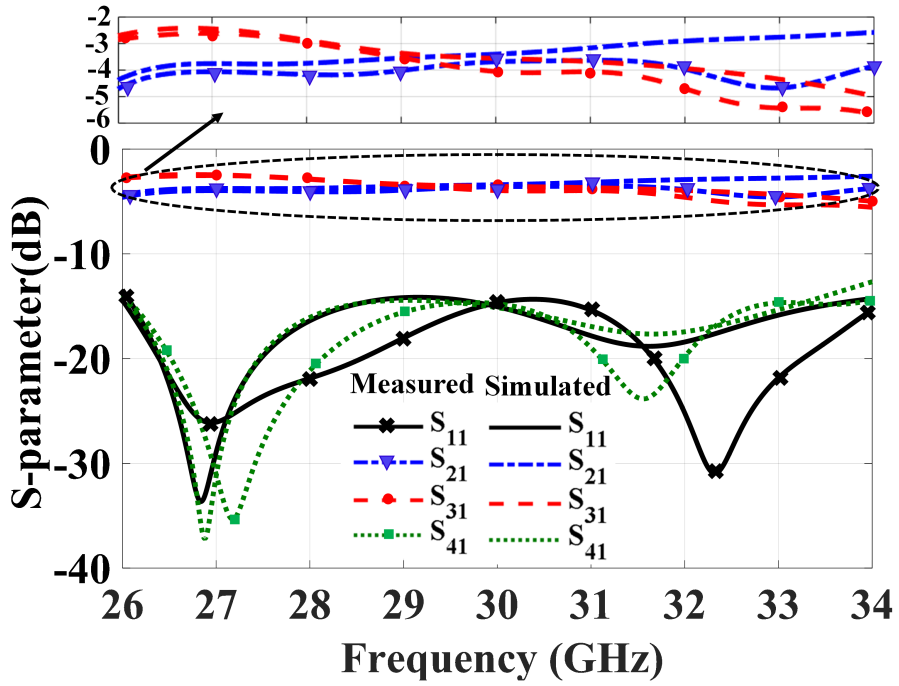

(a)

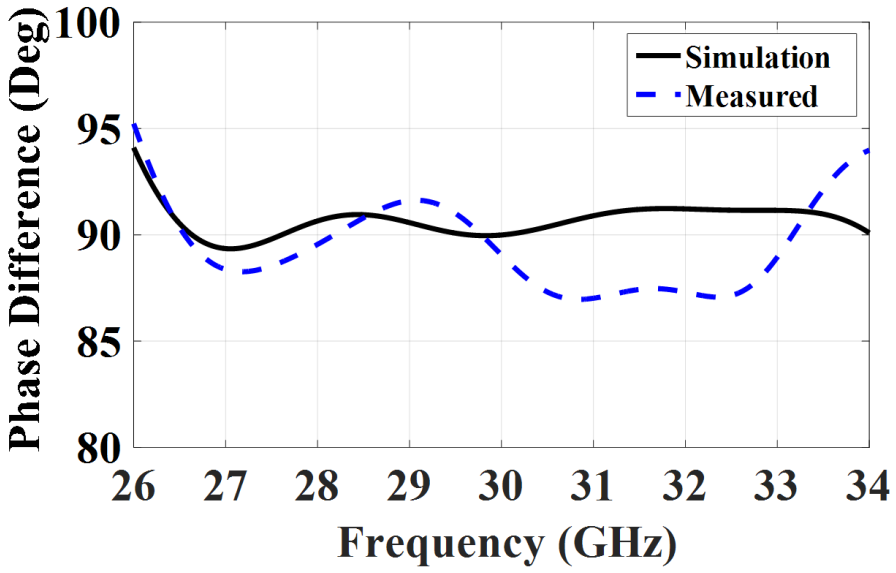

(b)

Figure 3.18: Simulated and measured,(a) S-parameters for the proposed coupler. (b) Output ports phase difference.

Table 3.3: Comparison between couplers configurations

Technology	Impedance BW (S_{11} < -10 dB),f_o	Amplitude balance (dB)	Phase balance	Size ($\lambda_o \times \lambda_o$)
Rectangular waveguide [90]	6.5% (14 GHz)	3.1±0.2 BW = 6.5%	90° ±0.3 BW = 6.5%	1.6 × 1.7
Groove gap waveguide [100]	14.3% (14 GHz)	3±0.75 BW = 7%	90° ±1 BW = 14.3%	2.7 × 5
Ridge gap waveguide [99]	14% (15 GHz)	3.5±0.75 BW = 7%	Not included	1.6 × 1.6
Substrate integrated waveguide [92]	18% (24 GHz)	4.7±0.5 BW ∼ 10%	92° ±2 BW ∼ 18%	1.4 × 1.5
Half mode substrate integrated waveguide [94]	11% (27.75 GHz)	4.08±0.25 BW ∼ 7%	180° ±10 BW ∼ 11%	Not included
Microstrip line [88]	11.2% (30 GHz)	4±1 BW ∼ 11.2%	90° ±1 BW ∼ 11.2%	1.3 × 1.1
Printed ridge gap waveguide [38]	6% (30 GHz)	3.6±1 BW = 6%	90° ±5 BW = 6%	1.1 × 1.1
Printed ridge gap waveguide [149]	26.5% (30 GHz)	3.7±0.75 BW = 13%	90° ±5 BW = 23%	1.3 × 1.3
Proposed work	26.5% (30 GHz)	3.6±0.75 BW = 13%	90° ±5 BW = 26%	1.2 × 1.2

the fabrication tolerances as well as the alignment of the multilayer structure.

3.2.3 Performance Evaluation

Finally, the performance of this work is evaluated through a comparison between the proposed coupler and other reported couplers implemented with different guiding technologies. This comparison is summarized in Table 3.3. Compared with the SIW and RGW couplers, the proposed PRGW coupler is with the smallest circuit size and low insertion loss. Although the microstrip coupler in [88] has a smaller size, it has limited bandwidth with higher insertion loss. Regarding the PRGW coupler presented in [38], it has a narrow band performance, which achieves only 6 % relative bandwidth at 30 GHz. On the other hand, the presented work focuses on improving performance, where a remarkable improvement in the performance is achieved. Compared with the wide band coupler presented in [149], it has similar wide bandwidth, however, it's size is larger than the proposed one. In addition, lower loss with wide phase balance bandwidth is achieved. Hence, the proposed PRGW coupler exhibits a miniaturized size and better performance.

3.3 Compact PRGW Crossover

The conventional crossover consists of cascading two 3-dB hybrid couplers yield to a large physical area, which may not be suitable for wireless mmWave applications. Various techniques implemented by modern technologies have been developed to miniaturize the size of the crossover [104, 106, 107, 150, 151]. However, many of these designs suffer from either poor performance (i.e., narrow bandwidth, low isolation, large transmission loss and/or large size) or complex structure, which greatly limits their practical application use. Therefore, the main objective of this subsection is to introduce the design and implementation of a compact wide bandwidth crossover for millimeter-wave applications based on PRGW technology.

3.3.1 Compact Crossover design

The geometrical configuration of the proposed crossover is shown in Fig. 3.19. The procedure of designing the proposed crossover starts with the design of electromagnetic bandgap (EBG) structure unit cell and PRGW line which is printed on 0.508 mm thick Roger RT 6002 with a dielectric constant of 2.94 and loss tangent of 0.0012 to cover 23.5-36.5 GHz, frequency band. The size of EBG unit cell is 0.18 $\lambda\times$ 0.18 λ with a 0.508 mm air gap, where λ is the free space wavelength at 30 GHz.

Similar design procedure is deployed to design a 0 dB coupler, where the coupling section width W is selected to satisfy a 5% impedance difference between the even and odd mode characteristics impedances over the frequency band of interest. By adjusting the coupling section length L, most of the power is coupled to the output port, while the other ports are isolated. Based on the even and odd mode analysis done in subsection 3.1, the coupling section W=8 mm is selected as an initial value, where the percentage difference approximately goes below 5%. The maximum coupling can be achieved when the length L gives a Φ equal to $\pm 180^{\circ}$. Hence, the coupling section length $L = 10$ mm is considered as an initial value for the realization of the proposed crossover. Also, H-plane impedance steps are employed to provide a degree of freedom in the tuning process and size reduction, where the final dimensions of the proposed crossover are indicated in Table 3.4.

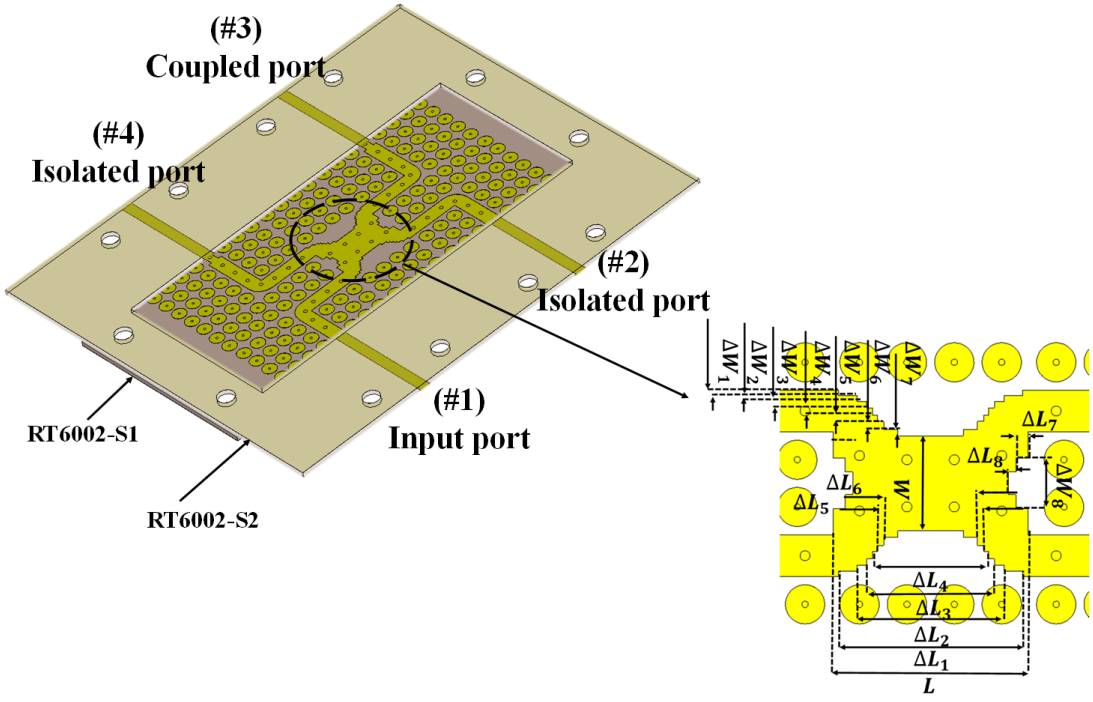

Figure 3.19: Block diagram of the 3-D geometrical configuration of 0 dB coupler (Upper ground is removed for clear illustration).

Table 3.4: Dimensions of the coupling section in millimeters

Section i	1	2	3	4	5	6	7	8
$\triangle L_i$	7.5	6	5.2	4.7	4.3	3.8	0.5	0.3
$\triangle W_i$	0.22	0.24	0.26	0.31	0.25	0.33	0.26	0.92

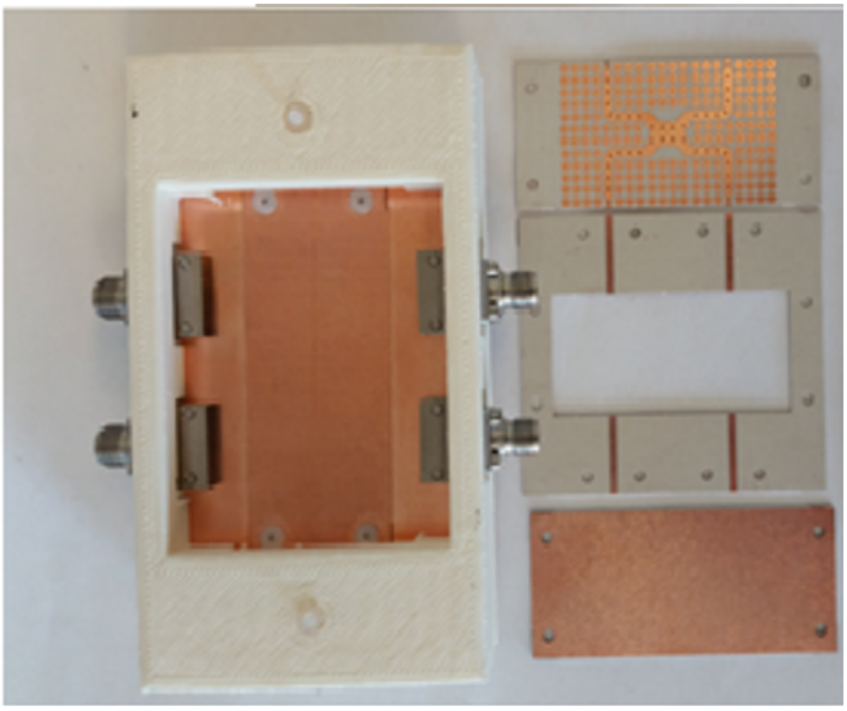

(a)

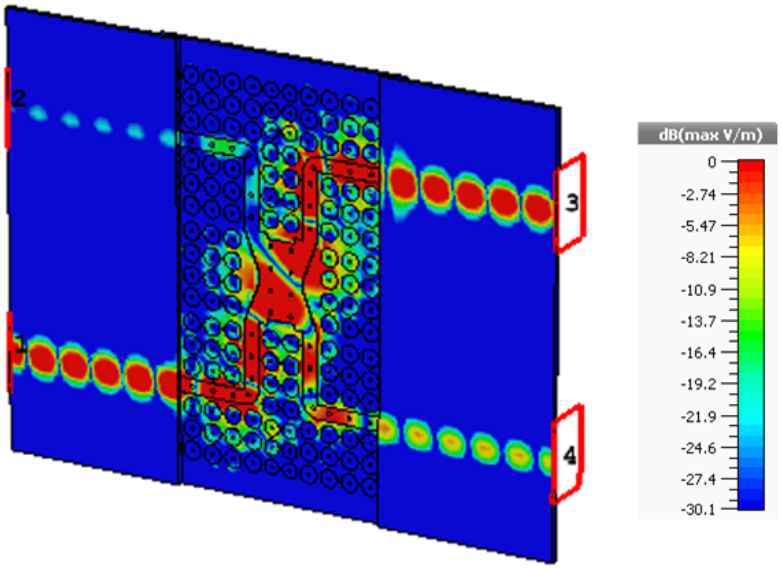

(b)

Figure 3.20: (a) Fabrication of the proposed crossover , and (b) The electric field distribution of the proposed crossover.

3.3.2 Simulation and Experimental Validation

The proposed 3-layers crossover is fabricated using standard printed circuit board (PCB) process and assembled using plastic screws. The photograph of the fabricated prototype is shown in Fig. 3.20(a). The S-parameters measurements were taken in a sequential way

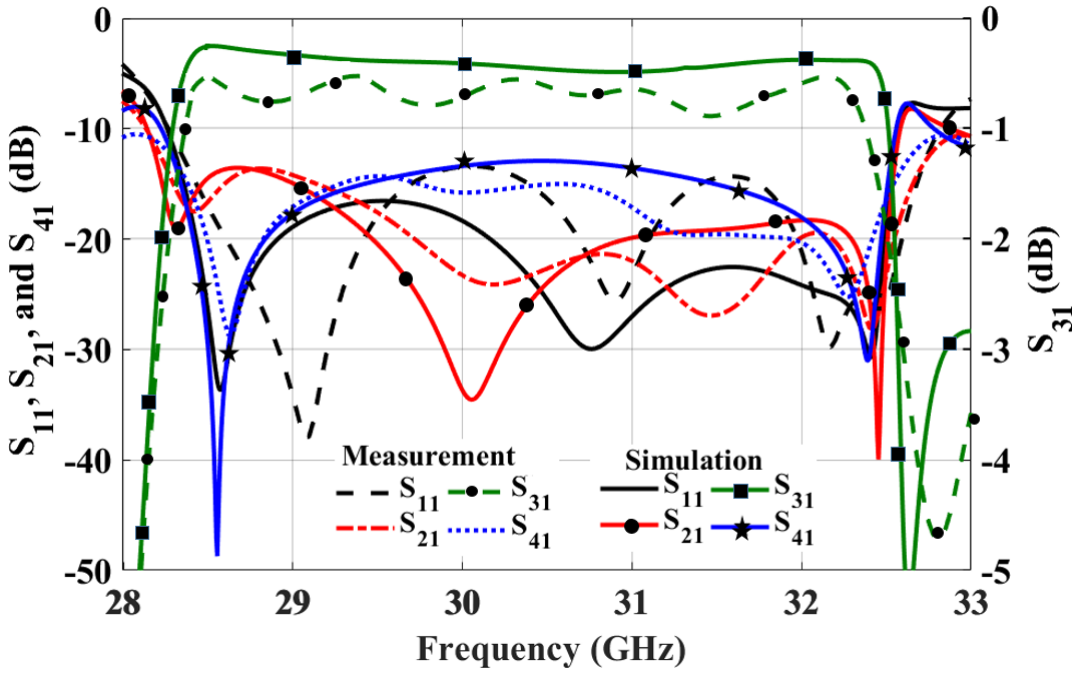

Figure 3.21: Simulated and measured S-parameters for the proposed crossover

by connecting two ports to the vector network analyzer (VNA) and the two other ports to 50 Ω matching loads. Also, the electric field distribution is shown in Fig. 3.20(b) emphasizes the performance of the proposed crossover in terms of isolation.

The simulated S-parameters of the proposed crossover in Fig. 3.21 demonstrates that the return loss is better than 10 dB over the band of interest from 28.5 to 32.5 GHz (13%). The isolation between the input port and the other two ports (2 and 4) is better than 13.5 dB over the desired frequency band. The coupling between ports 1 and 3 is around -0.5 dB from 28.5 to 32.5 GHz. Based on the simulated and measured results shown in Fig. 3.21, this 0 dB coupler can be used as a crossover in the beam steering applications with acceptable bandwidth.

3.3.3 Performance Evaluation

Finally, the performance of the proposed crossover structure is compared with the performance of other crossover structures in Table 3.5. Obviously, compared with the SIW crossover in [104], the proposed PRGW crossover has low insertion loss with wide bandwidth. Although the slotted SIW crossover in [107] has a wider fractional bandwidth, it has a larger size with higher insertion loss. Based on PRGW technology, a compact size crossover has been reported in [150], however, it has a narrower bandwidth than the

proposed component. While a wide bandwidth PRGW crossover is presented in [151], however, it has a larger size. Hence, the proposed PRGW crossover exhibits miniaturized size and high performance in terms of loss and bandwidth.

Table 3.5: Comparison between crossover configurations

	[104]	[107]	[150]	[151]	This work
Center Freq.(GHz)	20	30	30	30	30
Tech.	SIW	Slot. SIW	PRGW	PRGW	PRGW
BW (%)	10.5	16.7	1.6	13.3	13.3
Insertion loss (dB)	-	0.9	0.6	0.5	0.5
Size (λ^2)	2	3.1	2.1	2.8	2.25

Chapter 4

Millimeter Wave Scanning Antenna Array Fed by PRGW

Recently, millimeter-wave (mmWave) frequency bands are attracting more attention due to its ability to support a higher data rate for the next-generation of wireless communication systems. In 2015, World Radio Communication Conference (WRC -15) is proposed several mmWave frequencies ranging from 24 GHz to 86 GHz to accommodate emerging applications which are very critical for both commercial and industrial purposes [6]. Such applications will support a variety of fundamental personal communication services as well as high-data-rate applications enabling high definition video transmission. These services would have a high potential for the industry and support many sectors such as healthcare, connected homes, secure transport, security applications, and entertainment. Besides the huge frequency spectrum available in the mmWave band, intelligent subsystems such as beam switching are necessary in order to address the challenges and expectations of future technology. These can be summarized as high power efficiency, multi-user systems, and large channel capacity with wide scanning coverage. In addition, adopting the state of the art guiding structures, especially printed ridge gap waveguide (PRGW) to implement beam switching network for scanning antenna array will improve the system efficiency through providing low losses at mmWave frequencies.

In this chapter, we are investigating the use of PRGW technology as low signal distortion, low loss, and wide bandwidth beam switching network can be achieved. The main objective of this work is to introduce the design and implementation of a 2-D scanning antenna array fed by 4×4 PRGW butler matrix at mmWave bands. The butler matrix is implemented only using hybrid couplers that designed in the previous chapter to have a compact, low loss, and a wide relative bandwidth with stable phase balance. The proposed PRGW butler matrix is used to feed a 2×2 ME dipole antenna array to construct a 2-D

scanning antenna array features with a wide bandwidth and high radiation efficiency. The proposed antenna array is shown the ability to radiate 2-D beams, one in each quadrant at 35^o elevation angle. The proposed antenna array is fabricated and measured, where a good agreement between the simulated and measured results is achieved. In addition, a gain enhancement for the proposed ME-dipole two-dimensional scanning antenna array is achieved. A hybrid gain enhancement technique including AMC mushroom shapes around the antenna array with a perforated dielectric substrate lens located into the broadside direction is proposed. Therefore, all of these features make the proposed scanning antenna array candidates for millimeter-wave applications.

4.1 PRGW Beam Switching Network

In this section, a 2-D beam switching network (BSN) is proposed and theoretically analyzed. Next, a 4× 4 Butler Matrix based on the 2-D BSN is realized using a PRGW technology, where a 90^o hybrid coupler is well designed to have a compact size with wide operating bandwidth at 30 GHz. The purpose of this BSN is to provide a feeding network to feed antenna array and achieve a 2-D scanning ME antenna array as will be presented in the folowing sections.

4.1.1 Theory and Design

The block diagram of the proposed 2-D BSN is shown in Fig. 4.1, which consists of four 90^o hybrid couplers having four feeding ports 1-4 with output ports 5-8 connecting the antenna array elements. This configuration can provide phase differences $\Phi_x = \angle S_{5p} - \angle S_{6p} + 180^o = \angle S_{8p} - \angle S_{7p} + 180^o = \pm 90^o$ and $\Phi_y = \angle S_{5p} - \angle S_{8p} = \angle S_{6p} - \angle S_{7p} = \pm 90^o$ along the x-axis and y-axis, respectively, where subscript $p = 1, 2, 3, 4$ represents the corresponding input port. The phase differences Φ_x is added by 180^o, since couple of the output ports are opposite to each other along the x-direction. According to phase differences Φ_x and Φ_y, the orientation (Φ_o, θ_o) of the scanning beam can be calculated as follows [74]:

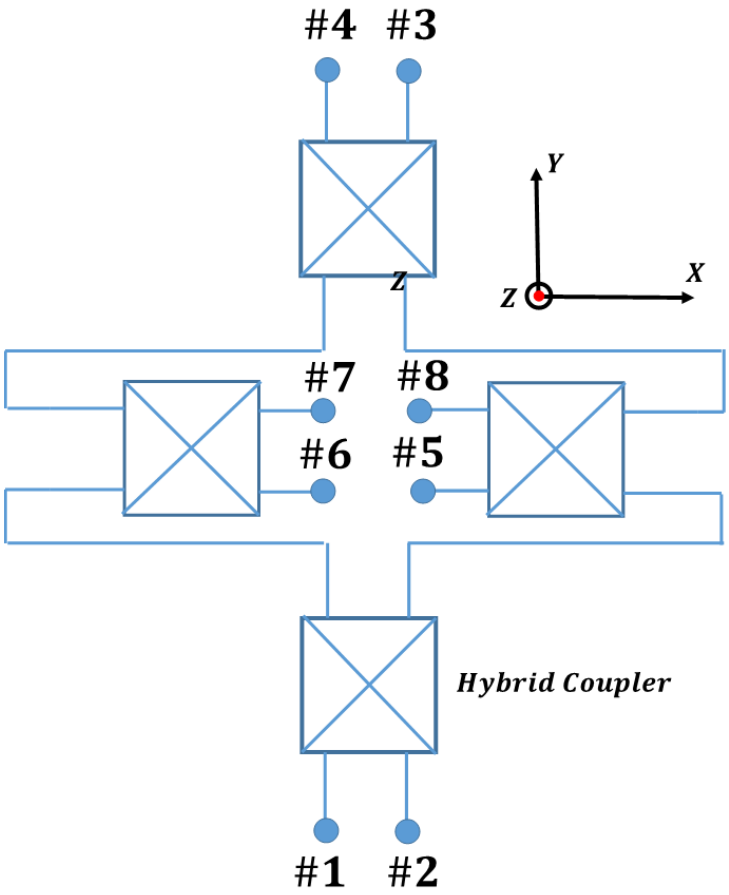

Figure 4.1: Block diagram of the proposed 2-D BSN.

$$\Phi_o = \tan^{-1}\left(\frac{\Phi_y d_x}{\Phi_x d_y}\right) \tag{4.1}$$

$$\theta_o = \sin^{-1}\sqrt{\left(\frac{\Phi_x}{k d_x}\right)^2 + \left(\frac{\Phi_y}{k d_y}\right)^2} \tag{4.2}$$

where d_x and d_y are the spacing between two adjacent antenna elements in the x- and y-direction, respectively, and k is the propagation constant in free space. The phase profile of the theoretical 4× 4 Butler Matrix is given in Table 4.1, assuming here that $d_x = d_y = \lambda/2$ at the 30 GHz to simplify the analysis. This phase profile results in four beams that are located in four quadrants of the array.

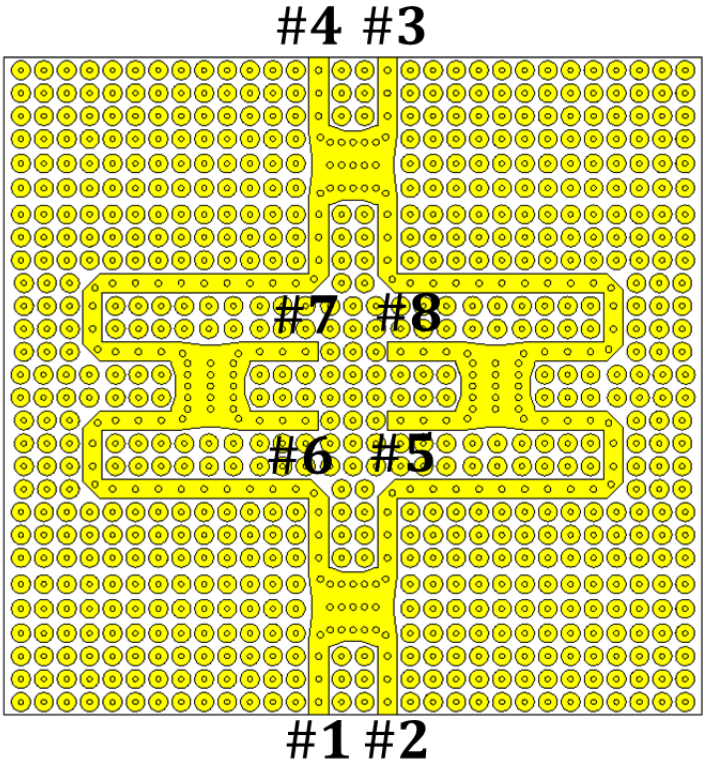

(a)

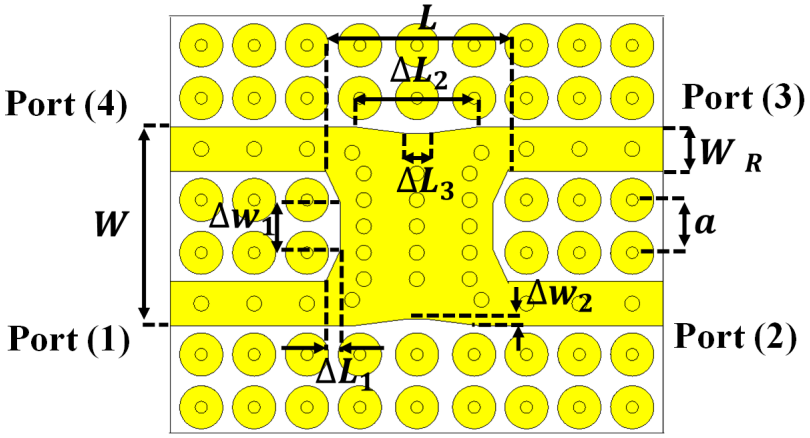

(b)

Figure 4.2: (a) Geometry of the proposed planar 4× 4 butler matrix with four hybrid PRGW couplers (Upper ground is removed for clear illustration). (b)PRGW hybrid coupler.

Table 4.1: Theoretical phase profile of the proposed Butler matrix

Input Port	Φ_x	Φ_y	θ_o	Φ_o
Port 1	90^o	90^o	45^o	-135^o
Port 2	-90^o	90^o	45^o	-45^o
Port 3	-90^o	-90^o	45^o	45^o
Port 4	90^o	-90^o	45^o	135^o

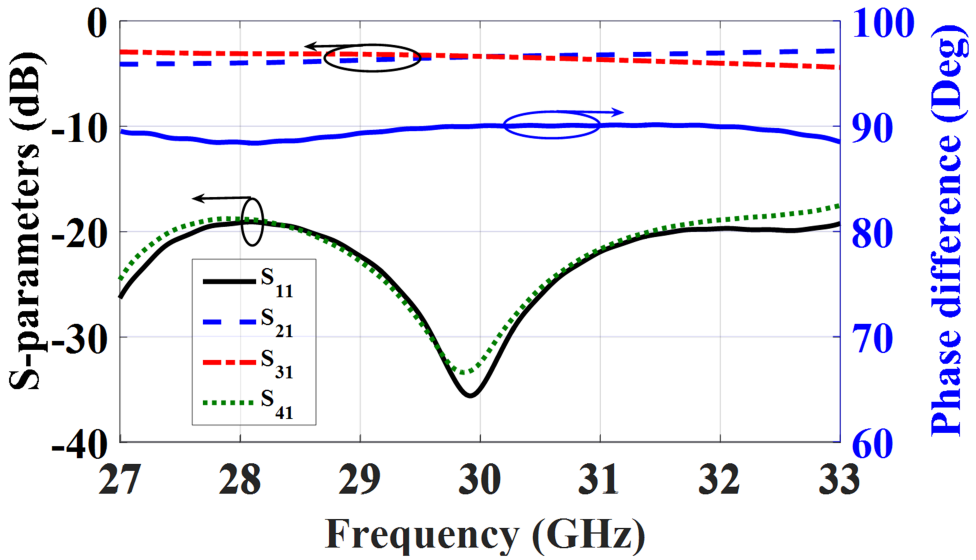

Figure 4.3: Simulated PRGW hybrid coupler scattering parameters and output phase difference.

4.1.2 Realization of 4× 4 Butler Matrix

Based on the block diagram shown in Fig. 4.1, the configuration of the proposed Butler matrix consisting of four 90^o hybrid couplers is shown in Fig. 4.2(a). Due to the low-loss, minimum dispersion, and wide bandwidth of the PRGW technology in mmWave bands, the proposed 3-dB planar quadrature hybrid couplers are implemented using PRGW structure. The design of the coupler shown in Fig. 4.2(b) is addressed before in Sec. 3.1, which achieved a 26 % relative impedance bandwidth at 30 GHz. In this section, this coupler is re-tuned to operate from 27-33 GHz with a deep matching level less than -20 dB over 20 % relative bandwidth as shown in Fig. 4.3. In addition, the phase difference ($\angle S_{21} - \angle S_{31}$) between output ports is 90°± °2 over the whole operating bandwidth with amplitude imbalance of 3.4 ± 0.5 dB over a 12% of the operating frequency band

As the Butler matrix network shown in Fig. 4.2(a) is completely symmetric, only the performances of the input port (p=1) are shown in Fig. 4.4(a). The input reflection coefficient and the coupling to the other input ports are almost better than -15 dB over

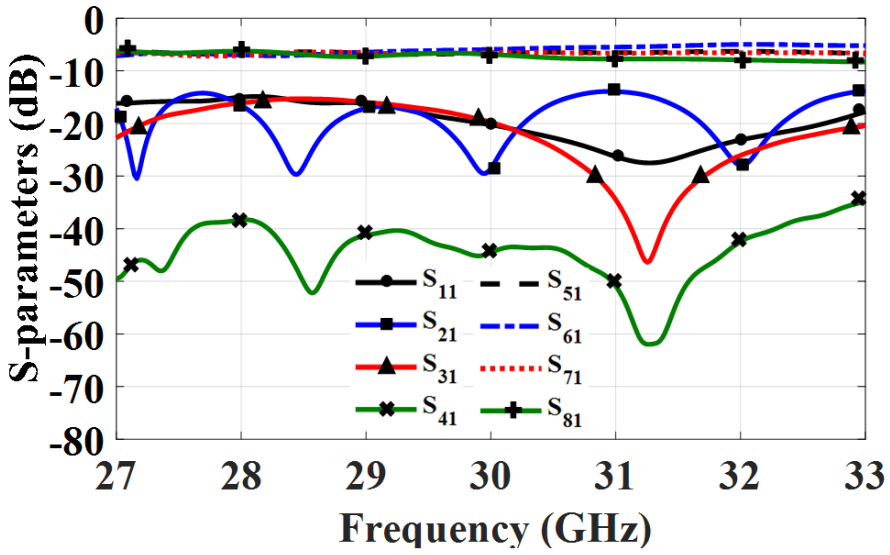

(a)

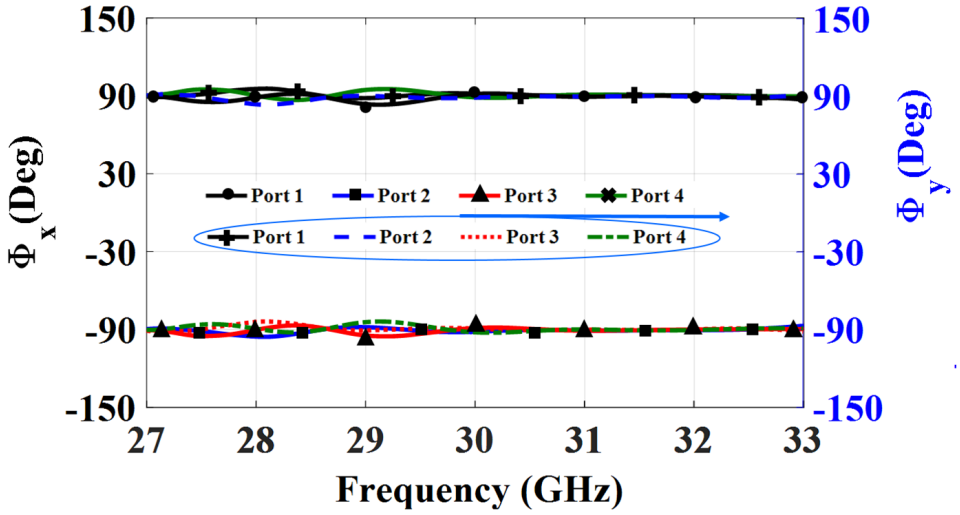

(b)

Figure 4.4: (a) Simulated S-parameters of the PRGW Butler matrix. (b) Output phase differences.

27-33 GHz bandwidth. The simulated transmission coefficients of port 1 is -6.5 dB with maximum deviation of ± 1.6 dB. Fig. 4.4(b) shows the simulated phase differences $\Phi_x = \angle S_{5p} - \angle S_{6p} + 180^o$ and $\Phi_y = \angle S_{5p} - \angle S_{8p}$ along the x-axis and y-axis, respectively, when one of the input ports is excited (p=1-4), while each one of the output ports is terminated with 50Ω load. The simulated phase differences Φ_x and Φ_y are very close to 90^o and -90^o which are in an excellent agreement with desired theoretical results. The proposed PRGW Butler matrix shows the maximum simulated phase errors of ± 5^o over the whole frequency band.

Table 4.2: Dimensions of hybrid coupler in millimeters

Parameters	W	L	W_R	a	ΔL_1	Δw_1	ΔL_2	Δw_2
Values	7	6.3	1.6	1.8	0.5	1.5	3.8	0.3

Table 4.3: Dimensions of ME-dipole antenna in millimeters

Parameters	L_{stub}	D_{stub}	L_s	L_d	W_s	W_d	h_a
Values	1.6	1.3	0.4	2.2	3.8	4.4	0.508

4.2 Magneto-Electric (ME)-Dipole Antenna Element

The ME-dipole antenna is adopted in this work as a radiation element to be integrated with the beam switching network and forming a beam scanning antenna array. The ME-dipole antenna has recently attracted considerable attention due to the combination of the two fundamental types of radiators, namely, magnetic and electric dipoles. Such antenna offers enhanced performance compared to other radiators such as electric dipoles and slot antennas [152]- [153]. The concept of ME-dipole antenna is based on exciting simultaneously an electric dipole and a magnetic dipole, which yields identical E- and H-plane far-field stable radiation patterns, and low back radiation with low cross-polarization over a wide frequency bandwidth [29]. Furthermore, it has a sufficient beamwidth in both E-and H-plane with a compact size, which is desirable for beam switching networks [74,80]. In this work, a compact magneto-electric dipole antenna is implemented based on PRGW technology which exhibits a wide impedance matching bandwidth.

The geometry of the proposed ME-dipole antenna is presented in Fig. 4.5, which consists of two Rogers RT6002 PCB laminates with dielectric constant $\varepsilon_r = 2.94$. Detailed dimensions of the proposed antenna are indicated in Table 4.3. The proposed antenna is composed of two patches connected to the ground through rows of metallic vias forming an electrical dipole on the top substrate, while the magnetic dipole is realized by the rectangular hole between the patches. This rectangular hole is extended to the bottom layer of the top substrate, which used as a feeding slot excited by a PRGW line printed on the bottom substrate. A good impedance matching is hard to achieve if the above configuration is fed only by a feeding slot etched on the ground plane. Therefore, a circular short circuit stub connected to the feeding line is deployed to achieve a deep matching level. The simulated reflection coefficient of the proposed antenna with and without stub

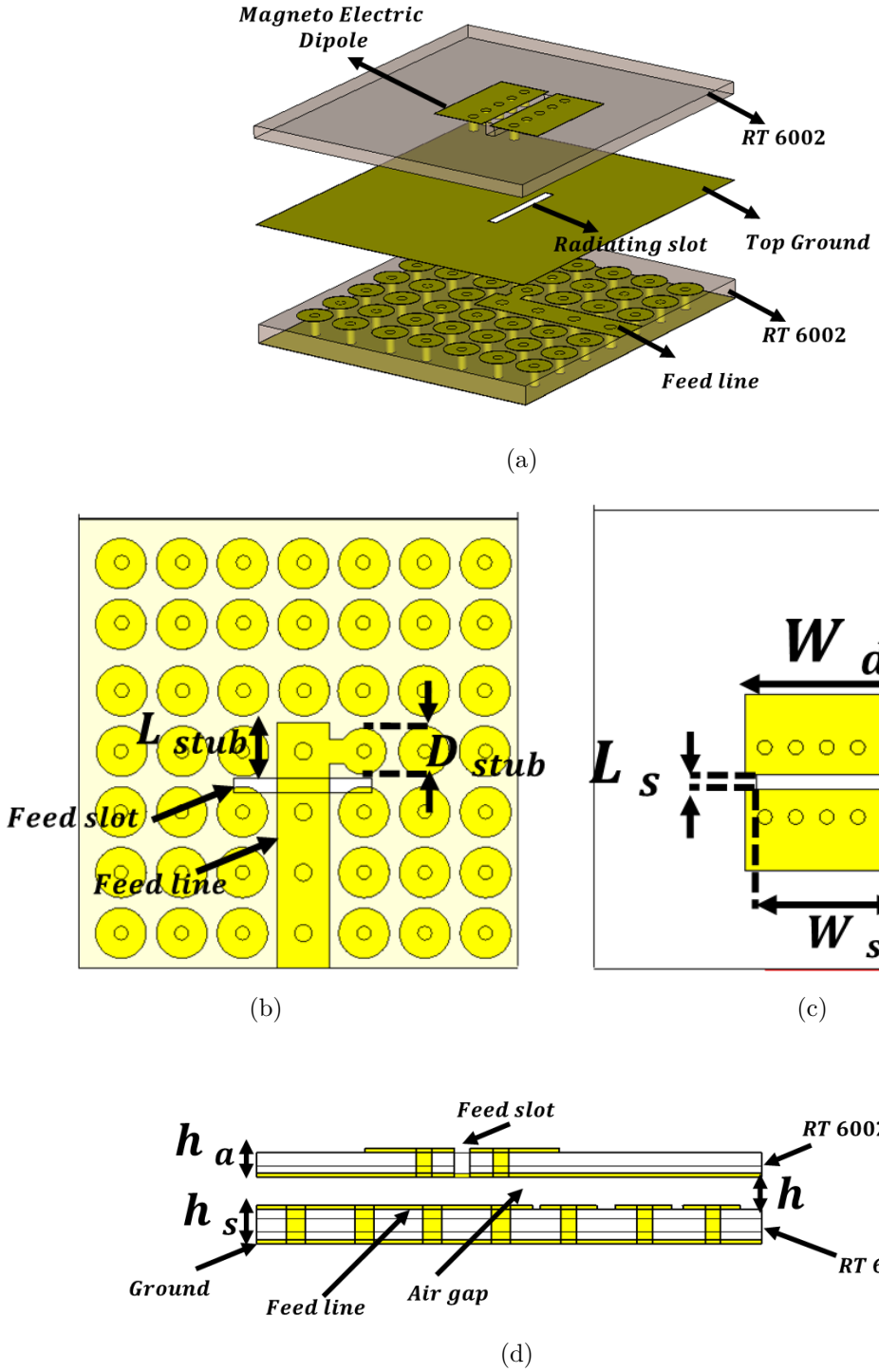

Figure 4.5: The geometry of the proposed antenna: (a) 3-D view; (b) bottom view; (c) top view; (d) side view.

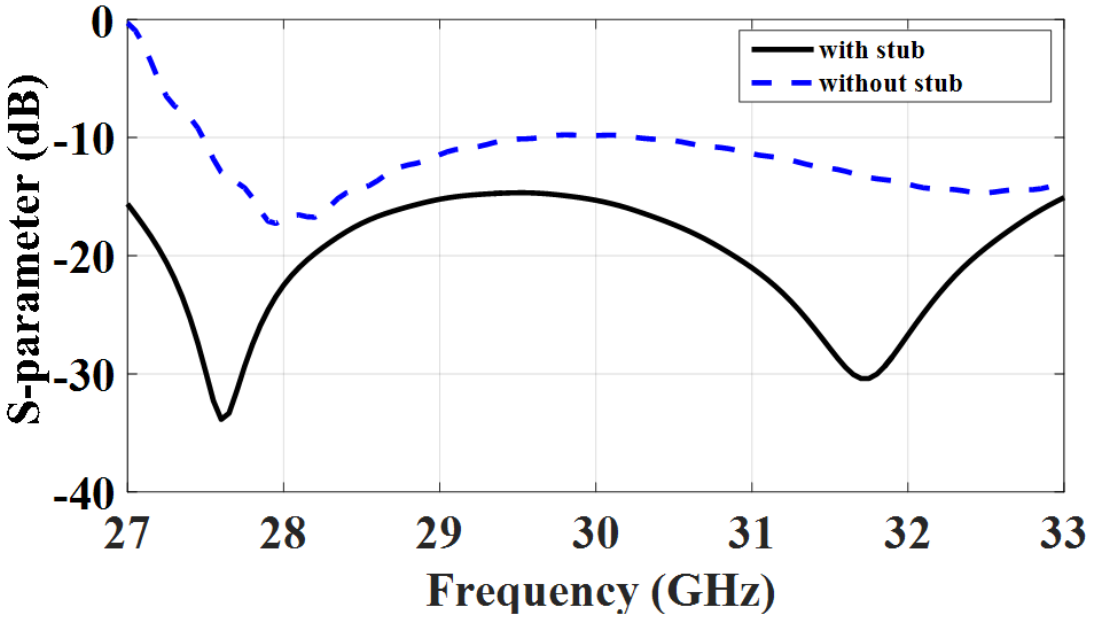

(a)

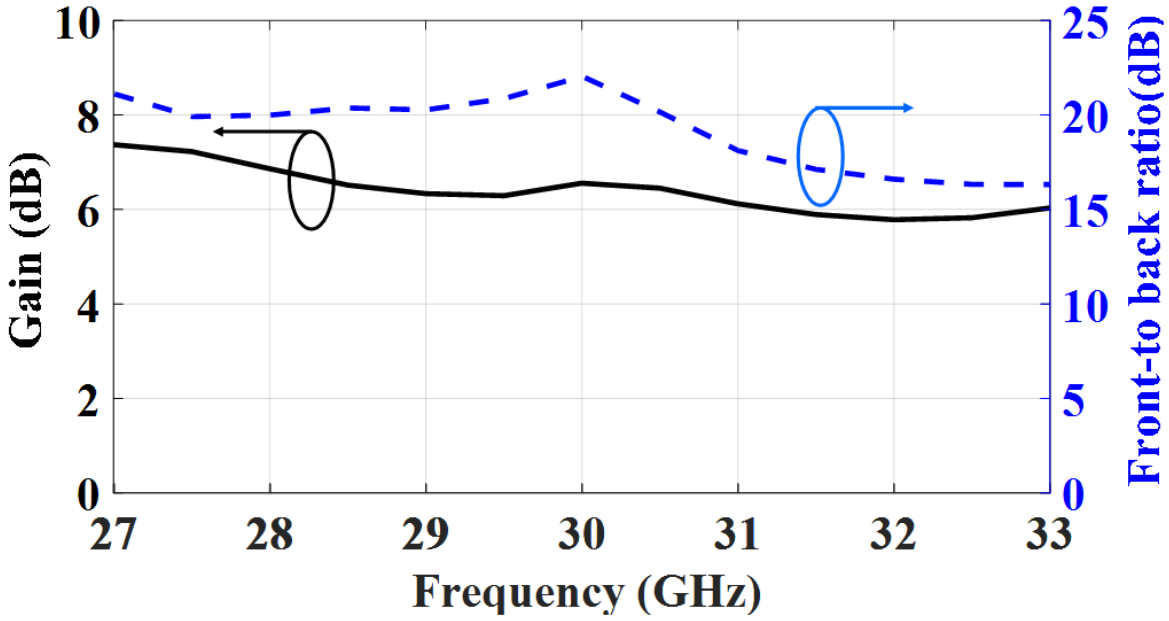

(b)

Figure 4.6: (a) The simulated reflection coefficient .(b) The realized gain and front-to-back ratio of the proposed antenna.

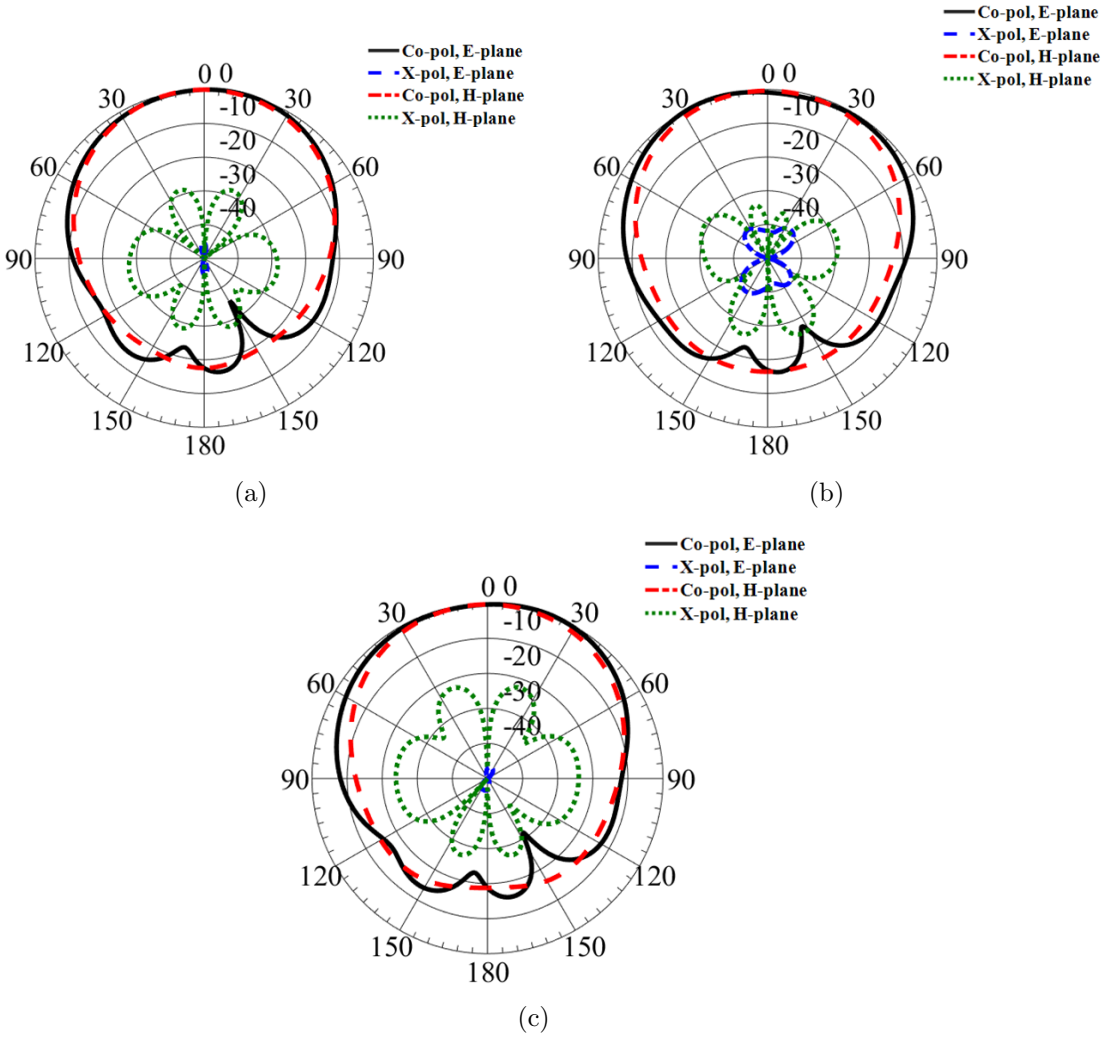

Figure 4.7: The simulated radiation pattern at: (a) F=27 GHz; (b) F=30 GHz; (c) F=33 GHz.

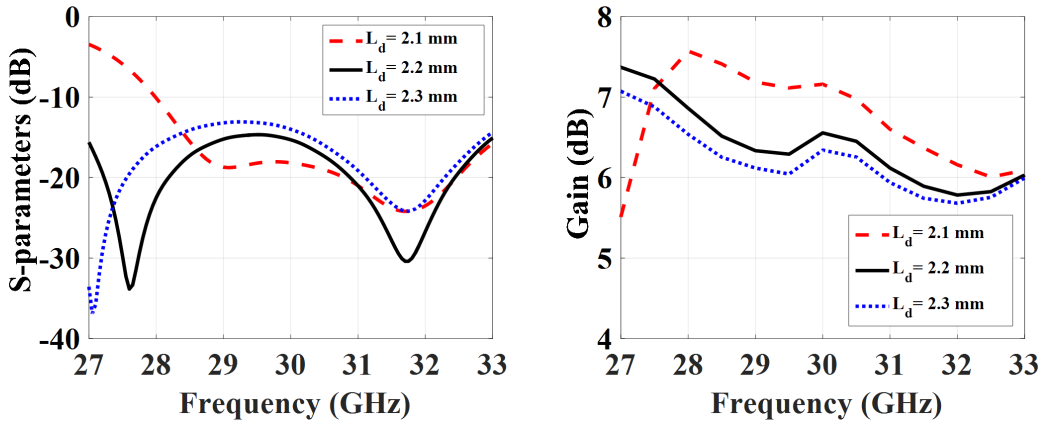

(a)

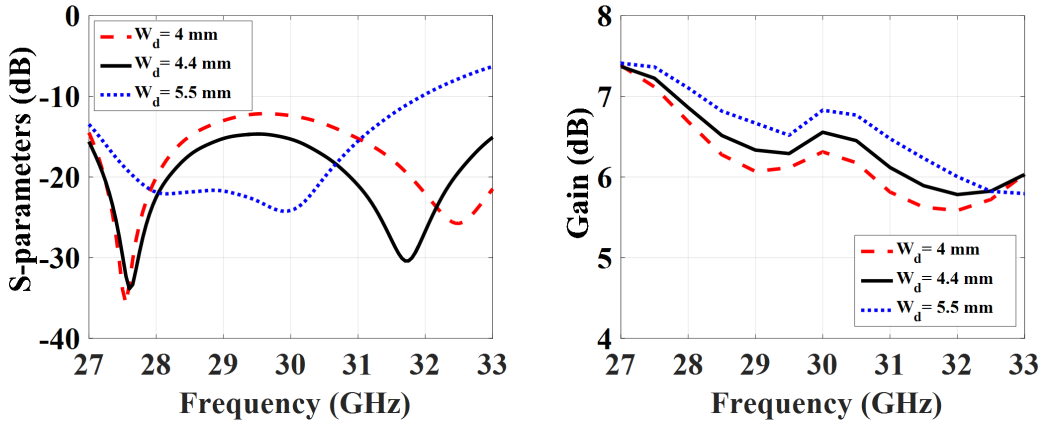

(b)

Figure 4.8: Simulated S-parameter, gain, front-to-back ratio at different ME-dipole parameters: (a) L_d; (b) W_d.

is presented in Fig. 4.6(a). It can be noticed that the matching level is significantly improved in the existence of the matching stub which demonstrates the effectiveness of its use. The proposed antenna has a wide bandwidth of 20% at 30 GHz with -15 dB matching level. Fig. 4.6(b) exhibits stable simulated gain results of the proposed antenna around 6.5± 0.5 dB with front-to-back ratio larger than 15 dB over the whole frequency band. Simulated radiation patterns of the proposed antenna at different frequencies are exhibited in Fig. 4.7. They are stable and symmetrical over the whole operating band with a low cross-polarization level in both E- and H-planes.

To understand the impact of different ME-dipole geometrical parameters on S-parameter, gain, and front-to-back ratio, parametric studies are performed by sweeping one of the parameters while the others are kept constant. Figs. 4.8(a) and 4.8(b) show the simulation results for reflection coefficient and gain for different dipole length L_d and width W_d.

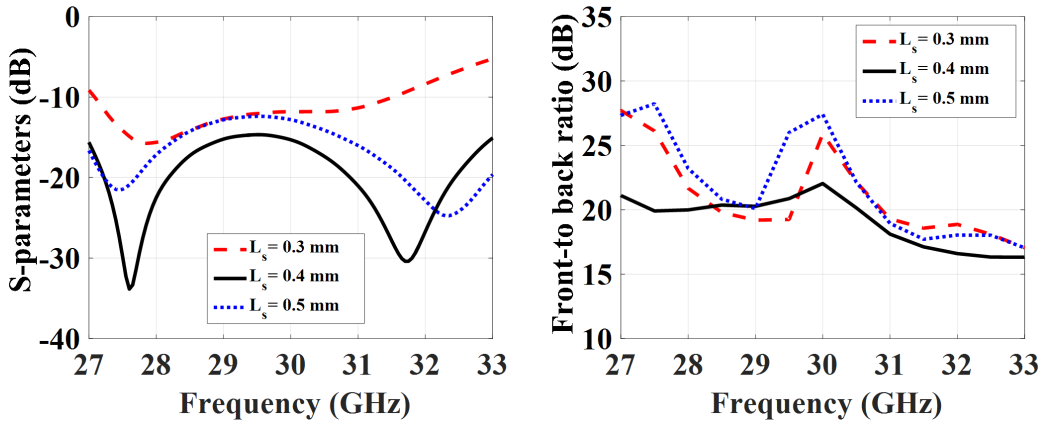

(a)

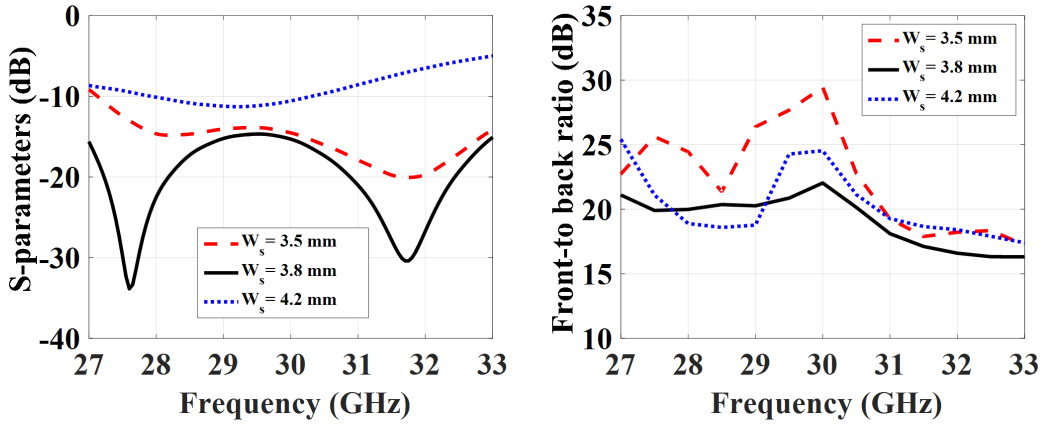

(b)

Figure 4.9: Simulated S-parameter, gain, front-to-back ratio at different ME-dipole parameters: (a) L_s; (a) W_s.

It can be depicted from these figures that the optimum values for L_d and W_d are 2.2 and 4.4 mm, respectively, and both L_d and W_d mainly affect the impedance matching rather than the gain. Figs. 4.9(a) and 4.9(b) study the reflection coefficient and front-to-back ratio at different slot sizes. It can be noticed that the optimum values for L_s and W_s are 0.4 and 3.8 mm, respectively. Both L_s and W_s parameters mainly affect the impedance matching and the front-to-back ratio.

The proposed ME-dipole antenna exhibits a low profile with low fabrication cost compared with the substrate integrated electric dipole in [152] and mesh grid antenna in [153] with large sizes and complicated 5-layer fabrication process. The ME-dipole antenna in [31], which is implemented in the inverted microstrip line gap waveguide technology has a larger size since the microstrip line and mushroom surface do not share the same substrate as the case of the PRGW technology used to excite the proposed ME-dipole

antenna. In addition, considering a -15 dB matching level, the proposed antenna achieves a 20% bandwidth compared with 8.3 % for the ME-dipole antenna in [31]. Based on the previously reported superior features of the proposed ME-dipole antenna compared with other radiators reported in the literature, the proposed antenna is considered as a good candidate for integration with the designed beam switching network presented in the previous section.

4.3 2-D Scanning Antenna Array

The above PRGW Butler matrix and the ME-dipole antenna are integrated to form a 2-D scanning beam switching network shown in Fig. 4.10. The inter-element spacing for the array in x- and y-direction are $d_x = 0.6\lambda$ and $d_y = 0.54\lambda$, where λ is a free space wavelength at 30 GHz. Applying the analysis discussed in the previous section and taking into consideration the exact inter-element spacing values d_x and d_y at 30 GHz with the progressive phase shift Φ_x and Φ_y shown in Fig. 4.4(b), four scanning beams with beam angle direction θ_o and Φ_o are calculated as (35^o,-135^o), (35^o,-45^o), (35^o,45^o), and (35^o,135^o) when fed from port 1 to port 4, respectively. Figure 4.11 shows the simulated radiation patterns at 30 GHz when different input ports are excited. All the previous designed components are assembled together to construct the 2-D scanning antenna array shown in Fig.4.10, where the simulated S-parameter, radiation pattern, gain, and efficiency will be compared with the measurement in the experimental validation section.

4.4 Experimental Validation

The proposed 2-D scanning antenna array is fabricated and measured. The fabricated parts are shown in Fig. 4.12(a). These parts are printed on Rogers RT6002 with relative dielectric constant ε_r =2.94 and loss tangent of 0.0012. Multiple plastic screws at the edges of substrates are used to align the fabricated parts together. The S-parameters of the proposed scanning array is measured by an N52271A PNA network analyzer, where the measured S-parameters and isolation of the proposed antenna array when the excitation from port 1 are shown in Fig. 4.12(b), which demonstrates that both matching and isolation levels are less than -10 dB over the frequency band of interest (from 27 to 33 GHz). The simulated and measured results are in a good agreement as illustrated in

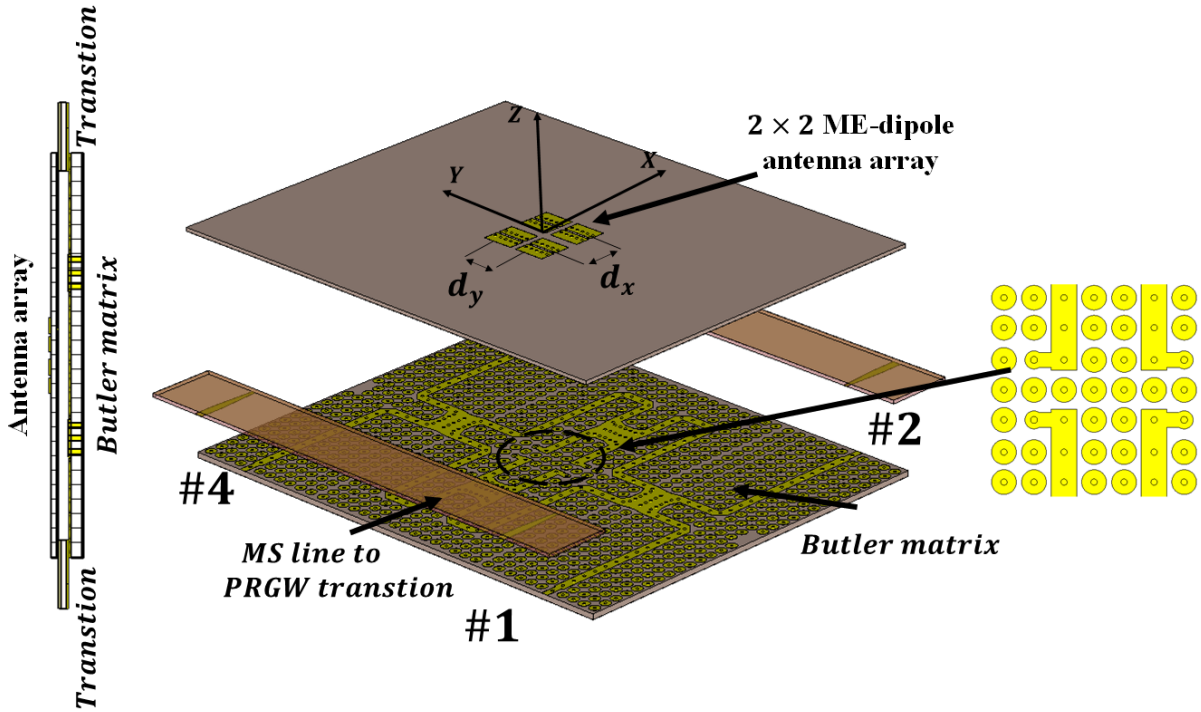

Figure 4.10: 3-D view of the proposed scanning antenna array.

Fig.4.12(b). The gain and radiation pattern measurement were performed in the anechoic chamber system, as shown in Fig. 4.13. The far-field measurement setup is adjusted by moving the array along with the horn antenna only in the upper hemisphere (-120 ^{o} to 120 ^{o}) at an interval of 5^o due to the system limitation.

Measured and simulated 2-D radiation patterns when the excitation from port 1 and port 3 are presented in Fig 4.14. The radiation patterns are stable over the whole operating frequency band, where the maximum radiation is noticed at elevation angle 35^o with low sidelobe level less than -15 dB.The measured HPBW is approximately 46^o and 44 ^{o} for ports 1 and 3, respectively, at 30 GHz. Furthermore, both radiation patterns with excitation from port 1 (Φ= 45^o) or port 3 (Φ= 135^o) are very close to each other. Theoretically, the expected gain for the proposed scanning array should be higher than 12 dB, however, a drop of 1.5 dB in the simulated gain is achieved. This drop mainly from both the scan and the feeding network losses. The simulated and measured gain of the proposed array when the excitation from port 1 is shown in Fig.4.15. This figure demonstrates that the measured gain is 9.7 $\pm$ 0.4 dB, which is in a good agreement with the simulated gain. The discrepancy in the measured gain may be due to measurement

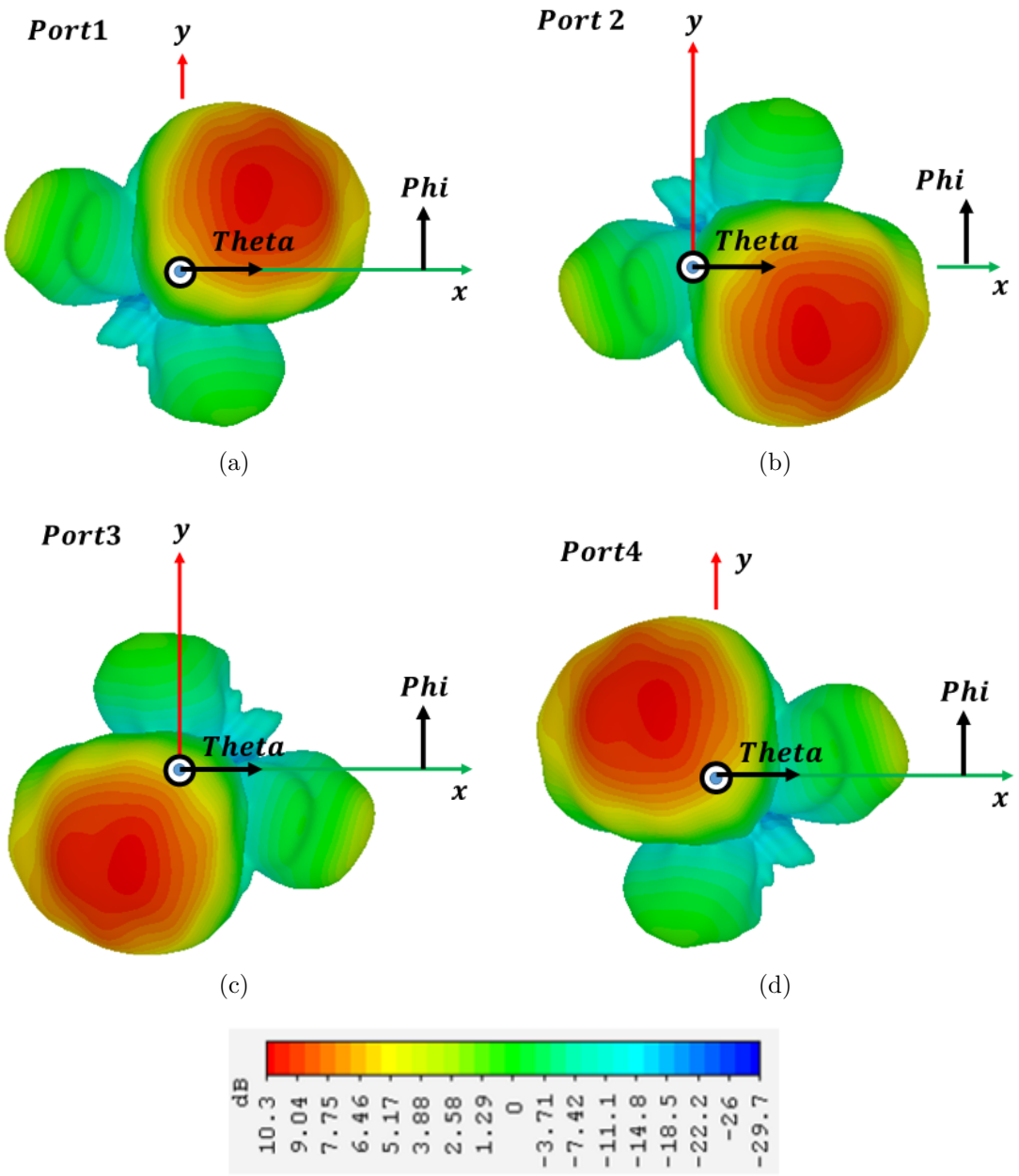

Figure 4.11: Simulated radiation patterns at 30 GHz. (a) port 1 excited. (b) port 2 excited. (c) port 3 excited. (d) port 4 excited.

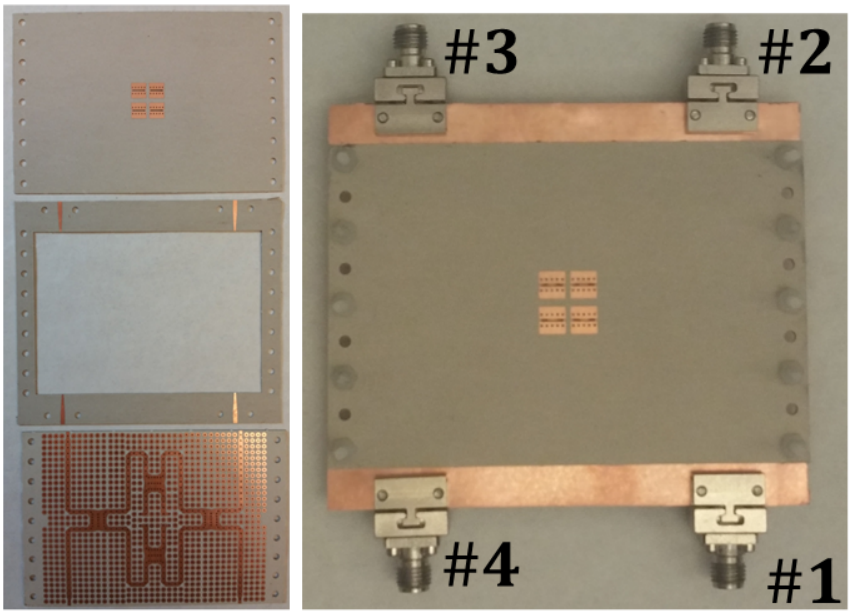

(a)

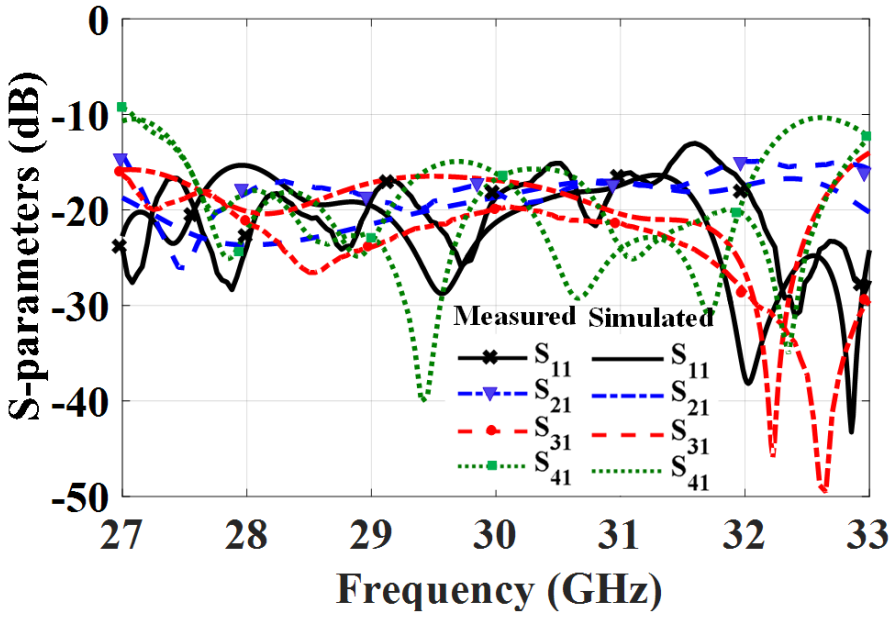

(b)

Figure 4.12: (a) Fabrication of the proposed 2-D scanning antenna array . (b)Simulation and measured S-parameters.

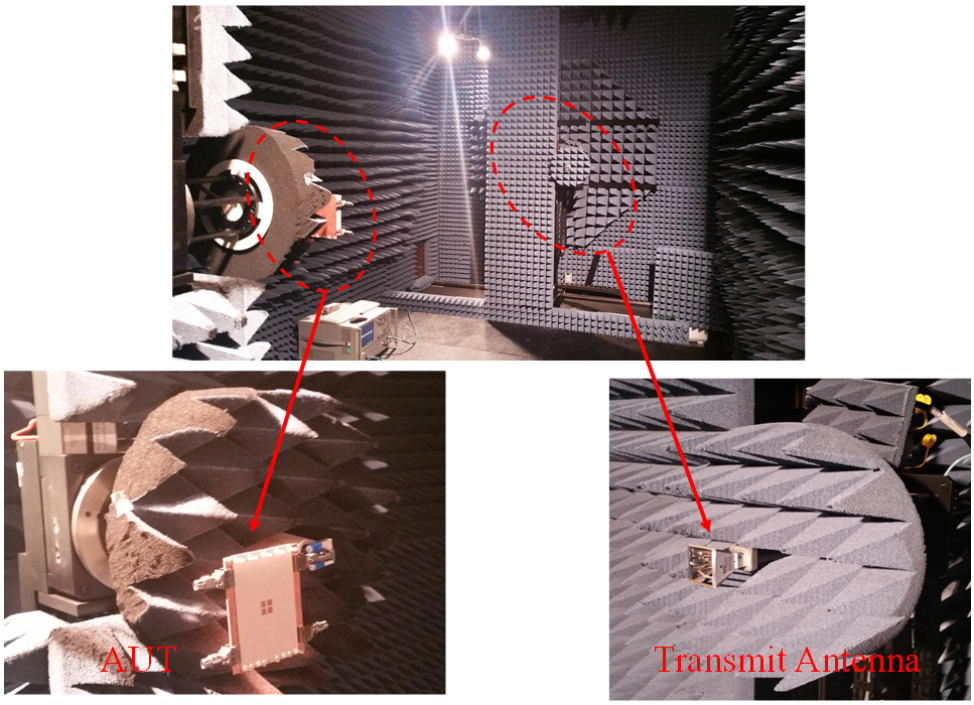

Figure 4.13: Radiation pattern measurement setup.

system tolerance and alignment as well as the fabrication tolerance of the proposed array. Also, the losses of the microstrip line transition and the connector have not been calibrated. Due to the difficulty in measuring the directivity using the available facility, only the simulation radiation efficiency is shown in Fig. 4.15. It can be observed that the proposed antenna array achieves a radiation efficiency of 84 % with small variation over the frequency band of interest.

4.5 Performance Evaluation

The performance of this work is evaluated through a comparison between the proposed 2-D scanning antenna array and other reported scanning array implemented with different guiding technologies. This comparison is summarized in Table 4.4. The proposed scanning array is implemented using a printed RGW technology that exhibited superior characteristics at mmWave frequency bands including low loss since the wave propagates inside the air gap instead of a dielectric. This feature results in high radiation efficiency larger than 84%, while other scanning array implemented using substrate integrated waveguide (SIW) technology have a radiation efficiency that does not exceed 70% as indicated in Table.4.4. Moreover, the proposed design has a compact size of $5.6\lambda \times 7.1\lambda$ with a wide impedance

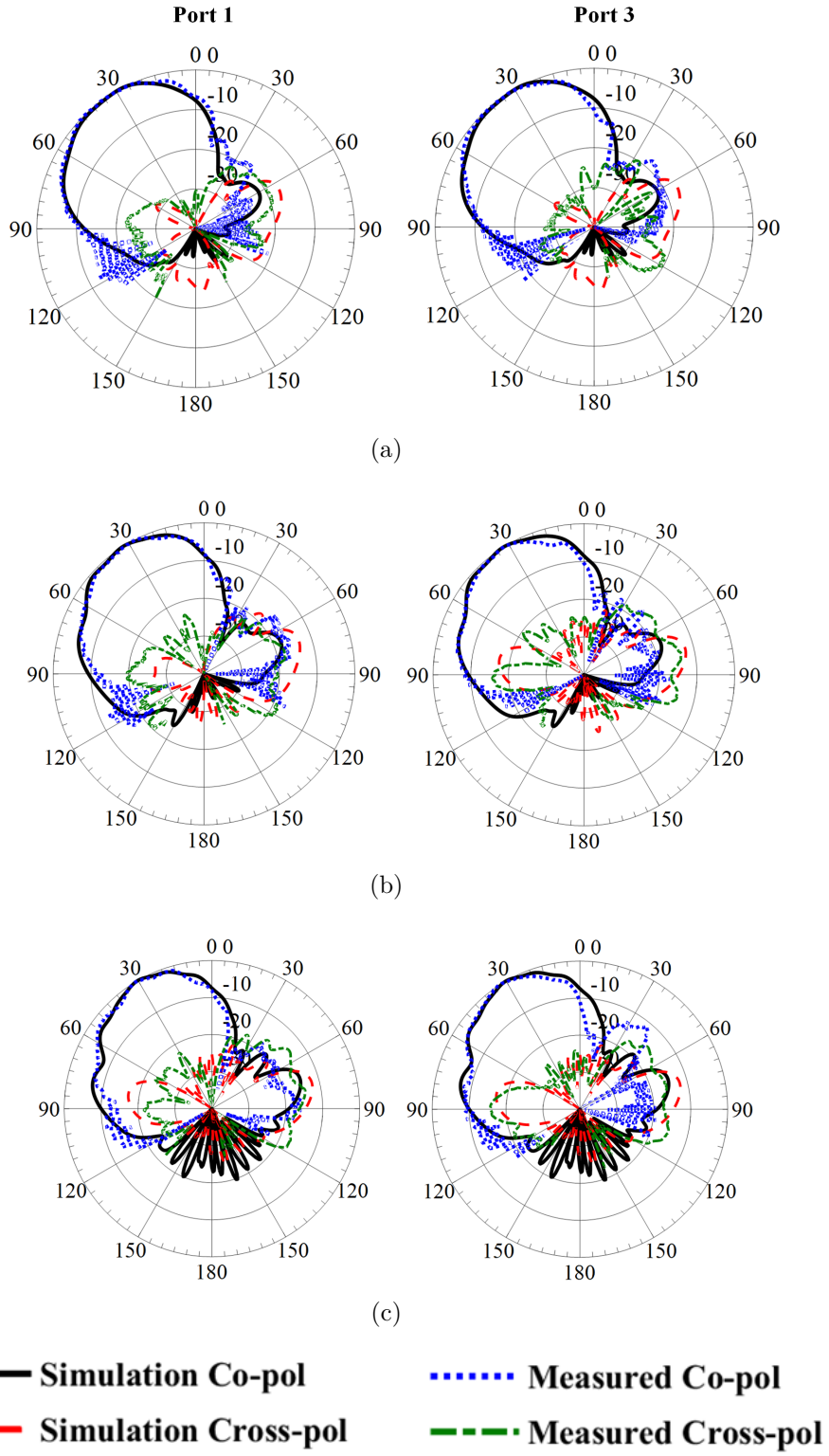

Figure 4.14: Measured and simulated 2-D radiation pattern for excitation from port 1 (left Φ= 45^o) and port 3 (rightΦ= 135^o): (a) F=27 GHz; (b) F=30 GHz; (c) F=33 GHz.

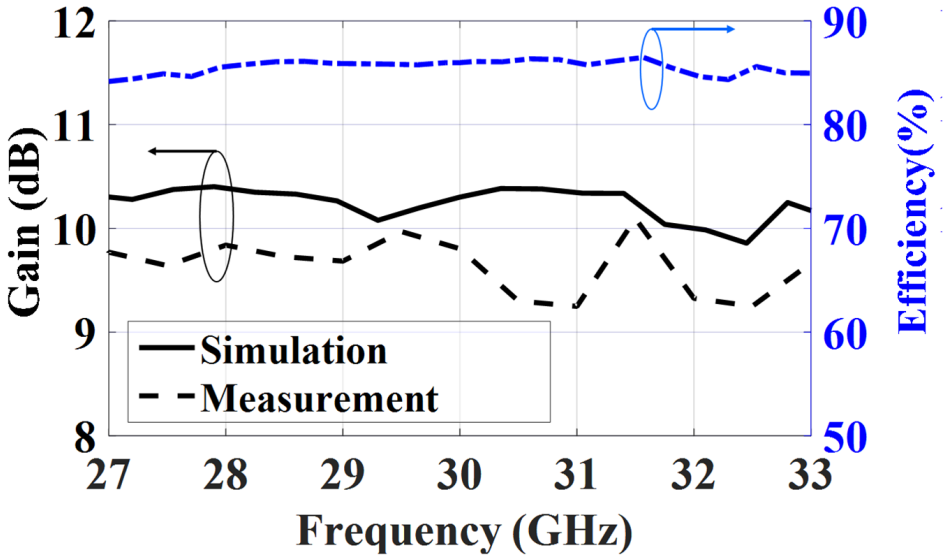

Figure 4.15: Measured and simulated gain and efficiency of the proposed scanning antenna array.

Table 4.4: Comparison between different 2-D scanning antenna array configurations designed at 30 GHz band

Ref.	BSN structure	Antenna array	BW/ Gain	Efficiency	Side lobe/ HPBWs	Size ($\lambda \times \lambda$)
[74]	Four layers	2×2	7.5%/ 12 dB	68.7 % (Measured)	-14.6 dB/ 28^o, 39^o	2.86 λ × 2.86 λ
[75]	Three layers	8×10	2.6%/ 20.4 dB	Not indicated	-10 dB/ Not indicated	7.6 λ × 8.2 λ
[76]	Four layers	4×4	13.3%/ 13.2 dB	Not indicated	-12 dB/ Not indicated	4.5 λ × 16.5 λ
[77]	One layers	4×4	13.3%/ 12.5 dB	46% (Measured)	-10 dB/ 30^o, 32^o	8 λ × 7 λ
This work	Two layers	2×2	20%/ 10.3 dB	84 % (Simulated)	-17 dB/ 44^o, 46^o	5.6 λ × 7.1 λ

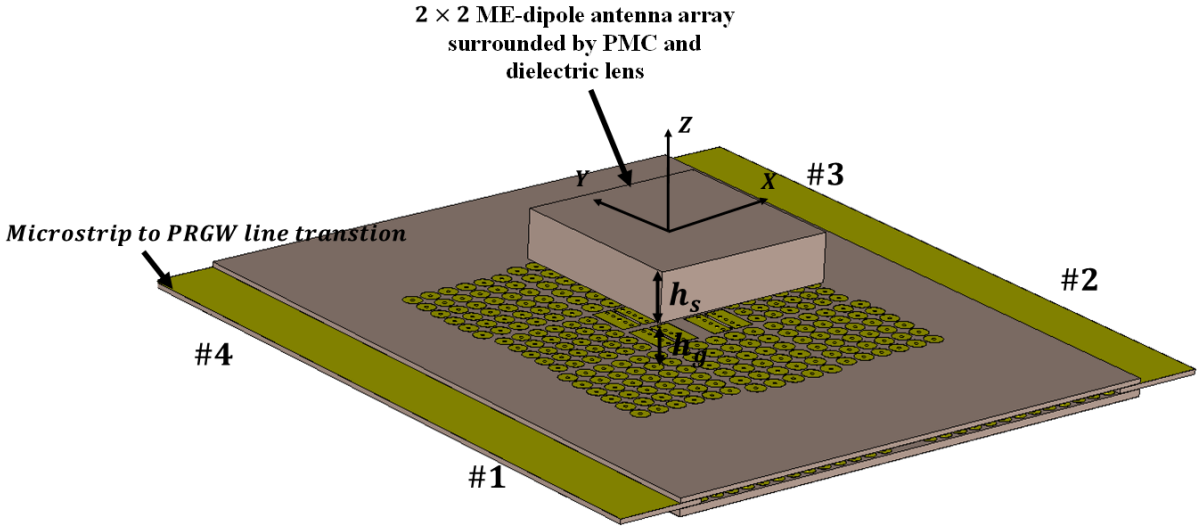

(a)

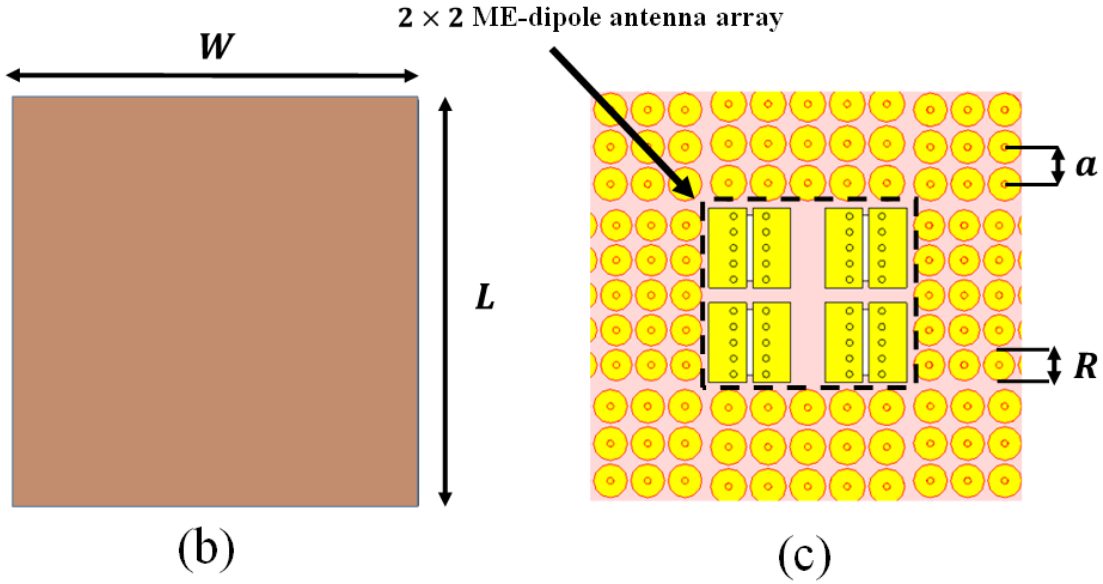

Figure 4.16: (a) 3-D view the proposed high gain scanning antenna array. (b) dielectric substrate lens. (c) Mushroom unit cell for AMC surface.

Table 4.5: Dimensions of the lens and AMC mushroom unit cell in millimeters

Dimension	Value
Superstrate length (L)	20
Superstrate width (W)	20
Superstrate thickness (h_s)	6.4
Superstrate height (h_g)	5.1
Unit cell period (a)	2
Unit cell diameter (R)	1.83

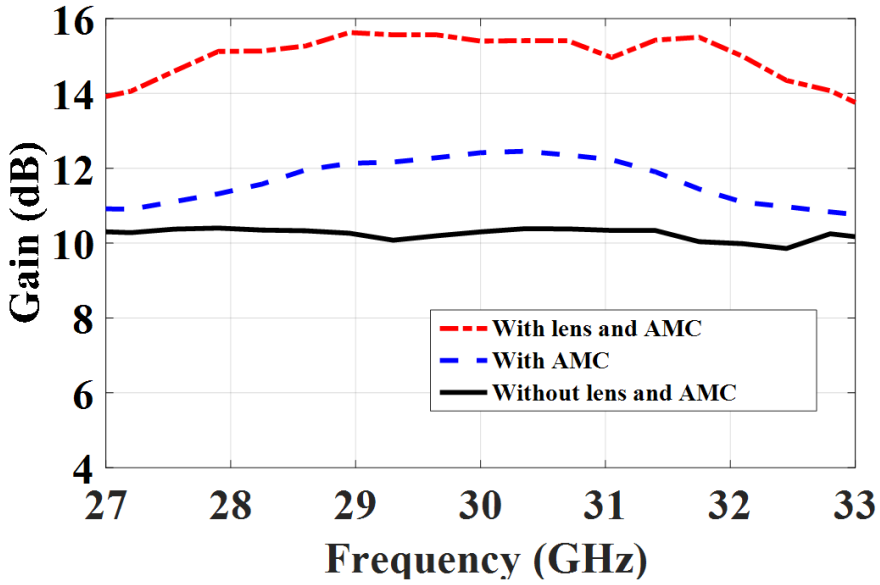

Figure 4.17: The effect of lens and AMC on the simulated gain.

bandwidth of 20 % at 30 GHz which is wider than most of 2-D scanning antenna array reported in [74–77]. For example, compared with the SIW antenna array in [74], which consisted of four-layers stacked on top of each other and has a higher gain, the proposed antenna array has a wider bandwidth, lower profile, and higher radiation efficiency. In addition, the proposed scanning antenna array has the lowest side lobe level with wide beamwidth. In order to enhance the coverage capability of the proposed scanning antenna array, a hybrid gain enhancement technique is proposed. Fig. 4.16(a) demonstrates the 2-D scanning antenna array incorporated with the proposed hybrid gain enhancement technique, which includes an AMC mushroom shape around the antenna array with a dielectric superstrate located into the broadside direction. First, the AMC surface implemented with a mushroom shape unit cell is placed around the 2×2 ME-dipole antenna array as shown in Fig. 4.16(b). Different approaches for the realization of the AMC are introduced in the literature, where the use of a mushroom shape can be considered the most effective and simple technique that features a wide operating bandwidth. This AMC is deployed to improve the antenna array gain in the operating frequency band by adjusting the dimension of EBG mushroom shape unit cells and the spacing between the radiating element and the AMC surface, where the optimum dimensions are listed in Table. 4.5. This results in a 2.5 dB gain improvement at the center operating frequency as shown in Fig. 4.17. This gain enhancement is due to the suppression of surface waves excited in the dielectric substrate that results in a great improvement for the sidelobe levels and

front to back ratios. Further gain improvement is achieved by using a superstrate that is realized using a dielectric Roger RT 5880 substrate with dielectric constants ε_r= 2.2. The main function of the superstrate is creating successive in-phase bounces of the trapped waves between the superstrat and the AMC surface. As a result, a high gain is achieved due to the constructive addition in the scanning direction. The superstrate is located approximately at $\lambda_o/2$ from the surface of the antenna array, where the width, length, and thickness of the superstrate are tuning to maximize the gain and the matching of the scanning antenna array. Table. 4.5 indicates the optimum dimensions of the superstrate, where a 5.5 dB gain improvement at the center operating frequency is achieved as shown in Fig. 4.17. Therefore, a high gain scanning antenna array with a stable gain of 15± 1 dB over a wide bandwidth is achieved.

Chapter 5

Differential Feeding Antenna Arrays Fed by PRGW

Lately, there is an explosive growth in the research and development of the next-generation wireless communication systems to address the challenges associated with the existing technologies. Challenges include limited data rate and high-energy consumption. Therefore, mmWave and higher frequency bands will be utilized to accommodate the required high data rate enabling the development of new applications that will have a significant value to the society. In addition, the evolution of guiding structure technologies and antenna design will significantly improve the performance of a wireless system from a hardware perspective. Guiding structure technologies with low loss, minimal dispersion, low cost, and wide bandwidth are strongly recommended at mmWave frequency bands. One of the states of art printed guiding structures is the printed ridge gap waveguide (PRGW) technology which demonstrated superior features at mmWave frequencies in the last few years. This technology is deployed many times in literature to implement either microwave components such as hybrid couplers and filters or as a feeding network to feed antenna arrays [27, 28, 154, 155]. High-performance antenna arrays are no less important as they are necessary for the future wireless communication systems. They should feature with high gain, wide bandwidth, and low cross-polarization to overcome the path losses associated with mmWave frequencies. Although high antenna gains can compensate for the losses experienced by mmWave transmissions, a slight movement of the antenna array may result in degradation of the receiver sensitivity due to the main beam misalignment. Therefore, circularly polarized antenna array designs offer advantages for mmWave communications as they can receive a signal in the presence of misalignment between transmitters and receivers. In addition, being easy to be integrated with differential mmWave monolithic ICs that have a high common-mode rejection ratio, immunity

of interference, and large-dynamic range is essential to facilitate the design complexity of the RF front-end. This can be achieved by designing differential feeding antennas instead of single-ended feed. As a consequence, a low cross-polarization level with high noise immunity can be achieved, which can improve the receiver sensitivity of the emerging communication systems. Also, other antenna techniques such as a dual-polarization are considered an effective antenna solution for the improvement of the communications link by reducing the multi-path fading loss and enabling the polarization diversity.

To further enhancement the reliability of the wireless communication link through improving the receiver noise sensitivity and enabling the polarization diversity, mmWave differential feeding antenna arrays having different polarization techniques are presented in this chapter. First, a differential feeding circularly polarized antenna array implemented with PRGW technology for mmWave applications is presented. The proposed antenna array is differentially fed, which offers the advantage of easy integration with differential mmWave monolithic ICs. It is a planar structure realized by a rectangular aperture incorporated with a circular-shaped polarizer to achieve a CP radiation. The proposed antenna array is fabricated and measured, where a wide measured bandwidth is achieved. Also, the proposed array is achieved a high radiation efficiency of 84% over the entire bandwidth. This performance makes the proposed CP antenna array an attractive candidate for practical millimeter-wave applications at 30 GHz frequency band. Second, a dual-polarized ME-dipole antenna based on PRGW technology is presented. A cross-shaped dipole backed by a square AMC side walls cavity is deployed to achieve a radiating antenna with dual polarization. Two feeding PRGW lines located at different layers are used to excite the dual-polarized antenna through the square cavity. A cross-shaped slot is etched on the upper ground of the cavity to excited the ME-dipole antenna. The proposed antenna is fabricated and measured where a good agreement between the simulation and measured results is observed. The fabricated prototype is shown an overlapped wide bandwidth at 30 GHz, where a high isolation level between the two excited ports is achieved over the whole bandwidth. A stable gain with low sidelobe level radiation patterns is achieved through using an AMC surface around the ME-dipole antenna. The proposed antenna is deployed to construct a 2×2 antenna array that is fed by a 1×4 differential power dividers. As a result, the proposed dual-polarized array is achieved a stable gain with low cross-polarization over a wide bandwidth.

Table 5.1: Dimensions of differential feeding power divider

Parameters	a	L_{t1}	W_{t1}	L_f	W_{R1}	W_f	L_s
Values	1.8	2.85	1.6	5.5	1.37	0.65	1.9
Parameters	W_s	L_i	W_i	W_{R2}	h_1	h_2	h_3
Values	5	0.34	4	1.37	0.5	0.5	0.127

5.1 Differential Feeding Circularly Polarized Antenna Array

5.1.1 Differential Feeding PRGW Power Divider

In order to achieve a stable 180^o phase difference between the output ports, a power divider formed by two layers coupled through an I-shape slot is shown in Fig. 5.1(a). The input port of the divider is located in the bottom layer, where the input signal propagates through a PRGW line. To provide a proper coupling as well as a deep impedance matching, the feeding PRGW line in the lower layer is terminated with a matching stub as shown in Fig. 5.1(b). The $\lambda/2$ length I-shape coupling slot is incorporated with two opposite PRGW lines to provide equally split signals with 180^o phase difference to the output ports as shown in Fig. 5.1(b). Both PRGW lines located in the upper and bottom layers are designed using an EBG unit cell, which is printed on RO3003 substrate with a relative dielectric constant of 3 and a thickness of 0.5 mm. The PRGW line and EBG unit cell characteristics and dimensions are well addressed before in literature to achieve a certain bandwidth [38, 154, 155]. Here, the EBG unit cell has a unit cell period = 1.8 mm and gap height = 0.254 mm, which result in a band gap from 23 to 36 GHz [42]. The dimensions of proposed power divider are listed in Table 5.1. Its simulated S-parameters are shown in Fig. 5.2. This figure shows that the proposed power divider achieves a deep matching level less than -15 dB over a 20 % relative bandwidth at 30 GHz. In addition, the power is divided equally into the two output ports with 180^o phase difference and 0.3 dB insertion loss. This power divider will be deployed to feed the differentially fed CP antenna as will be presented in the following section.

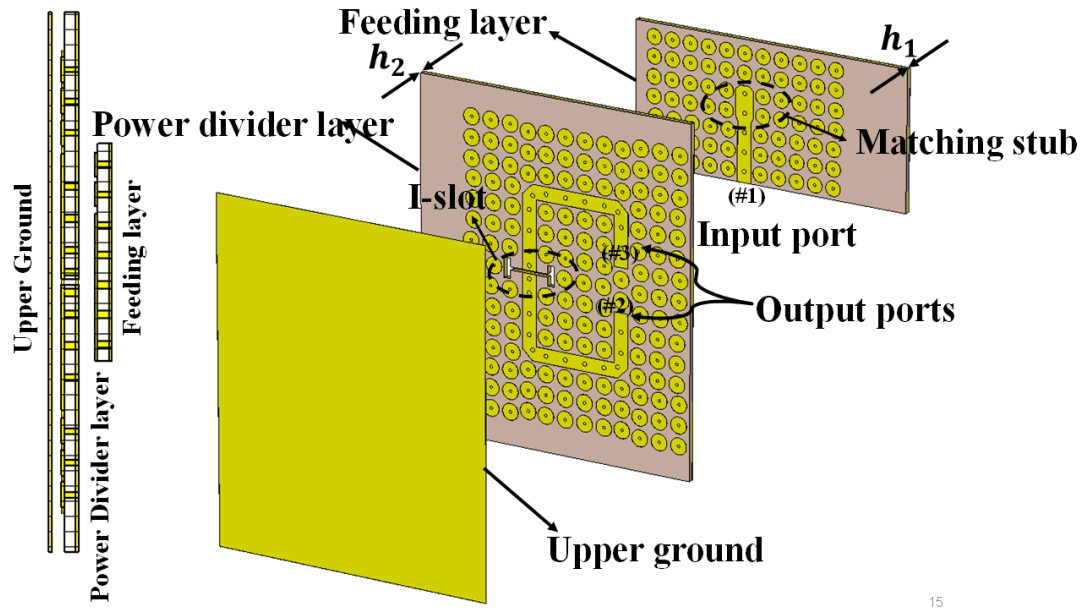

(a)

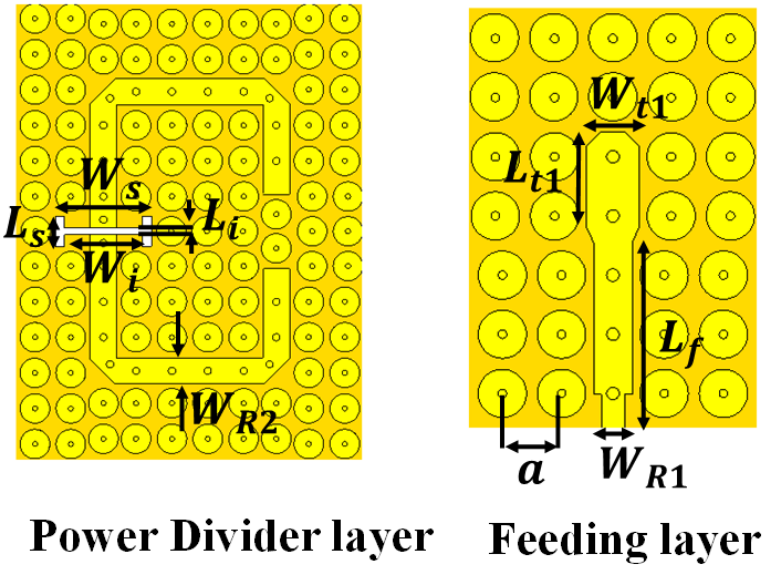

(b)

Figure 5.1: (a) 3-D view of differential feeding power divider. (b) Geometries of two layers.

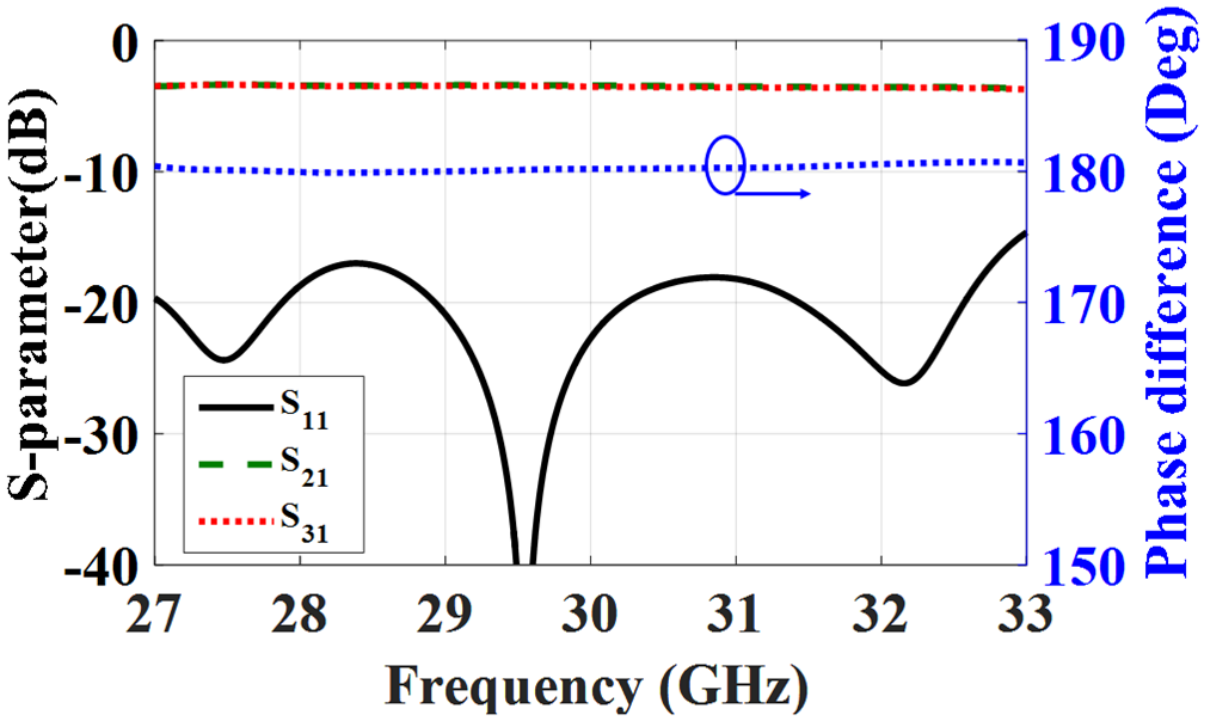

Figure 5.2: Simulated S-parameters of the differential fed power divider.

5.1.2 Single Element Antenna Design

Most of the existing mmWave CP antennas are mainly based on using a feeding network exciting radiating elements (patches or slots) with equal amplitude and 90^o phase difference, which have a narrow band performance [156, 157]. However, few trails are performed to excite a CP aperture antennas that have a wider bandwidth, especially at 30 GHz mmWave band. Accordingly, a perturbation method for an aperture antenna using a circular-shape polarizer to generate a CP wave is introduced. Fig. 5.3(a) shows a 3-D view of the proposed CP antenna fed by the designed differential feeding power divider. The geometrical configuration of the proposed antenna is shown in Fig. 5.3(b), which consists of a rectangular aperture having a circular-shape polarizer formed by patch surrounded by an open-end ring. The antenna is printed on RT 5880 with a relative dielectric constant of 2.2 and a thickness of 0.127 mm. The aperture size is selected to be $\lambda \times \lambda$ to have a large aperture efficiency and compact size. The antenna is optimized at 30 GHz, where the detailed dimensions of the proposed antenna are indicated in Table 5.2.

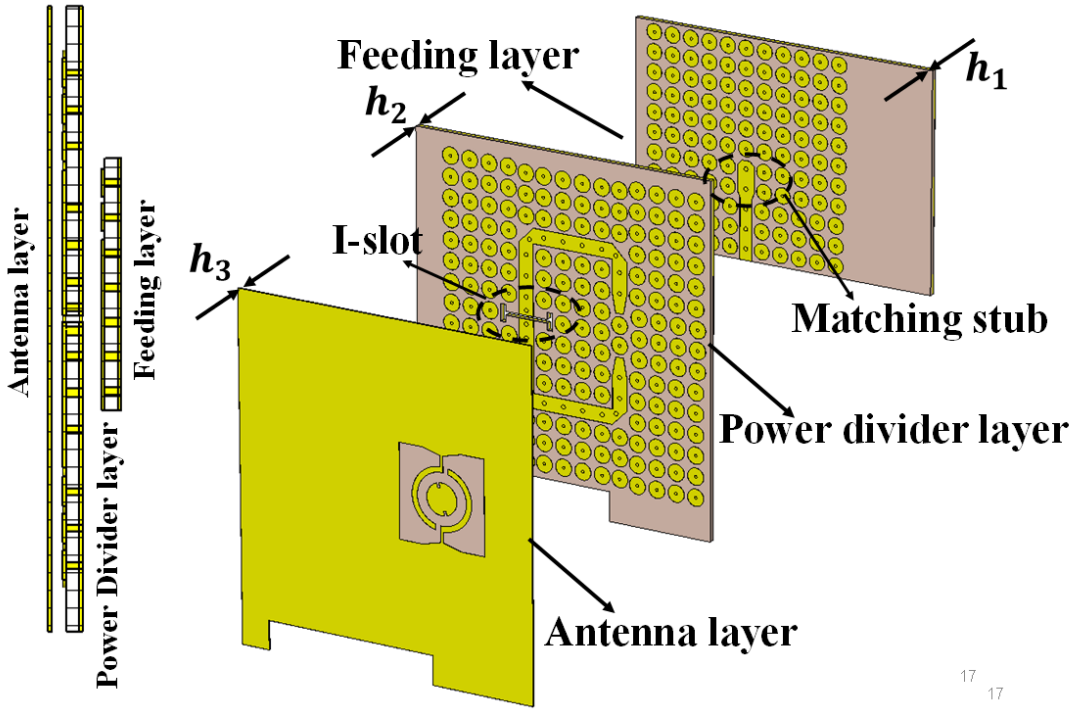

(a)

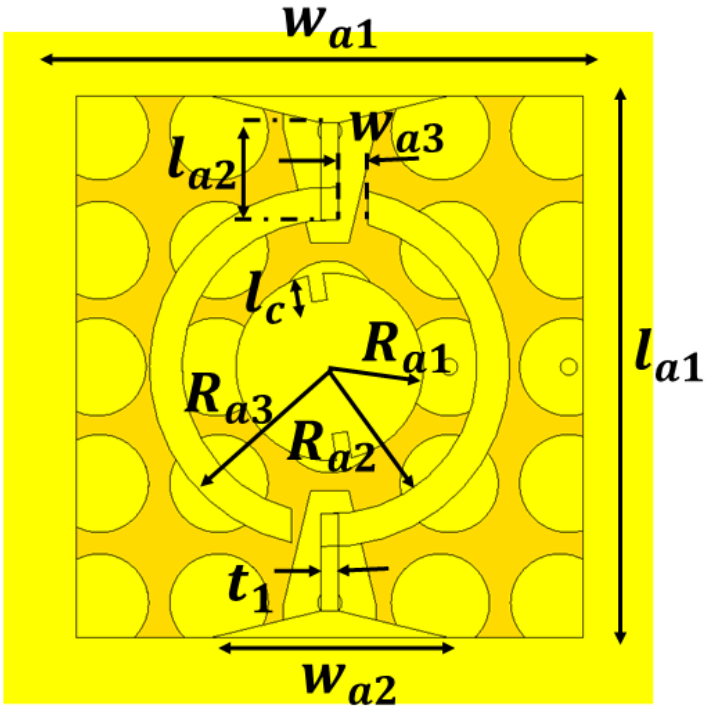

(b)

Figure 5.3: Geometry of the proposed CP differential feed antenna. (a) Perspective view. (b) Antenna top view.

Table 5.2: Dimensions of differential feeding antenna in millimeters

Parameters	w_{a1}	l_{a1}	w_{a2}	l_{a2}	w_{a3}
Values	8.2	8.6	3.7	1.47	0.5
Parameters	t_1	l_c	R_{a1}	R_{a2}	R_{a3}
Values	0.26	0.4	1.45	2.36	2.85

5.1.2.1 Working Principle

As shown in Fig. 5.4(a) the rectangular aperture antenna with a circular-shape closed ring polarizer is linearly polarized. The electric field distribution is shown in Fig. 5.4(a) indicates that along X-direction, the electric field distribution is symmetrical and out of phase, while along the Y-direction, the horizontal electric field distribution is symmetrical and in phase. As a result, the closed ring generates only E_y polarization along the Y-direction. In order to generate horizontal polarization, an open circular ring is introduced to perturb the horizontal electric field distribution and generates another polarization, i.e., -E_x polarization along the X-direction as shown in Fig. 5.4(b). As a result, the two polarization, E_y polarization, and -E_x polarization are forming pair of orthogonal modes that are introduced to achieve the first condition for circular polarization. In order to equalize the magnitude and adjust the quadrature-phase difference of these two modes, an open ring is incorporated with a patch having a pair of rectangular cuts and rotated with a proper angle with respect to the Y-axis. By adjusting the patch dimensions and the position of the cut, the two orthogonal polarizations can be generated with equal amplitudes and a 90^o phase shift. Consequently, the antenna generates a circular polarization. For the proposed antenna shown in Fig. 5.3(b), it generates right-hand circular polarization (RHCP). If the cuts on the ring are reversed, the antenna will generate left-hand circular polarization (LHCP). In addition, both the rectangular aperture and circular-shape open ring polarizer contribute in the radiation as observed from the simulated surface current distribution on the radiating element shown in Fig.5.4(c). As a consequence, a multi-resonance behavior and wide bandwidth performance are achieved as shown in the simulation results section.This explanation provides an insight into the operating principle of the proposed CP antenna.

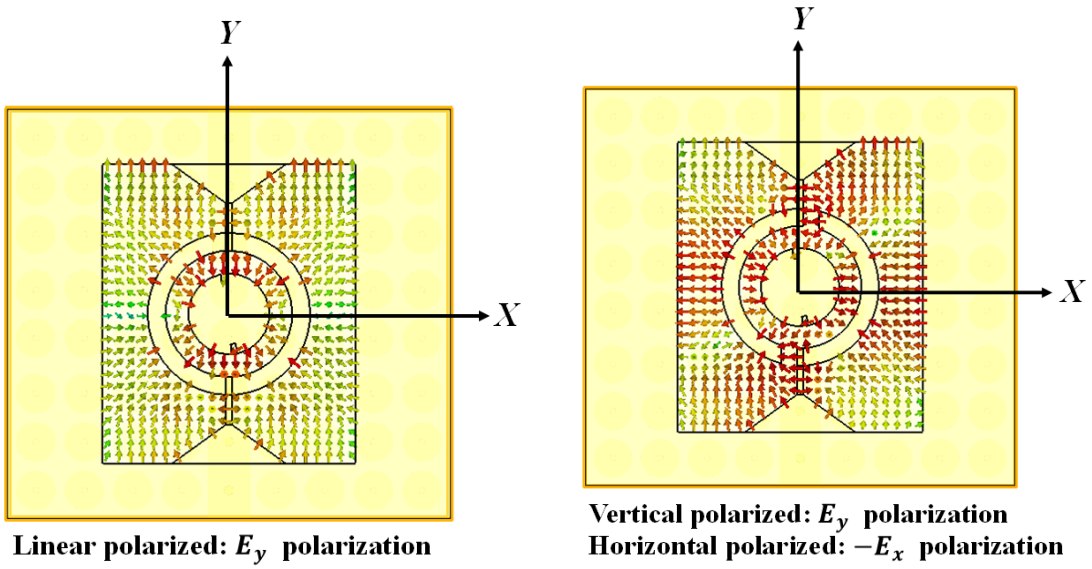

(a) (b)

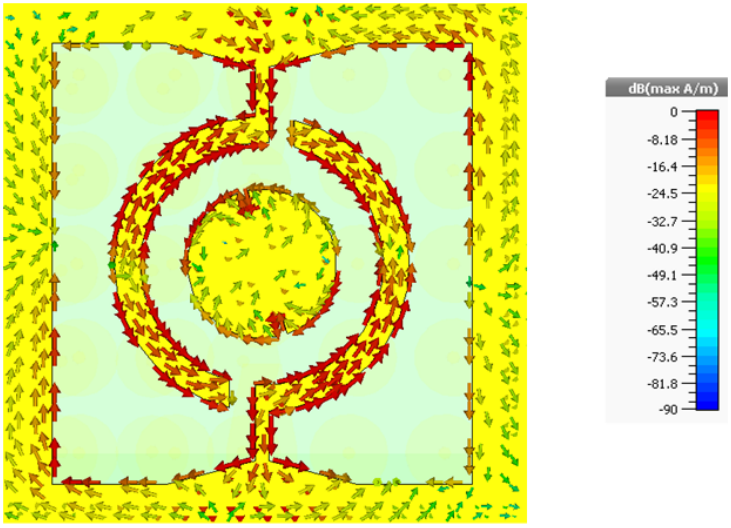

(c)

Figure 5.4: Surface E-field vector current distributions in the aperture of the proposed CP antenna at 30 GHz. (a) Closed ring. (b) Open ring. Red and green colors stand for the strongest and weakest magnitude, respectively. (c) Simulated current distributions at 30 GHz.

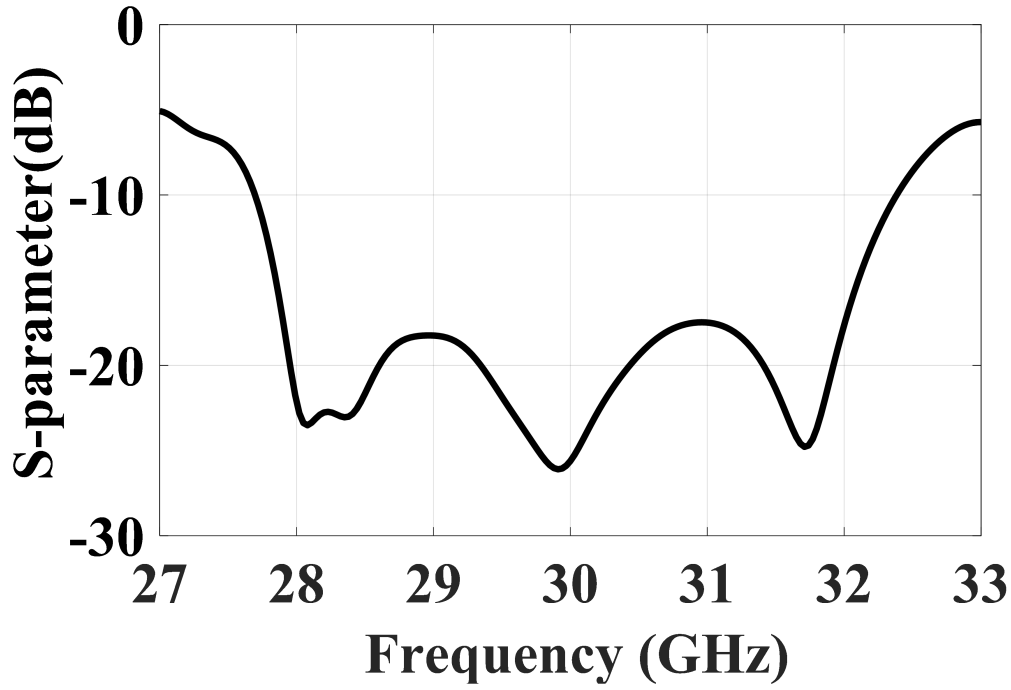

(a)

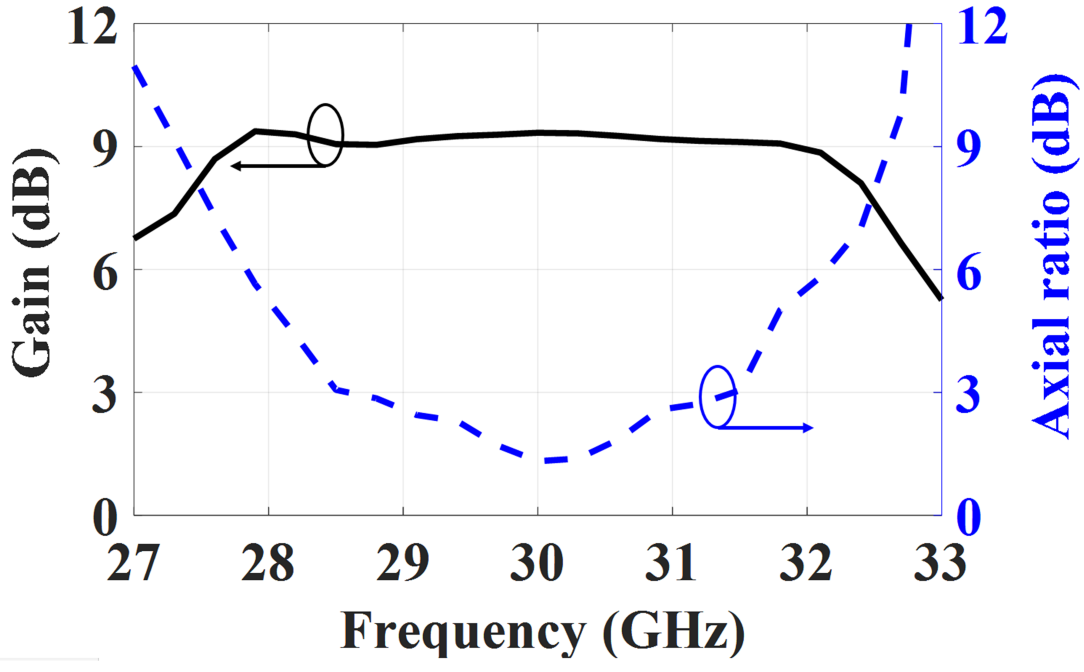

(b)

Figure 5.5: (a) Simulated S-parameters. (b) Simulated gain and axial ratio.

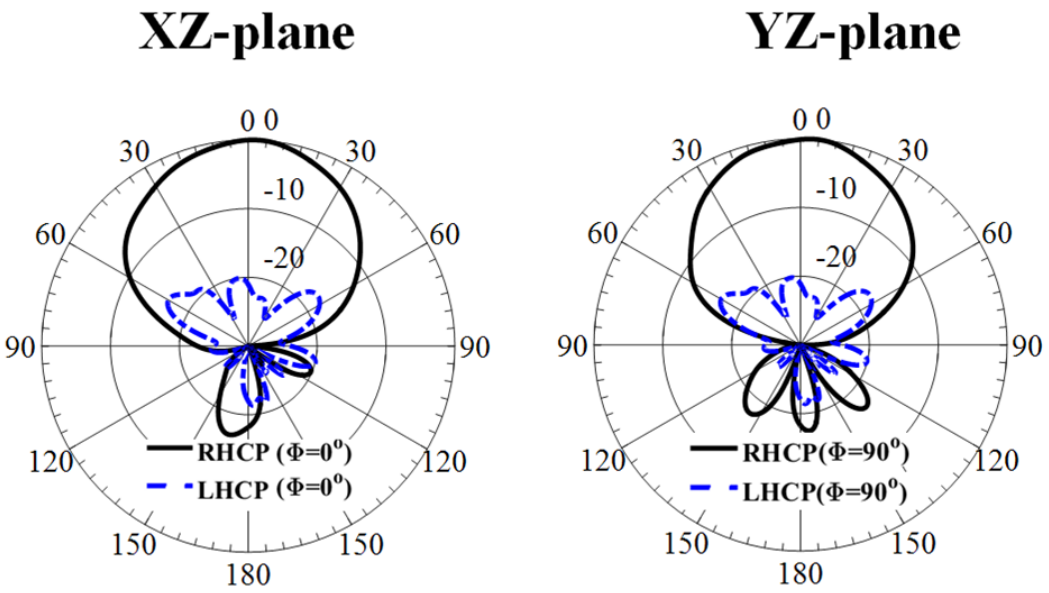

Figure 5.6: Simulated 2-D radiation pattern in XZ plane(left, $\phi = 0^o$) and YZ plane (right, $\phi = 90^o$) at 30 GHz.

5.1.2.2 Simulation Results

The simulated reflection coefficient of the proposed antenna with the differential feeding network is presented in Fig. 5.5(a). The proposed antenna has a wide impedance bandwidth of 15.6% at 30 GHz with -10 dB matching level. Fig. 5.5(b) exhibits the simulated gain results of the proposed antenna, which is around 9±0.5 dB with an axial ratio less than 3 dB over 10% of the operating frequency band. Simulated radiation pattern of the proposed antenna at 30 GHz is shown in Fig. 5.6. It is symmetrical in the XZ- and YZ-planes with low axial ratio corresponding to low cross-polarization level below -20 dB at broadside direction [158]. In addition, the antenna aperture efficiency η_{ap} is calculated using the following formula:

$$\eta_{ap} = \frac{G\lambda^2}{4\pi A_p} \tag{5.1}$$

where, G and A_p are the gain and the aperture size of the antenna, respectively. Using the gain of the proposed antenna with the differential feeding network and the area covered by the aperture as the physical aperture of the antenna, the obtained aperture efficiency is 89% at 30 GHz.

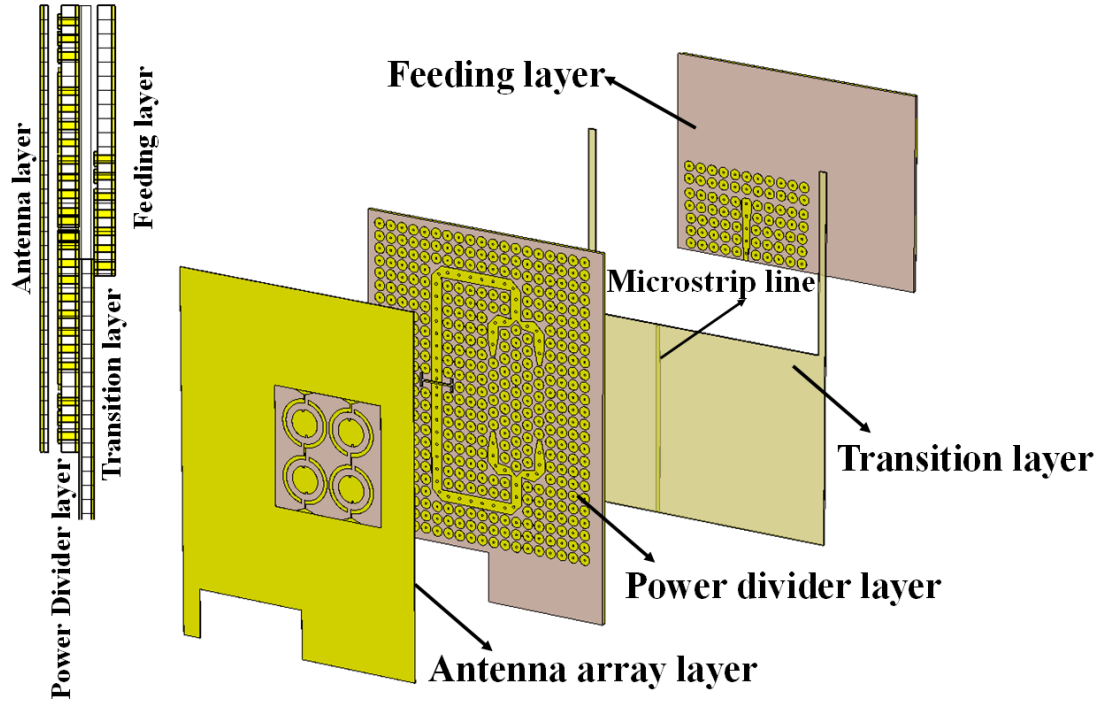

Figure 5.7: Geometry of the proposed CP differential feed antenna array.

5.1.3 Antenna Array Design

Based on the above single antenna element design, a high gain antenna array is realized by extending the aperture area to incorporate four radiation elements as shown in Fig. 5.7 and 5.8(a).The array consists of four CP antenna elements, each two are connected in a cascading manner through a metal strip. This strip with length c_x and width w_x controls the spacing and the mutual coupling between the elements, which is a critical parameter to adjust both impedance and axial ratio bandwidths. In addition, this strip length is varying within a limited range to keep the inter-element spacing less than λ and avoid grating lobes. Figs. 5.9(a), and 5.9(b) shows the effect of c_x on both impedance bandwidth and axial ratio, respectively. It can be depicted from these figures that the optimum value for c_x is 1.1 mm, and mainly affects both the impedance matching and axial ratio. The size of aperture area is about 1.6 $\lambda\times$ 1.65 λ, where λ is the free space wavelength at 30 GHz. The proposed array is differentially fed by 1×4 differential feeding power divider as shown in Fig. 5.8(b). The proposed antenna array is optimized using CST microwave studio to operate at 30 GHz, where detailed dimensions of the antenna

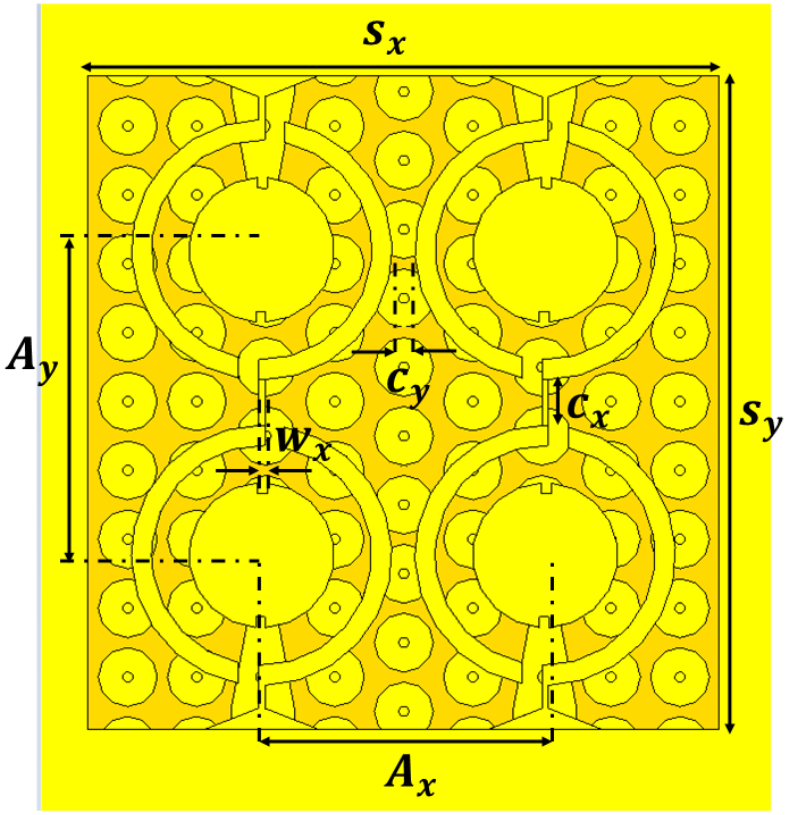

(a)

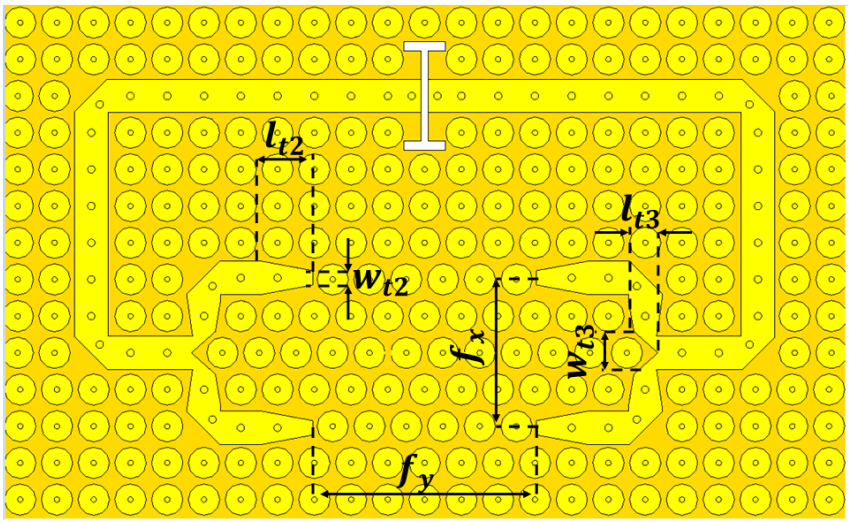

(b)

Figure 5.8: (a) Antenna array layer. (b) Power divider layer.

Table 5.3: Dimensions of differential feeding antenna array in millimeters

Parameters	l_{t2}	w_{t2}	l_{t3}	w_{t3}	f_x	f_y
Values	2.5	0.7	1.1	2	7	10.7
Parameters	s_x	s_y	A_x	A_y	c_x	c_y
Values	16	16.5	7	7.7	1.1	0.6

array configuration are given in Table 5.3. The simulated S-parameter, radiation pattern, gain, and efficiency will be compared with the measurement in the following section.

5.1.4 Experimental Validation

The proposed CP antenna array is fabricated using a standard PCB process, where the fabricated parts are shown in Fig. 5.10(a). These parts are aligned together using plastic screws at the edges of substrates, where the integrated prototype after assembly is shown in Fig. 5.10(b). The reflection coefficient ($\mid S_{11} \mid$) of the proposed array is measured by an N52271A PNA network analyzer, where the measured setup is shown in Fig. 5.11(a). The measured and simulated reflection coefficient of the proposed antenna array is shown in Fig. 5.11(b). Both measured and simulated matching level is less than -10 dB over a relative bandwidth of 15.6 % at 30 GHz.

The gain and radiation pattern measurements were performed in the anechoic chamber system, as shown in Fig. 5.12. Measured and simulated 2-D radiation patterns on XZ-plane and YZ-plane at 28.5, 30, and 31.5 GHz are presented in Figs. 5.13(a), 5.13(b), and 5.13(c), respectively. It can be observed that both measurement and simulation results are in good agreement. In addition, the measured radiation patterns are stable over the operating frequency band with the maximum gain pointed in the broadside direction. Furthermore, the maximum cross-polarization level (i.e.,LHCP) is less than 17 dB at the measured frequencies within the operating bandwidth.

Fig. 5.14(a) shows the measured and simulated RHCP gain and AR over the operating frequency bandwidth. The measured AR is below a 3 dB level over a 10 % bandwidth, which is matched very well with simulation results. In addition, the 3 dB gain bandwidth is 14 % with a maximum broadside gain of 13.5 dB at 30 GHz. The discrepancy in the measured gain is mainly due to the losses of the microstrip line transition, connector, adapters, and cable which have not been calibrated. Therefore, these losses mainly affect the calculated aperture efficiency, which results in a measured efficiency of 67.5 % at 30

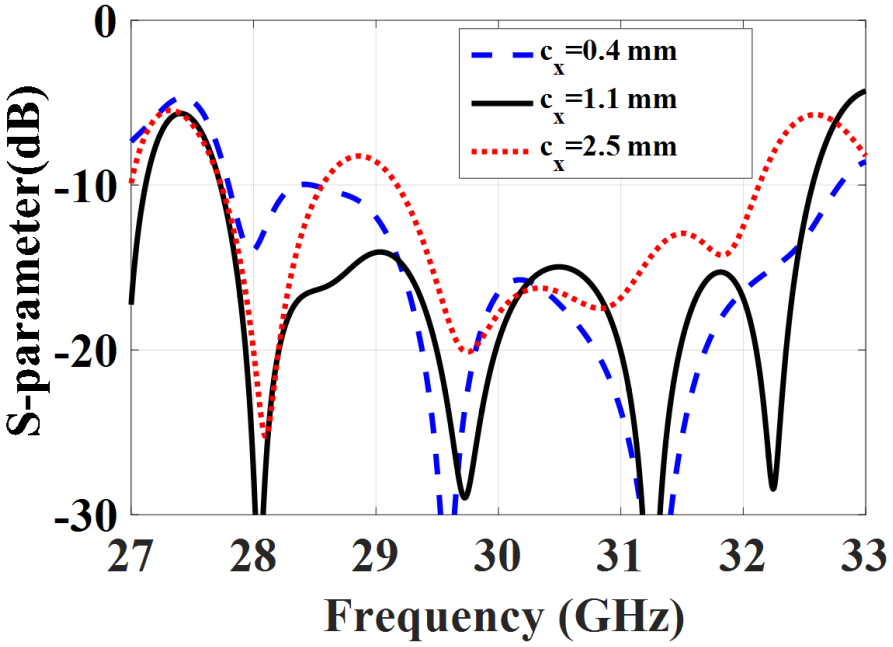

(a)

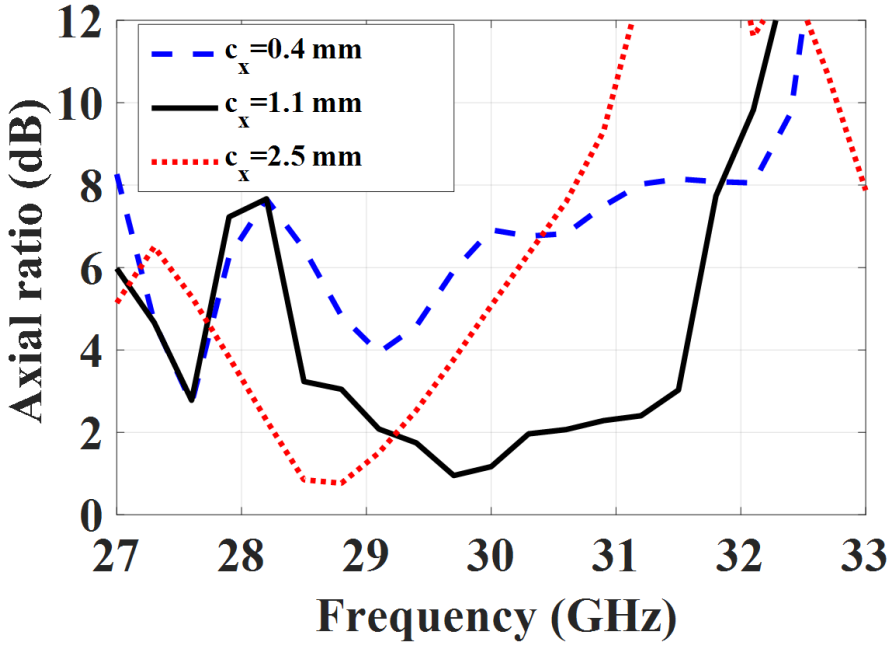

(b)

Figure 5.9: The effect of strip length c_x on (a) S-parameter and (a) Axial ratio

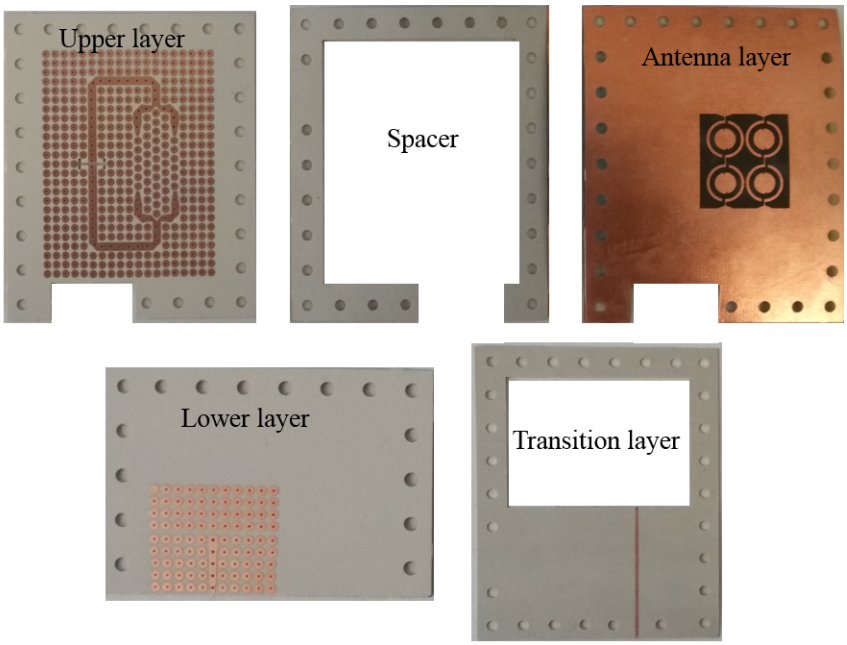

(a)

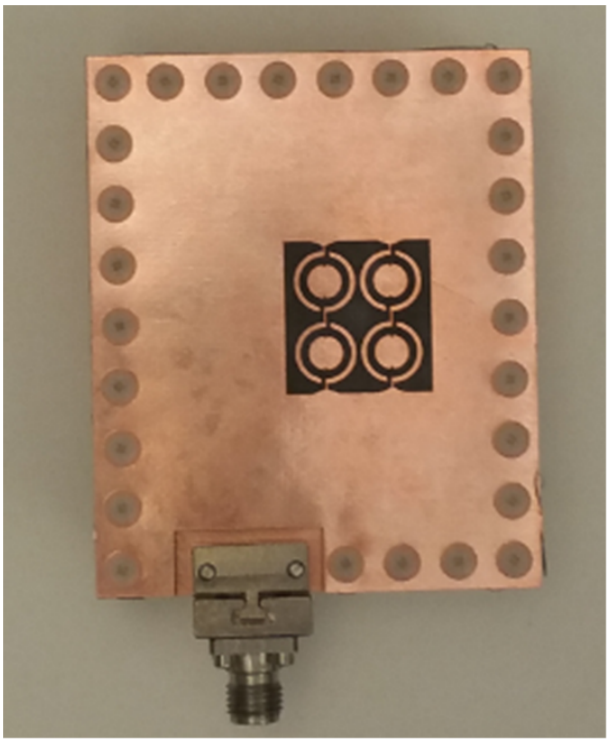

(b)

Figure 5.10: (a) Fabrication parts of the proposed antenna array before assembly. (b) Fabricated prototype of the proposed array after assembly.

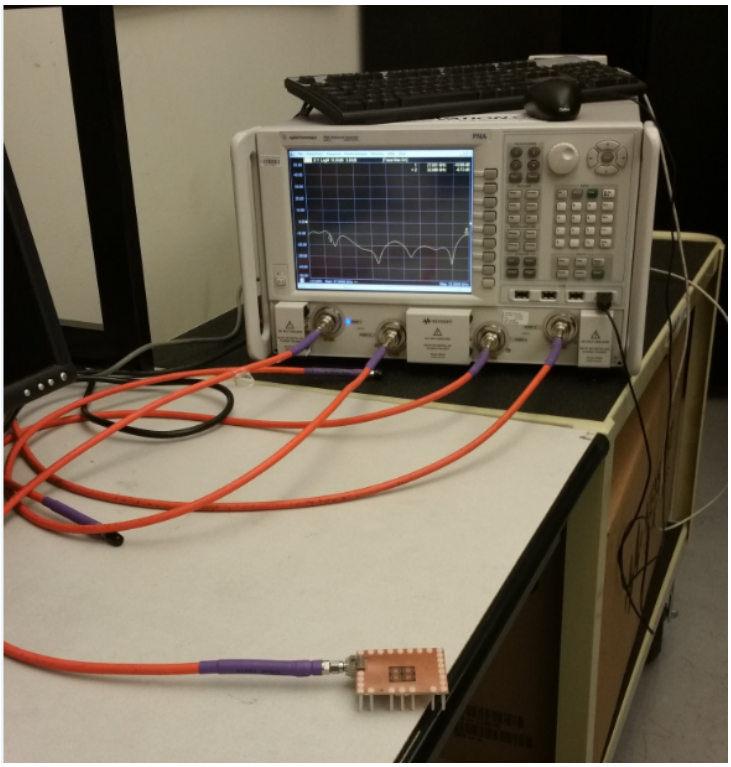

(a)

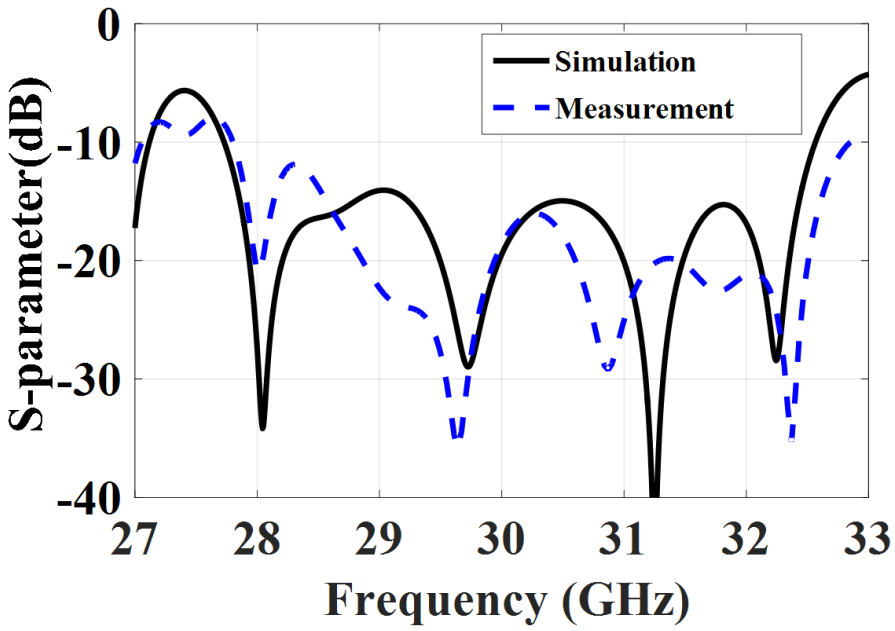

(b)

Figure 5.11: (a) Measurement setup. (b) Simulated and measured S-parameters.

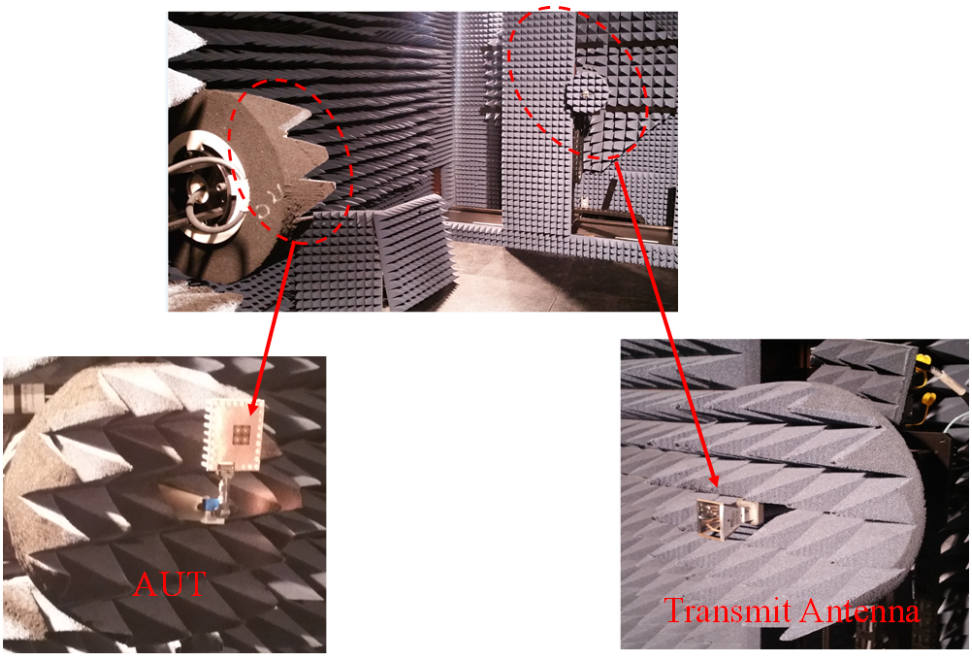

Figure 5.12: Radiation pattern measurement setup.

GHz. Due to a difficulty in the directivity measurement using the available facility, only the simulation radiation efficiency is shown in Fig. 5.14(b). It can be observed that the proposed antenna array achieve a radiation efficiency of 84 % with small variation over the frequency band of interest.

5.1.5 Performance Evaluation

A comparison between the proposed antenna array and other types of CP antenna array implemented with different guiding technologies is given in Table 5.4. For a fair comparison, the feeding network is included in the performance evaluation of the CP antenna array. This comparison assists in evaluating the potential of the proposed array structure. Compared with a 1×8 patch antenna array in [159], which is fed using rectangular waveguide, the proposed array has a wider bandwidth, lower profile, higher radiation efficiency, and low cost as well as similar gain. The 4×4 patch array in [160] and a 2×2 grid in [161], which implemented in LTCC and microstrip line technologies, respectively, having a wider impedance and AR bandwidths than the proposed array. However, the proposed antenna array achieves high efficiency with a smaller size and low profile. Compared with the 2×2 patch array backed by SIW cavity in [156] and 2×2 ring slot on SIW cavity in [157], the proposed array has wider impedance and AR bandwidths as well as higher gain. The

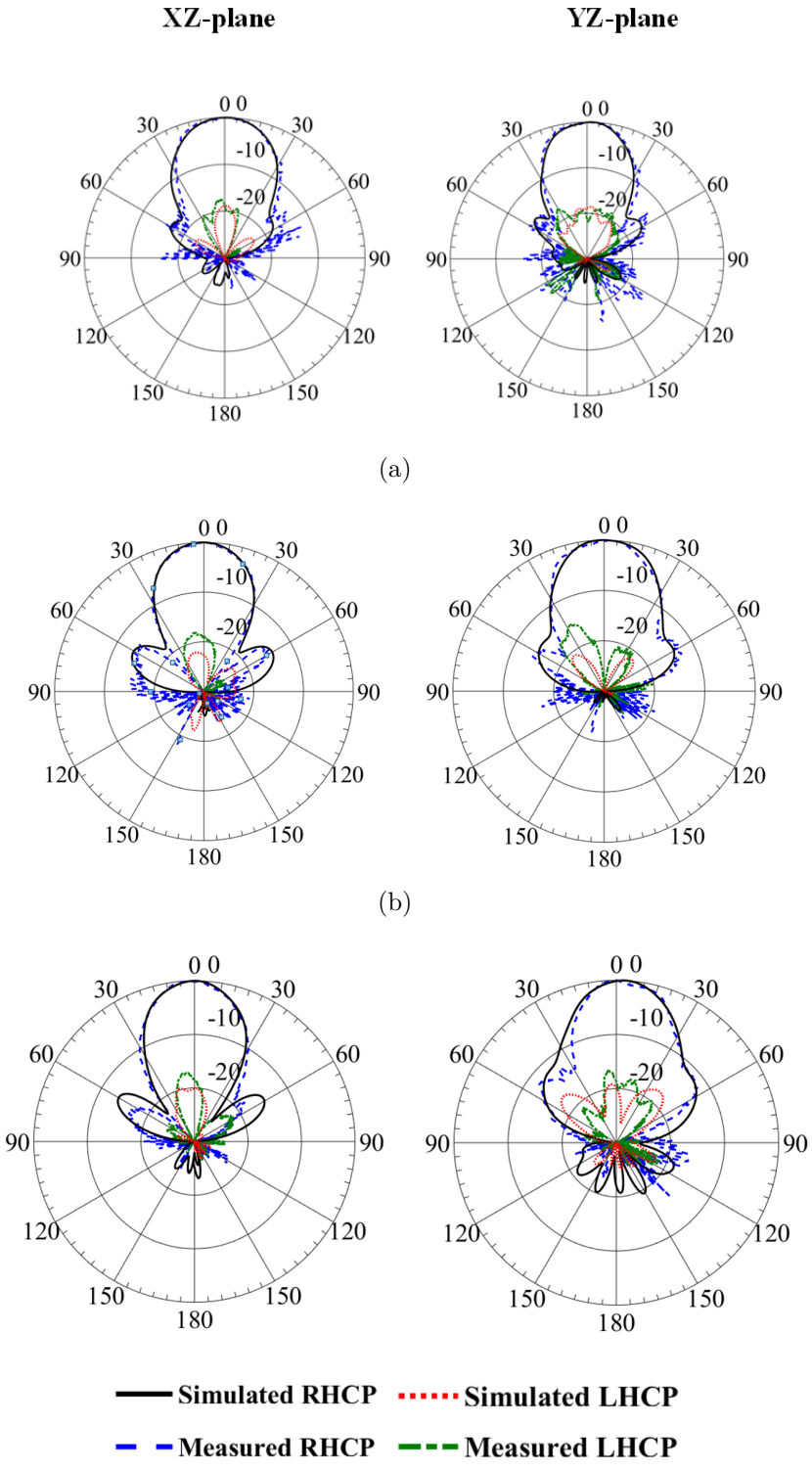

Figure 5.13: Measured and simulated 2-D radiation pattern: (a) F=28.5 GHz. (b) F=30 GHz. (c) F=31.5 GHz

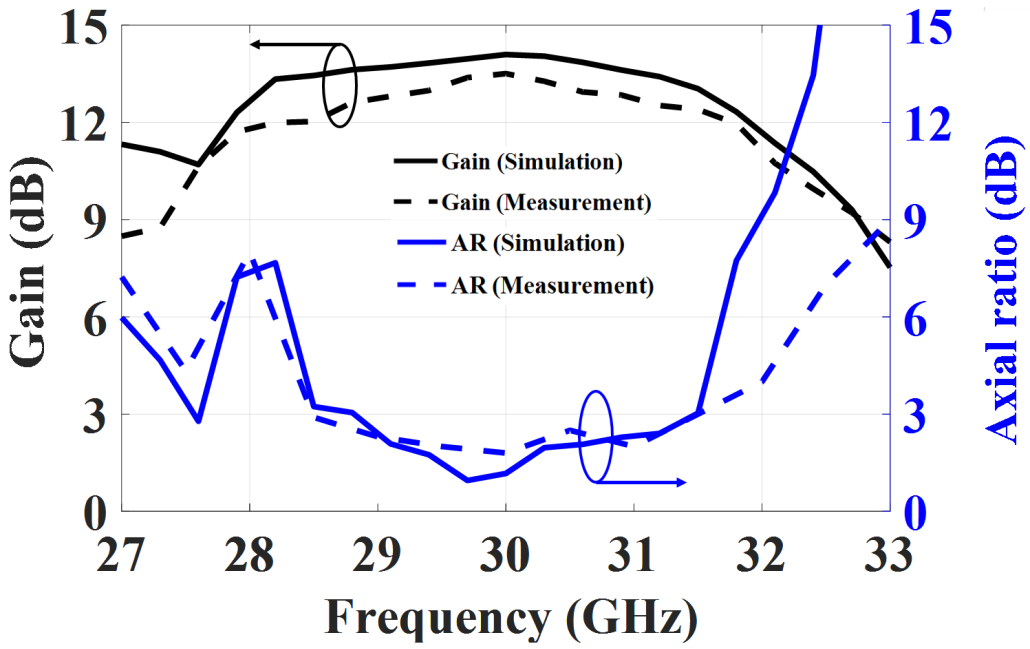

(a)

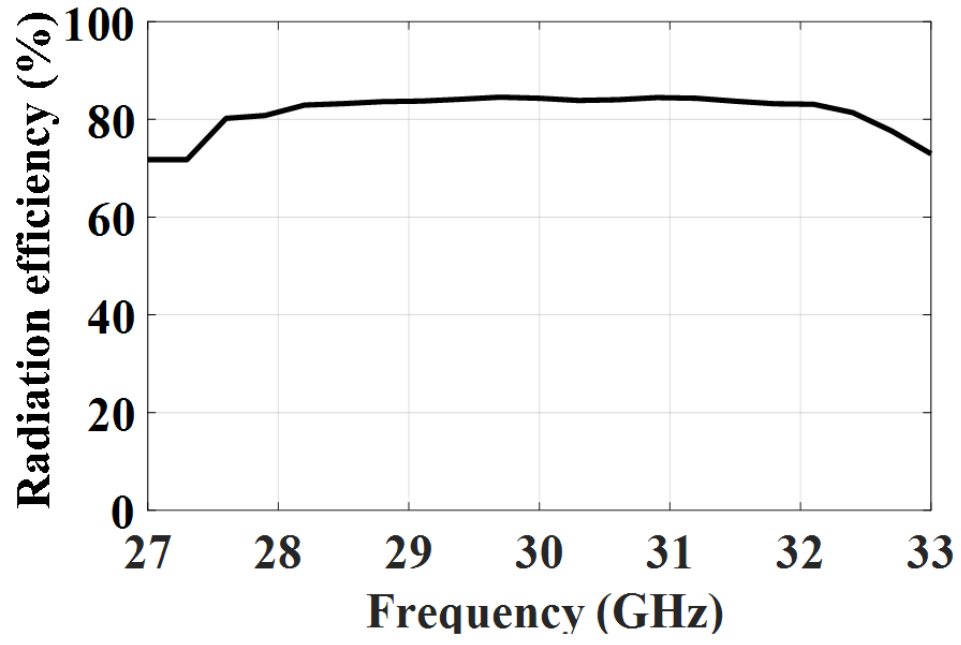

(b)

Figure 5.14: (a) Simulated and measured gain and axial ratio. (b) Simulated radiation efficiency.

Table 5.4: Comparison between different CP antenna arrays operating at mmWave band

Ref.	Freq. (GHz)	Impedance BW	Gain	3-dB Gain BW	3-dB AR BW	Radiation eff.
[159]	26	5.7 %	14 dB	5.7%	5.7%	70%
[160]	28.35	19.6 %	17.4 dB	13%	14%	65%
[161]	60	16.4%	14.3 dB	11.9%	14.4%	31.8%
[156]	60	6.6 %	12.5 dB	6.6%	6.6%	82%
[157]	18	3.1 %	7.1 dB	N.A	3.6%	N.A
[162]	30	6%	14.5 dB	6%	6%	N.A
[163]	77	11.6 %	12.8 dB	9%	9%	N.A
The proposed work	30	15.6 %	13.5 dB	14%	10%	84%

4×4 loop array fed by SIW feeding network in [162]has a high gain compared with the proposed array. However, the proposed array has a wider impedance and AR bandwidths with higher radiation efficiency. Compared with the 1×4 slots fed by metal RGW in [163], our antenna array has a lower profile, wider impedance and AR bandwidths, and higher gain.

5.2 Dual Polarized Antenna Array

5.2.1 Dual-polarized ME-dipole Antenna Design

The geometry of the proposed dual-polarized ME-dipole antenna is depicted in Fig. 5.15, which consists of three Rogers RT6002 substrates with dielectric constant $\varepsilon_r = 2.94$ and thickness h_s= 0.762 mm. The dual-polarized ME-dipole structure is built in the top layer, where vertical and horizontal electrical planar dipoles composed of four identical square metallic patches are printed on the top substrate surface as shown in Fig. 5.16(a). Each patch is connected to the substrate ground through a set of six metallic plated via holes located close to the inner corner of the patch. While the vertical and horizontal magnetic dipoles are formed by a cross-shaped aperture between the patches extended to the top substrate ground surrounded by the platted via holes as shown in Fig. 5.16(a). This cross-shaped aperture is composed of two vertical and horizontal rectangular apertures, which each aperture is used to excite vertical and horizontal electrical and magnetic dipoles, respectively. A square AMC sidewalls cavity is adopted to excite the proposed dual-polarized ME-dipole, which is located in the middle substrate. The AMC walls are formed by EBG mushroom-shaped structure as shown in Fig. 5.16(b). This cavity is excited by two PRGW lines located in the bottom and middle substrates with input ports 1 and 2, respectively. To increase the gain of the proposed dual-polarized ME-dipole antenna to be suitable for mmWave applications, an AMC surface formed by Electromagnetic Band Gap (EBG) mushroom-shaped structure is placed around the ME-dipole as shown in Fig. 5.16(a).

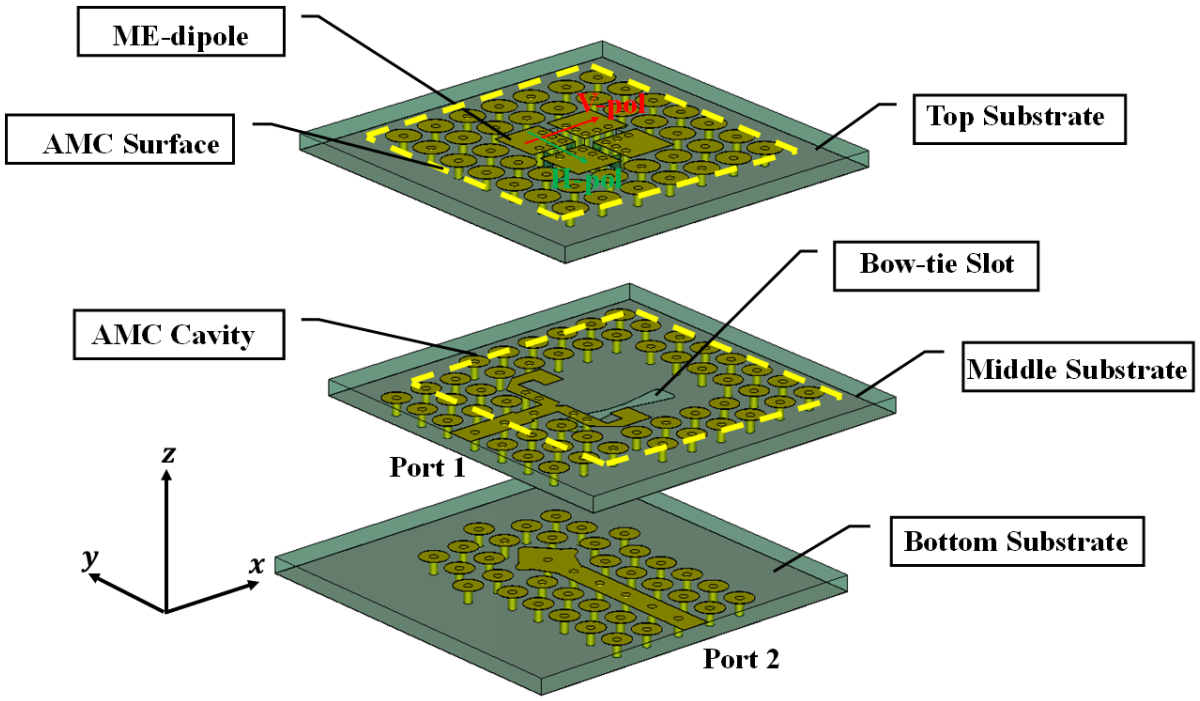

Figure 5.15: Geometry of the proposed dual-polarized ME-dipole antenna.

5.2.2 Design Guideline and Operating Principle

In order to achieve stable radiation characteristics over a wide operating frequency band, ME-dipole antenna is adopted in the proposed work. The idea of ME-dipole antenna is to use the concept of the complementary antenna to achieve symmetrical E-plane and H-plane patterns [164]. As well known, the electric dipole has a radiation pattern of a figure-8 and a figure-O in the E-plane and H-plane, respectively, while reverse radiation patterns are achieved for the magnetic dipole. If both electric and magnetic dipoles are placed orthogonally and excited simultaneously with appropriate amplitude and phase, symmetrical unidirectional radiation patterns with low back radiation can be obtained [165]. Therefore, this type of antenna has a higher gain and efficiency than other available antenna elements [166]. Also, it has a stable gain and beamwidth over a wide frequency band. Generally, the electric dipole is implemented by a horizontal metallic patch, while the magnetic dipole is realized using a slot antenna.

Practical designs feature a dual-polarization are reported in the literature, [139, 167, 168]. In order to excite these ME- dipole antenna types, pair of L-shaped are deployed with different heights to achieve high isolation. Although these designs have a good impedance bandwidth as well as high isolation, they are featured with a large size and bulky struc-

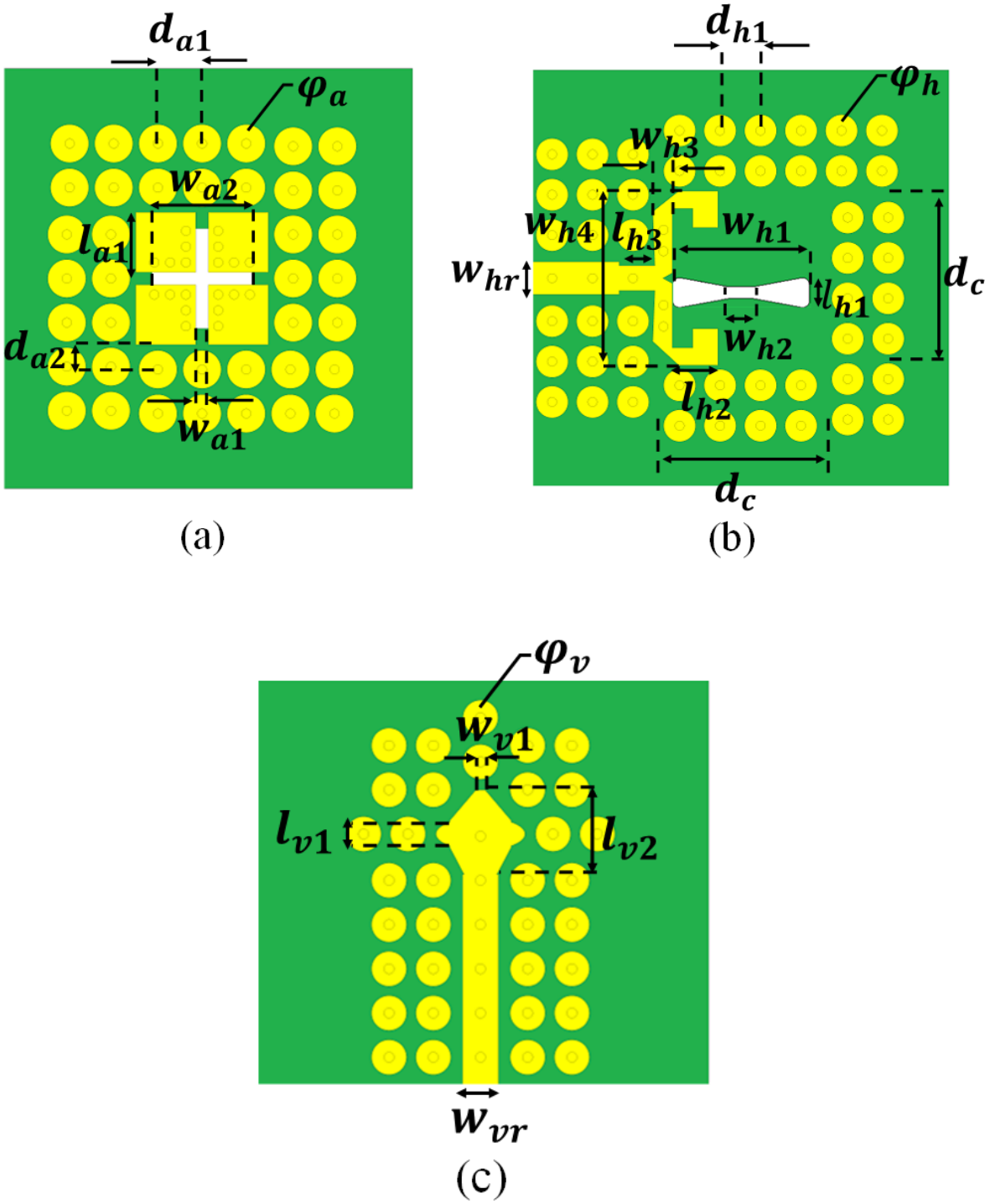

Figure 5.16: Top views of the dual-polarized ME-dipole antenna layers. (a) Top substrate. (b) Middle substrate. (c) Bottom substrate.

tures, which limit their functions, especially at mmWave frequencies. Therefore, a low profile ME-dipole antenna realized using a printed circuit board (PCB) technique is proposed in this work. The electric dipoles are realized using a pair of patches printed on the top substrate surface as shown in Fig. 5.16(a), while the apertures between the metallic patches represent the magnetic dipoles.

5.2.2.1 Design Guideline

As mention before, a square AMC sidewalls cavity is deployed to excite the proposed antenna. A square cavity is chosen to have similar exciting modes characteristics for both polarization. The initial size of the cavity is calculated to excite a TM_{210} and TM_{120} for the horizontal and vertical polarization, respectively at a lower frequency of the operating bandwidth (27 GHz), where the dimension of the cavity $d_c = 7.9$ mm is calculated as follow [169]:

$$d_c = \frac{\sqrt{5}c}{2\sqrt{\epsilon_{reff}} f_{r(TM_{210,120})}} \tag{5.2}$$

where, c is the speed of the light in free space, ϵ_{reff} is the effective dielectric constant, and f_r is the resonance frequency for TM_{210} or TM_{120}. The square cavity is partially dielectric filled with overall height $h_t = h_s + h_g$, where $h_s = 0.762mm$ is the thickness of dielectric, while $h_g = 0.254mm$ is the height of air gap. Hence, the effective dielectric constant ϵ_{reff} is calculate as follow:

$$\epsilon_{reff} = \frac{h_s}{h_t}\varepsilon_r + (1 - \frac{h_s}{h_t}) \tag{5.3}$$

An orthogonal feeding technique is used to excite the cavity, which implemented by two PRGW structures located at different layers to achieve sufficient isolation between the horizontal and vertical polarization. The horizontal polarization (H-Pol) is fed by a PRGW line printed on the middle substrate with input port 1. The input power from port 1 is coupled to the cavity through symmetrical end-launch PRGW configuration as shown in Fig. 5.16(b). The magnetic field distribution for a TM_{210} mode when feeding on port 1 is shown in Fig. 5.17(a). This mode enables the excitation of the horizontal

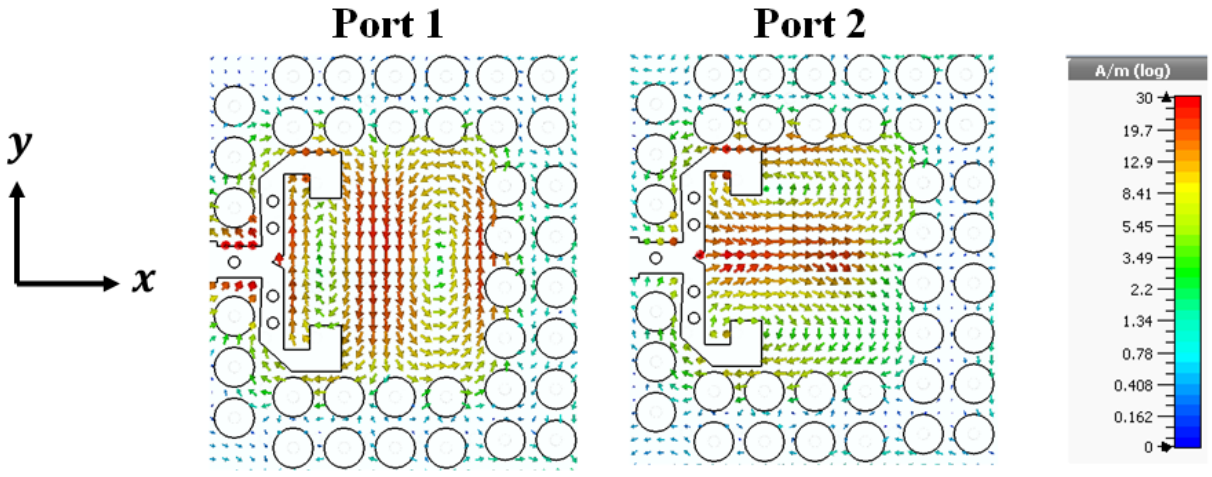

(a)

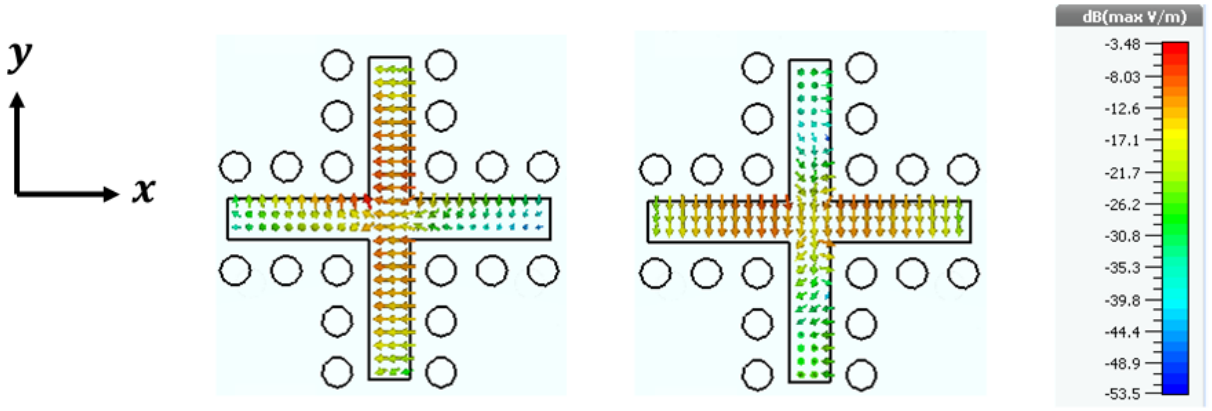

(b)

Figure 5.17: The excitation of the proposed dual-polarized antenna . (a) The magnetic field distribution in the square cavity. (b) The electric field distribution in the excited slots.

aperture without affecting the vertical aperture as shown in Fig. 5.17(b), which in turn the horizontal ME-dipole is excited. A capacitive and inductive matching circuit formed by a metallic U-shape strip and pair of metallic vias are deployed to appropriate couple the input power to the cavity with minimum reflection. Several parametric studies are performed to figure out the proper dimensions of the U-shape strip as well as the location of the inductive vias.

The vertical polarization (V-Pol) is obtained by a PRGW line printed on the bottom substrate with input port 2. The input signal from port 2 is coupled through a Bow-tie slot etched on the bottom ground of the middle substrate as shown in Fig. 5.16(c) . The magnetic field distribution for the TM_{120} mode when feeding on port 2 is shown in Fig. 5.17(a). This mode enables the excitation of the vertical aperture as shown in Fig. 5.17(b), consecutively the vertical ME-dipole is excited through the vertical aperture. To achieve a good impedance matching over a wide frequency bandwidth, a matching stub is connected to the PRGW line located on the bottom substrate as shown in Fig. 5.16(c). Based on detailed parametric studies on the dimensions of the matching stub, Bow-tie slot, and the distance between the Bow-tie slot and the matching stub; the dimensions are determined. Finally, an optimization process is performed for the whole structure with around 10% of the initial dimensions to achieve a deep matching level and high isolation between the exciting ports.

Several articles are addressed the design of the PRGW line, which it's operating bandwidth is controlled by the bandgap of the surround EBG mushroom-shaped structure [38, 39, 149]. The air gap for the proposed PRGW line is selected to be h_{gap}=0.254 mm, where the dispersion diagram for a section of the designed PRGW is shown in Fig. 5.18. This diagram is obtained using Computer Simulation Technology (CST) Eigenmode solver, which shows the bandgap starts from 24 GHz to 40 GHz, where the quasi-TEM mode is propagating. Also, the widths of the ridges for both PRGW lines w_{hr} and w_{vr} are selected to achieve a 50Ω characteristics impedance. Detailed dimensions of the proposed dual-polarized ME-dipole antenna are indicated in Table. 5.5.

5.2.2.2 Operating Principle

For further understanding of the operating principle of the proposed antenna, the current distribution on the metallic patches as well as the electric field on the radiation apertures

Table 5.5: Dimensions of the proposed dual-polarized ME-dipole antenna

Parameters	ϕ_a	d_{a1}	d_{a2}	w_{a1}	w_{a2}	l_{a1}	ϕ_h
Values	1.6	1.8	1	0.5	4.1	2.5	1.3
Parameters	d_{h1}	w_{hr}	w_{h1}	w_{h2}	w_{h3}	w_{h4}	l_{h1}
Values	1.7	1.37	5.6	1	0.75	7.3	0.6
Parameters	l_{h2}	l_{h3}	ϕ_v	w_{v1}	w_{vr}	l_{v1}	l_{v2}
Values	1.6	1.5	1.3	0.4	1.37	0.9	3.2

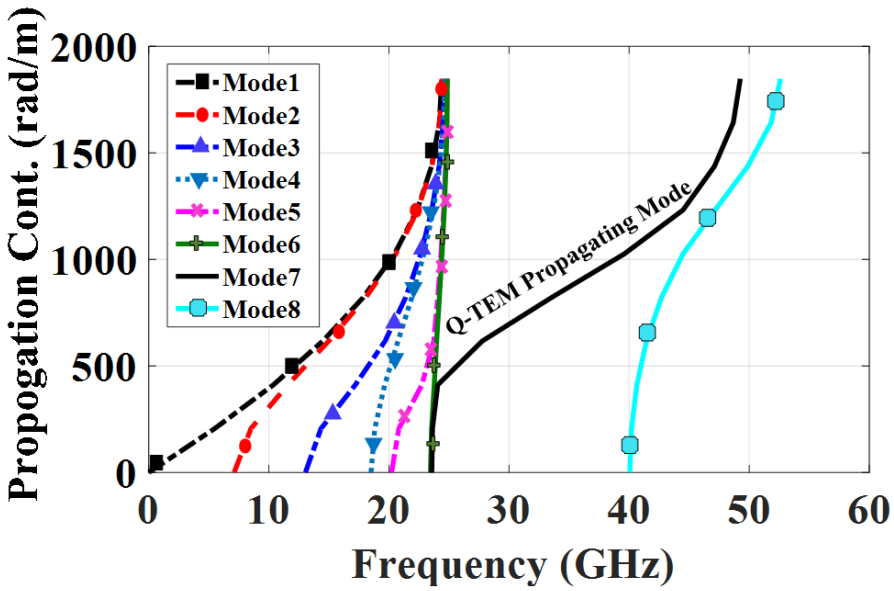

Figure 5.18: The dispersion diagram of PRGW structure.

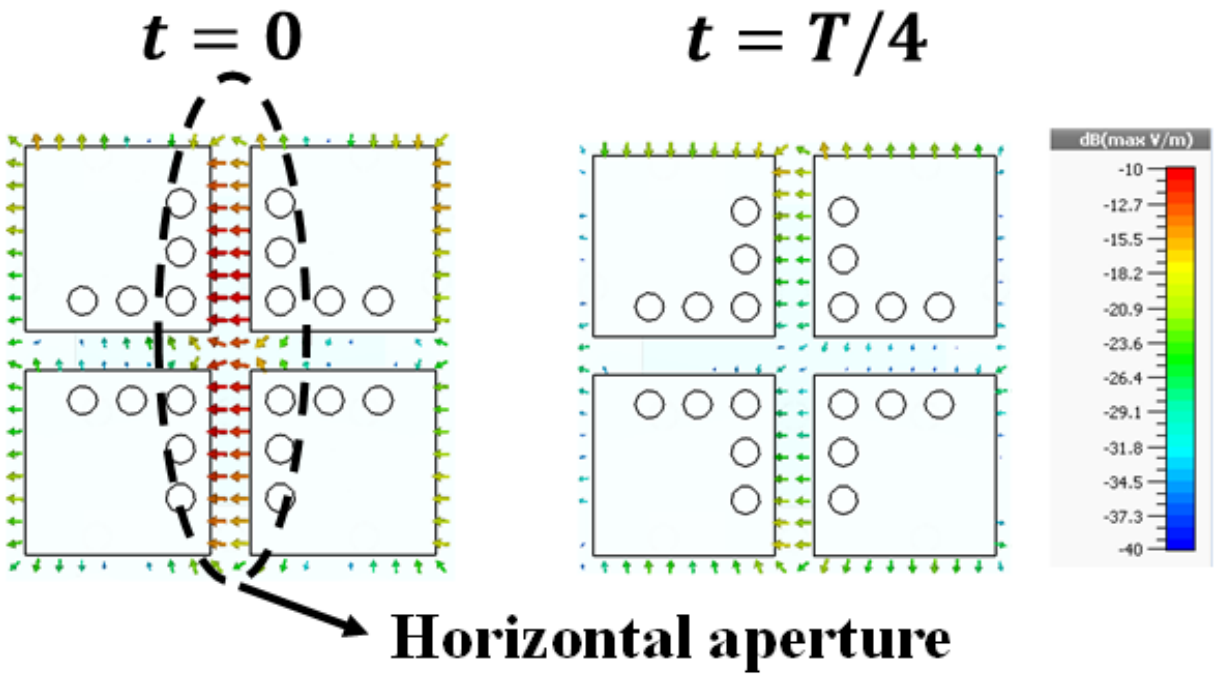

(a)

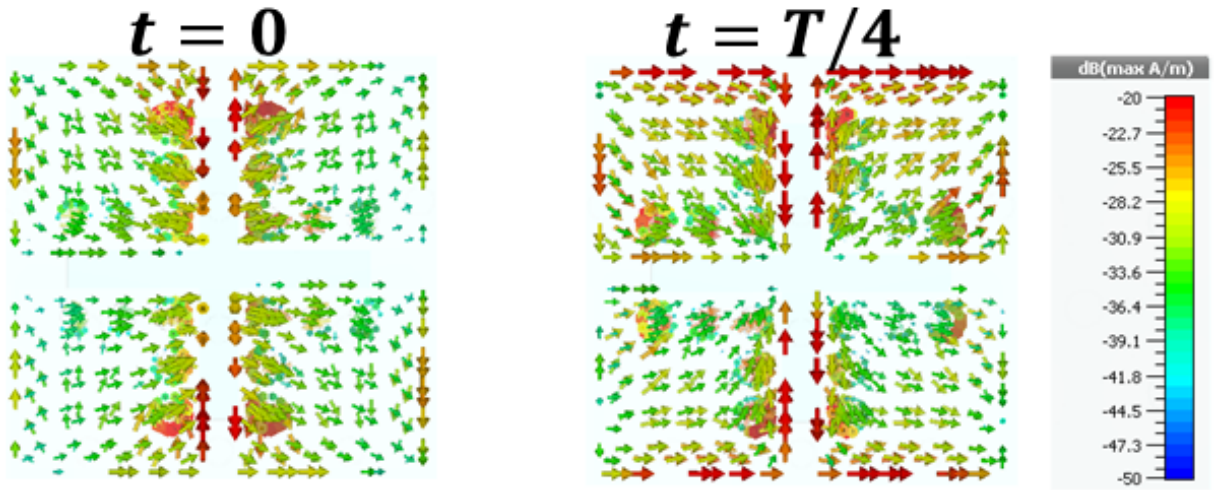

(b)

Figure 5.19: The proposed dual-polarized ME-dipole operation when port 1 is excited. (a) Electric field distribution. (b) Current distributions.

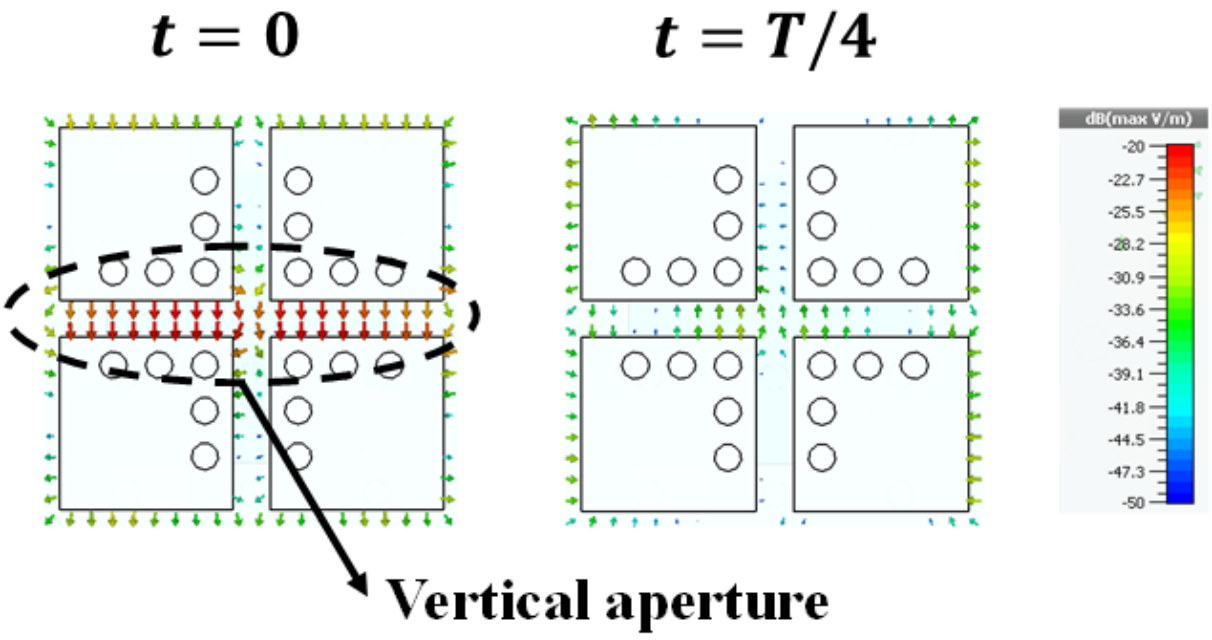

(a)

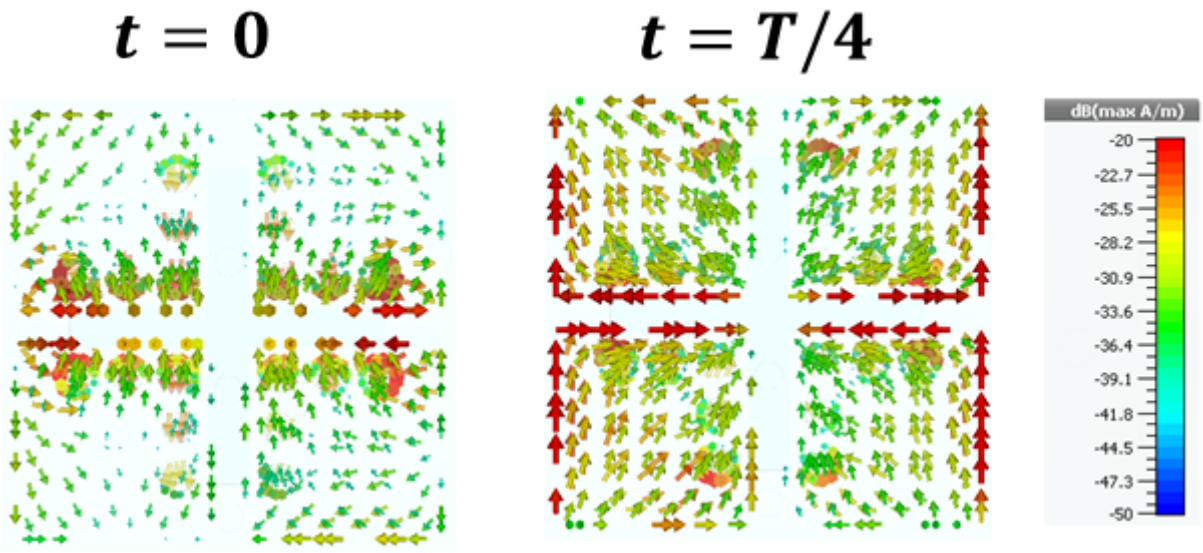

(b)

Figure 5.20: The proposed dual-polarized ME-dipole operation when port 2 is excited. (a) Electric field distribution. (b) Current distributions.

is shown in Figs. 5.19 and 5.20 for port 1 and Port 2, respectively, where T is a period of time at the center operating frequency (30 GHz). At the time $t = 0$ and port 1 is excited, the electric field density on the horizontal radiating aperture is dominated and the current density on the metallic patches is minimized, which means that magnetic dipole is strongly excited. While, at $t = T/4$ the electric field density is relatively weak and the current density reached the maximum on the outer edges of the patches, which means that the electric dipole is strongly excited. Similar operation can be depicted when port 2 is excited as shown in Fig. 5.20, where the orientation of both electric and magnetic dipoles are perpendicular to the case when port 1 is excited. Consequently, both electric and magnetic dipoles are excited with roughly similar strength, 90^o phase difference and orthogonal to each other, which indicates that the proposed antenna is operating as a complementary antenna [164, 165].

5.2.3 Gain Enhancement of the Proposed Antenna

A gain enhancement for the proposed antenna is obtained by placing an AMC surface around the ME-dipole antenna as shown in Fig. 5.15. Different approaches for the realization of the AMC are introduced in the literature, where the deploying of a mushroom shape can be considered the most effective and simple technique that features a wide operating bandwidth. In the proposed design, the mushroom shape EBG unit cell is designed to achieve a reflection coefficient with a magnitude of 0 dB over the operating bandwidth and a phase crosses 0^o at the center operating frequency. The reflection magnitude and phase for the designed EBG unit cell are shown in Fig. 5.21, where the operating bandwidth of the AMC surface is defined as the range where the reflection phase is between $+90^o$ and -90^o [170–172]. The performance of the proposed antenna is evaluated with and without the AMC surface, where a gain improvement of 2.5 dBi is achieved as shown in Fig. 5.22. This gain enhancement is due to the suppression of surface waves excited in the dielectric substrate that results in a great improvement for the sidelobe levels and front to back ratios. Fig. 5.23 shows the effect of the AMC surface on the front to back ratio. It is clear that the front to back ratios of the antenna are dramatically improved, where the front to back ratios larger than 20 dB are achieved over the whole operating bandwidth.

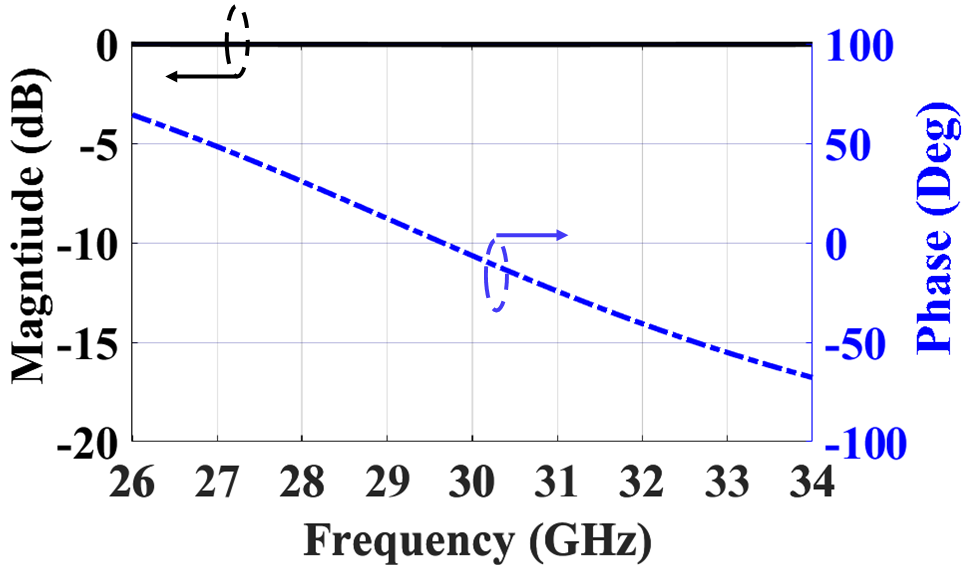

Figure 5.21: Simulated reflection coefficient magnitude and phase of the AMC surface.

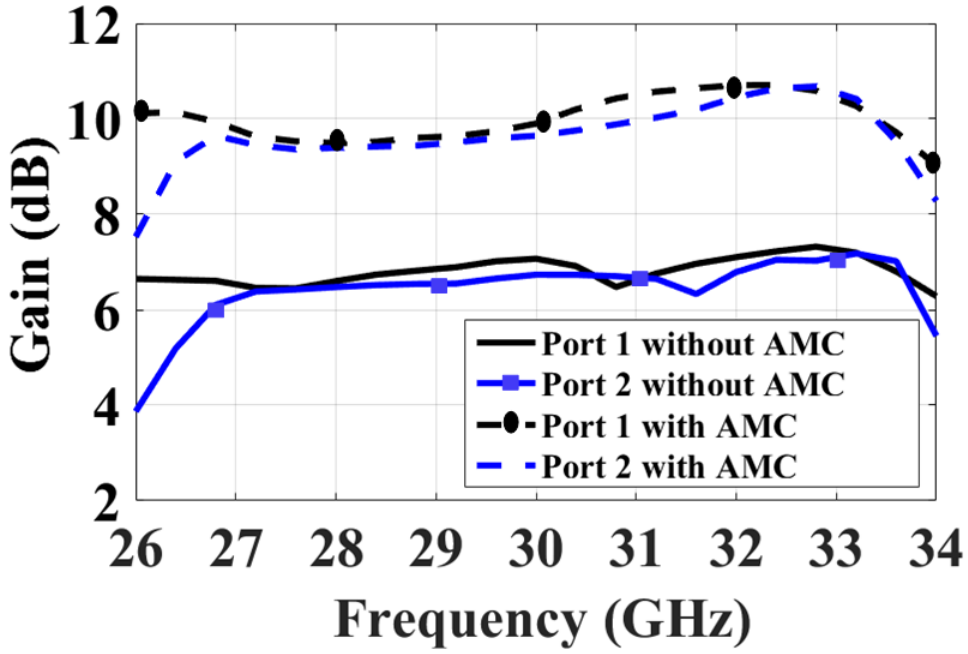

Figure 5.22: Simulated gain of the proposed antenna with and without the AMC surface.

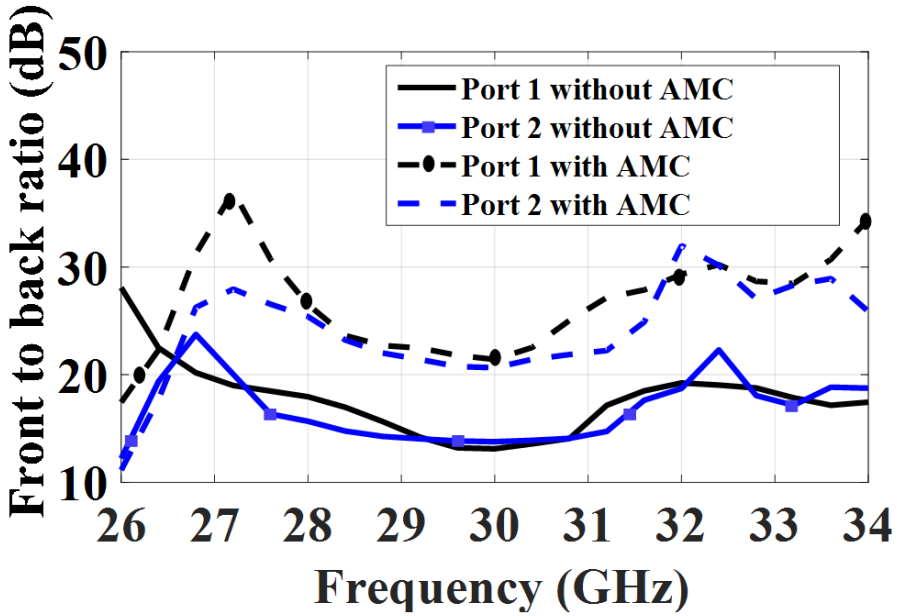

Figure 5.23: Simulated front to back ratio of the proposed antenna with and without the AMC surface.

5.2.4 Experimental Validation

The proposed antenna is fabricated using the conventional PCB process, where the fabricated prototype is shown in Fig. 5.24(a). A microstrip line to the PRGW transition is designed to achieve a -15 dB matching level that allows the testing of the proposed antenna. Detailed design of such type of transition is addressed before in the literature [38–40, 42, 149]. The fabricated parts of the proposed antenna are aligned together using glue, where the substrate layers are stacked together using the thermal pressure technique. The reflection coefficient of the proposed antenna is measured by the N52271A performance network analyzer (PNA), where the measured setup is shown in Fig. 5.24(b). The measured and simulated reflection coefficients of the proposed dual-polarized antenna are shown in Fig. 5.25(a). Both measured and simulated matching levels are less than -10 dB with an overlapped relative bandwidth of 23.4% at 30 GHz. Also, the isolation level higher than 20 dB is achieved over the whole band. it's worth to mention that relatively low isolation mainly occurs because of the asymmetry of the cavity mode caused by the feeding part of port 1 as can be seen from the H-fields in Fig. 5.17(a). This asymmetry of the H-fields of the mode when port 1 is excited results in a non-zero filed in the bowtie slot and hence reduces the isolation. A technique to improve the isolation is by using different slot shape with smaller size. Another technique is to avoid using the AMC cavity and used

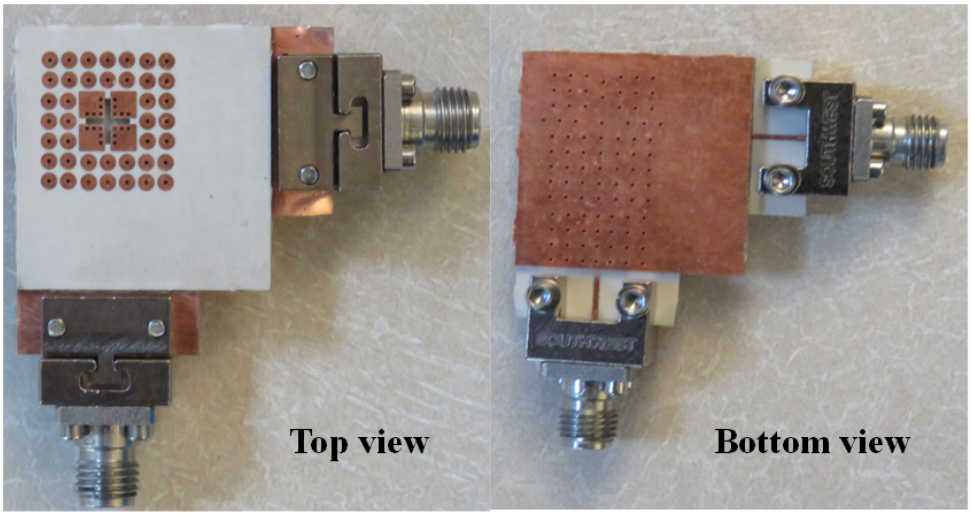

(a)

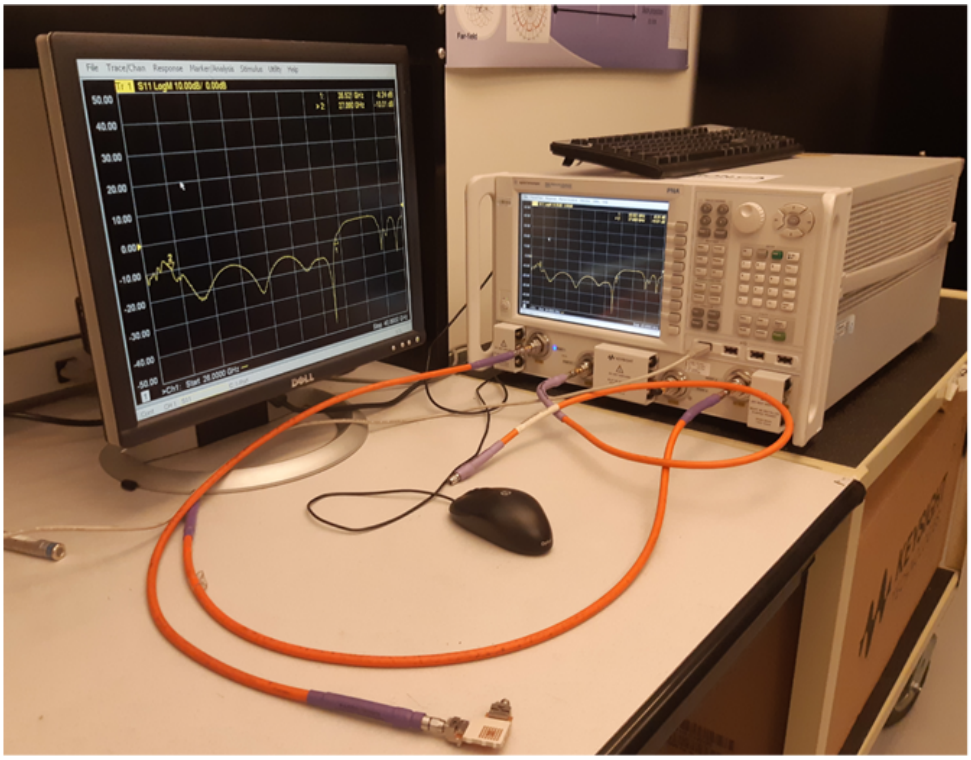

(b)

Figure 5.24: (a) The fabricated prototype of the proposed dual-polarized antenna. (b)The measurement setup.

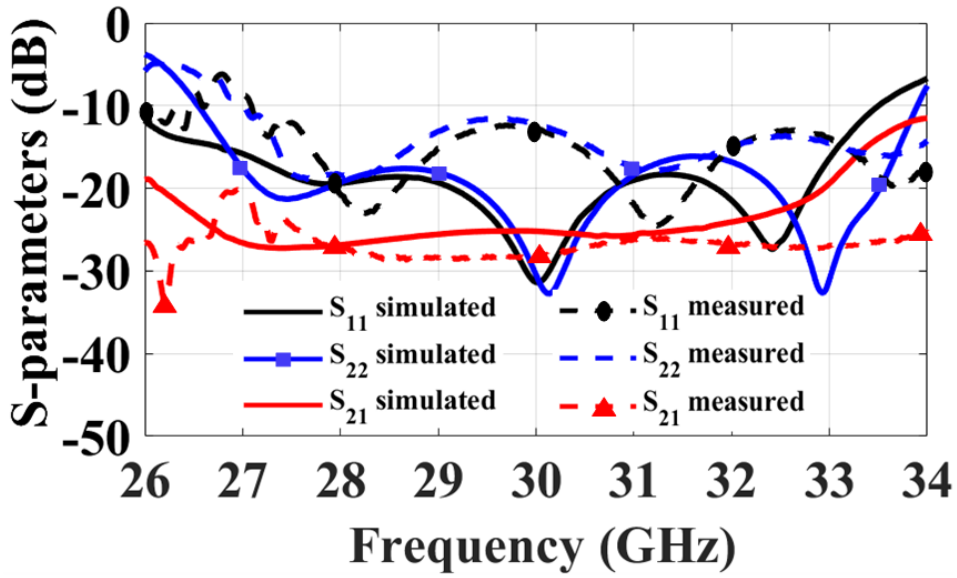

(a)

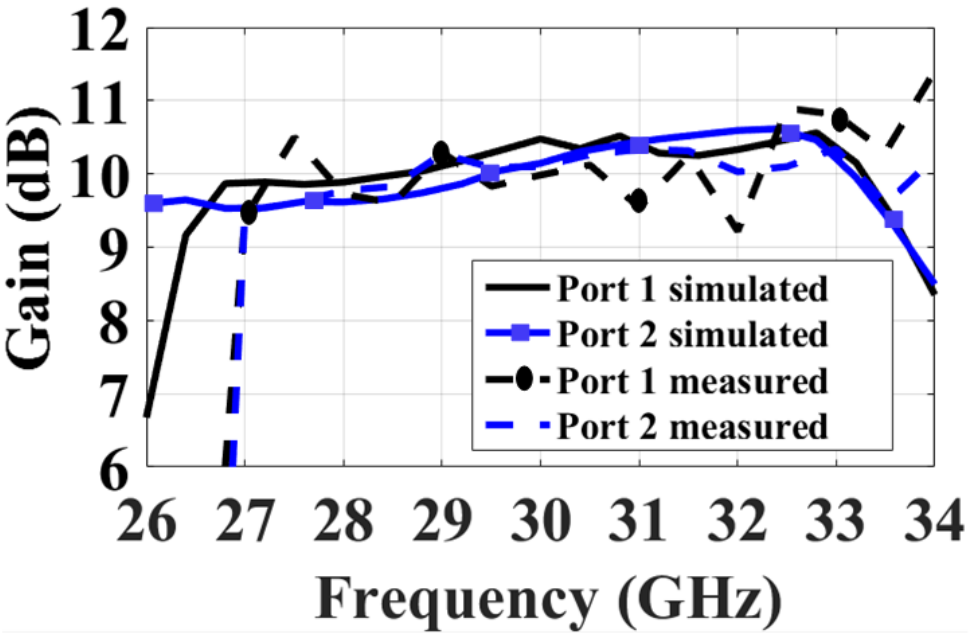

(b)

Figure 5.25: The simulated and measured results of the proposed dual-polarized antenna . (a) S-parameters. (b) Gain.

a direct coupling between the two ports and the antenna through using different matching techniques. This will increase the isolation, however, narrow bandwidth and large size will be obtained. A slight frequency shift can be observed for the measured results, which probably due to the fabrication tolerance or the change in material properties at high frequencies.

The gain of the proposed antenna is measured and compared with the simulation

Table 5.6: Comparison between dual-polarized antenna configurations

Ref.	Frequency (GHz)	BW/ ISO.	Gain	SLL/X-Pol. level	Size $\lambda \times \lambda \times \lambda$
[137]	92.5	24 %/17 dB	7.25 dBi	-10 dB/-25 dB	N.A
[138]	60	16.7 %/ 30 dB	11.2 dBi	-11.2 dB/-32 dB	1.33 × 1.33× 0.47
[139]	60	15 %/ 55 dB	N.A	-13 dB/N.A	1.4× 1.4× 3.08
[140]	30.25	4.9 %/ 40 dB	N.A	N.A	2.5× 2.5× 3.08
This Work	30	23.4 %/ 20 dB	10.5 dBi	-20 dB/ -20 dB	1.2 × 1.2× 0.27

results in Fig. 5.25(b). A good agreement between the simulated and the measured results can be observed, where the proposed antenna achieves a gain of 10±0.5 dBi in the whole band. Also, the co-polar (CO-Pol.) and cross-polar (X-Pol.) radiation patterns are measured at different frequencies for both polarizations. The comparison between the simulated and measured radiation patterns in both E- and H-planes for port 1 and port 2 is depicted in Fig. 5.26 and Fig. 5.27, respectively. It is noticed that both simulated and measured results are in a good agreement, where a slight discrepancy between the results is mainly because of the radiation pattern measurement setup inaccuracies or misalignment. The proposed antenna has a symmetrical radiation pattern with a low sidelobe level (less than -20 dB) for both polarization. In addition, cross-polarization levels less than -20 dB is achieved over the whole frequency band.

5.2.5 Performance Evaluation

Finally, the performance of the proposed antenna is compared with other configurations of the dual-polarized antenna implemented with different guiding technologies, which is given in Table 5.6. Compared with a patch antenna in [137], which is implemented based on LTCC technology, operating at 92.5 GHz and achieved a matching level of -7 dB with both high sidelobe level (SLL) and cross-polarization level, the proposed antenna has a

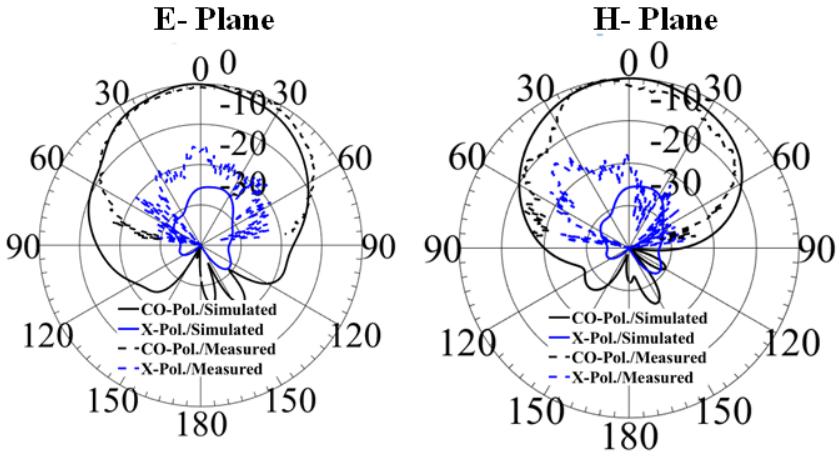

(a)

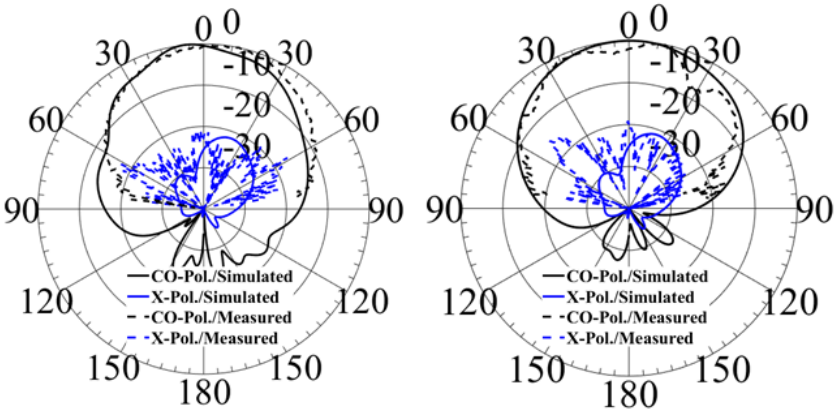

(b)

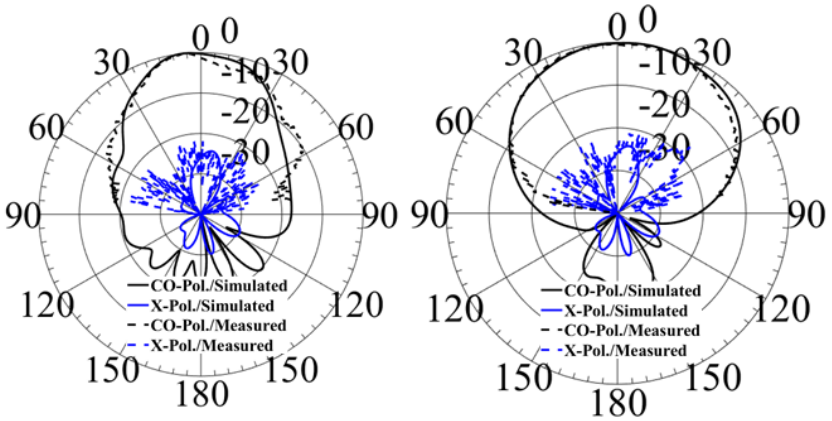

(c)

Figure 5.26: Horizontal polarized (Port 1) simulated and measured radiation pattern of the proposed dual-polarized antenna for several frequencies. (a) F=28 GHz. (b) F=30 GHz. (c) F=32 GHz.

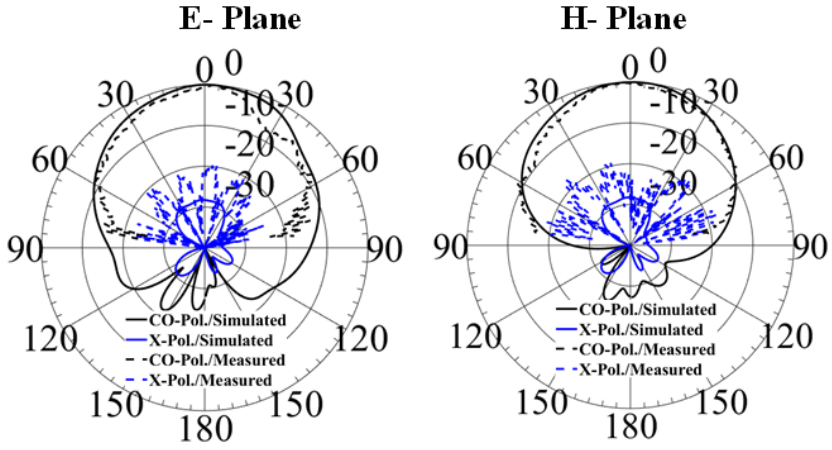

(a)

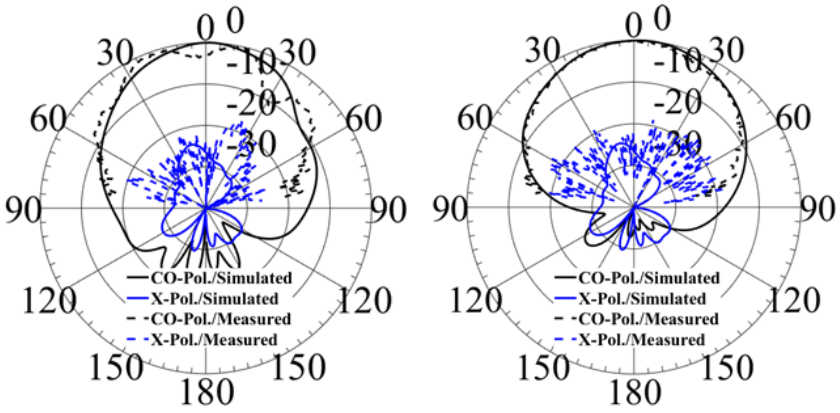

(b)

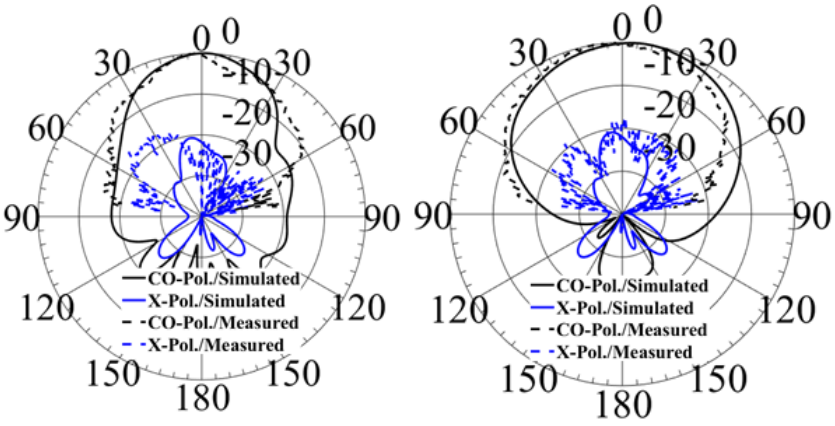

(c)

Figure 5.27: Vertical polarized (Port 2) simulated and measured radiation pattern of the proposed dual-polarized antenna for several frequencies. (a) F=28 GHz. (b) F=30 GHz. (c) F=32 GHz.

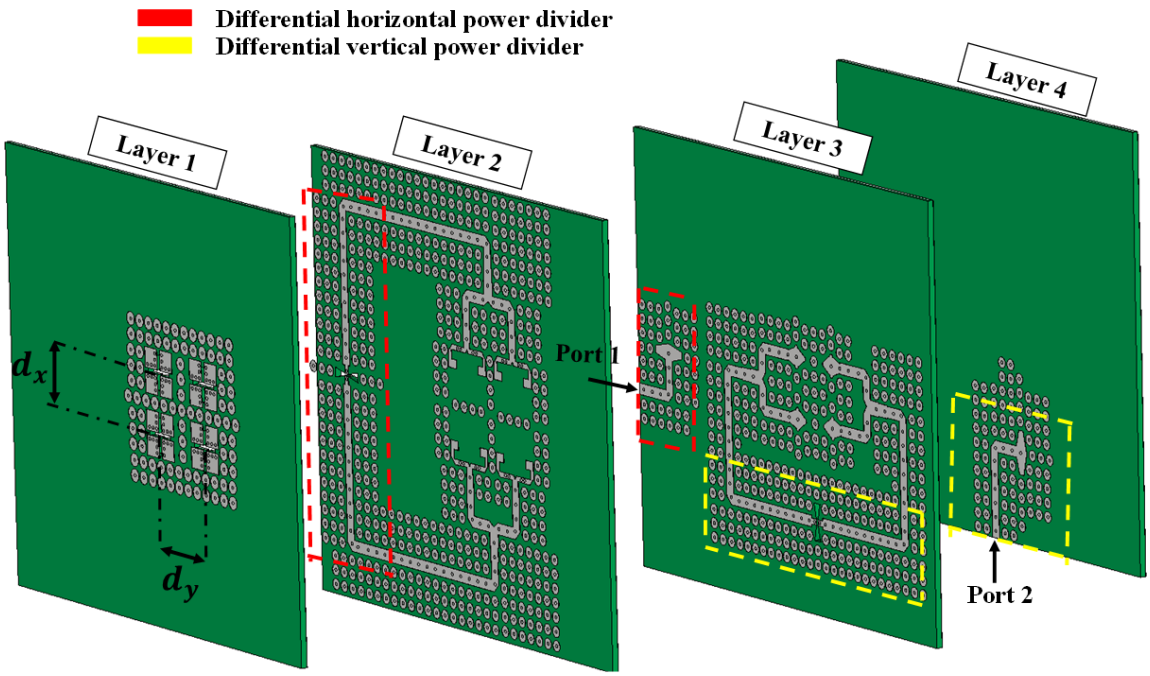

Figure 5.28: Geometrical configuration of the proposed dual polarized antenna array.

better measured matching level less than -11 dB with higher isolation and gain. A 2 × 2 cavity-backed slot antenna feeding by SIW in [138] has both high isolation level and gain compared with the proposed antenna. However, a wider bandwidth, lower isolation level, and smaller size are achieved in the proposed work. In addition, two configurations for the dual-polarized antenna are implemented based on Gap Waveguide (GW) technology and deployed the concept of cavity-backed slot antenna have been reported in [139, 140]. Although these designs have a high isolation level, the proposed antenna achieved a wider bandwidth, better isolation level, low profile, and smaller size.

5.2.6 Dual Polarized Antenna Array

In this section, a 2 × 2 array is designed based on the previously proposed dual-polarized antenna. Fig. 5.28 shows the configuration of the proposed antenna array, which consists of four layers. Layer 1 includes a 2 × 2 ME-dipole antennas, where the inter-element spacing $d_x = 8.8$ mm and $d_y = 7.4$ mm are selected to be less than λ at the center operating frequency (30 GHz) to avoid grating lobes. In order to feed the proposed antenna array, differential feeding power dividers are deployed and built-in layer 2, layer 3, and layer 4 as shown in Fig. 5.28. The purpose of using this power divider is providing an equal

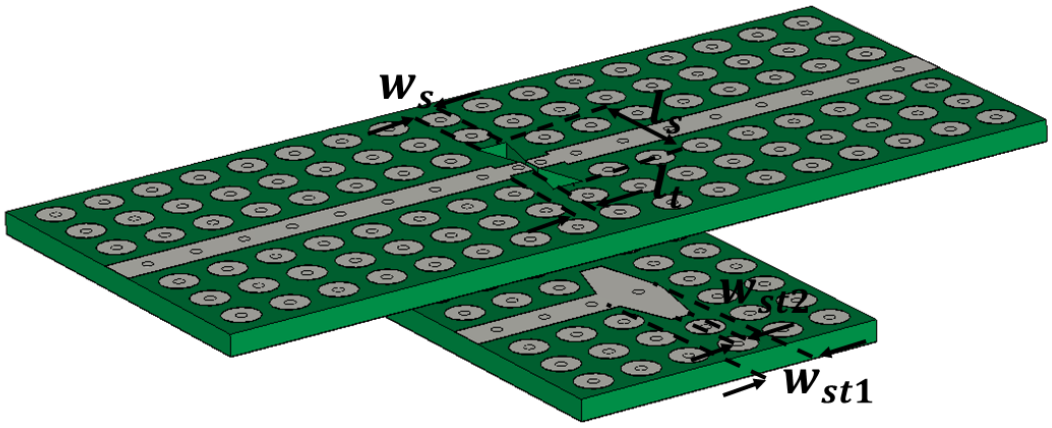

(a)

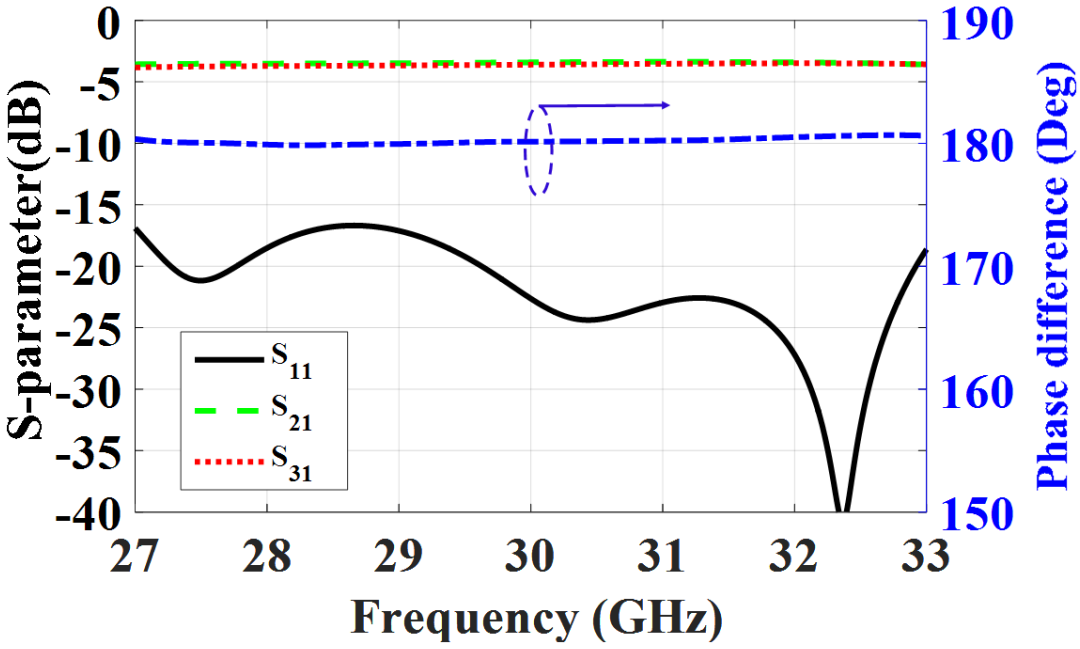

(b)

Figure 5.29: Proposed dual polarized antenna array differential power divider . (a) Configuration of differential power divider. (b) Simulated S-parameters.

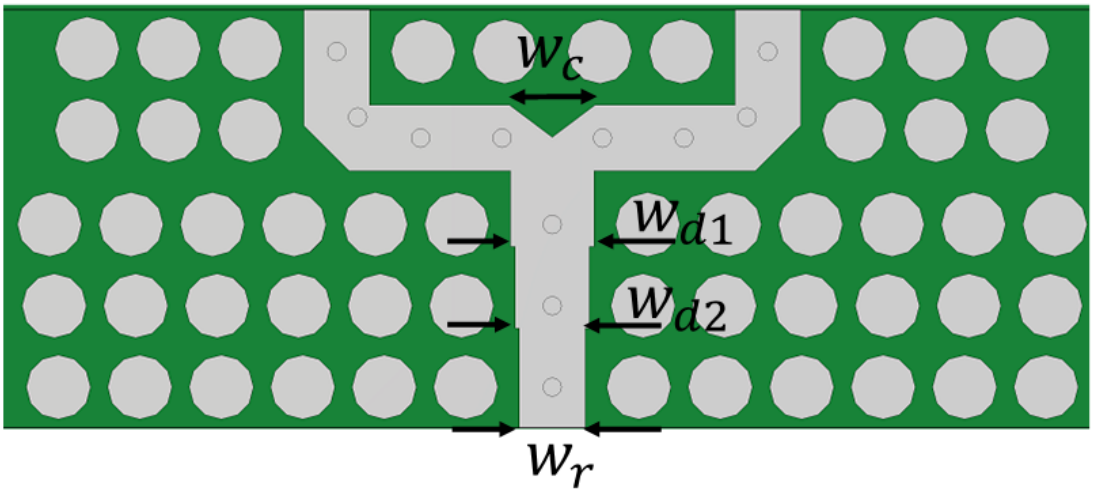

(a)

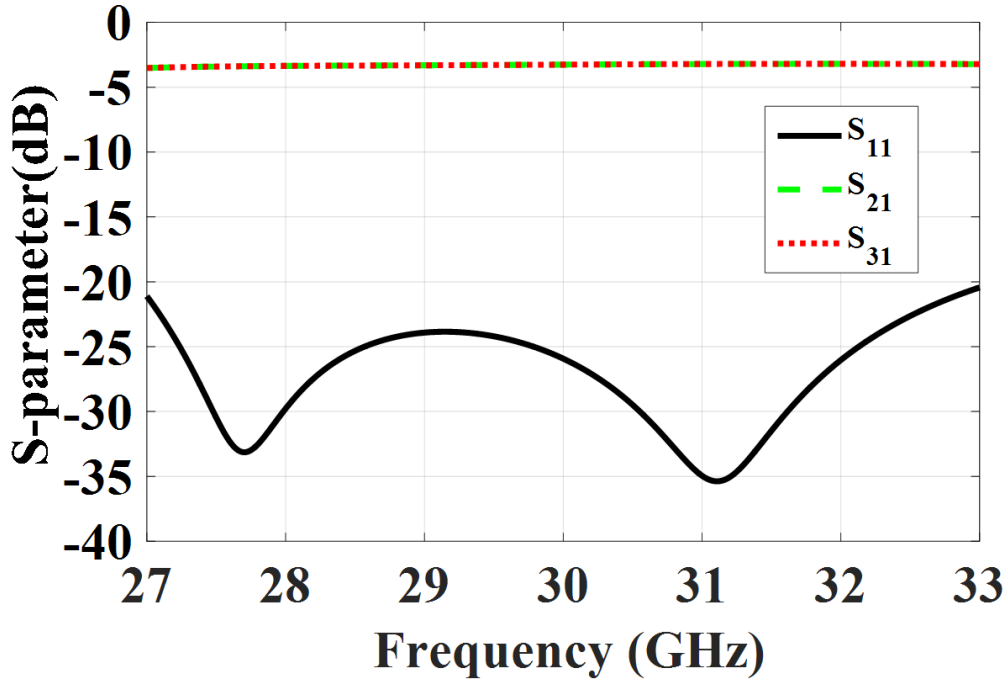

(b)

Figure 5.30: Proposed dual polarized antenna array in phase power divider. (a) Configuration of in phase power divider. (b) Simulated S-parameters.

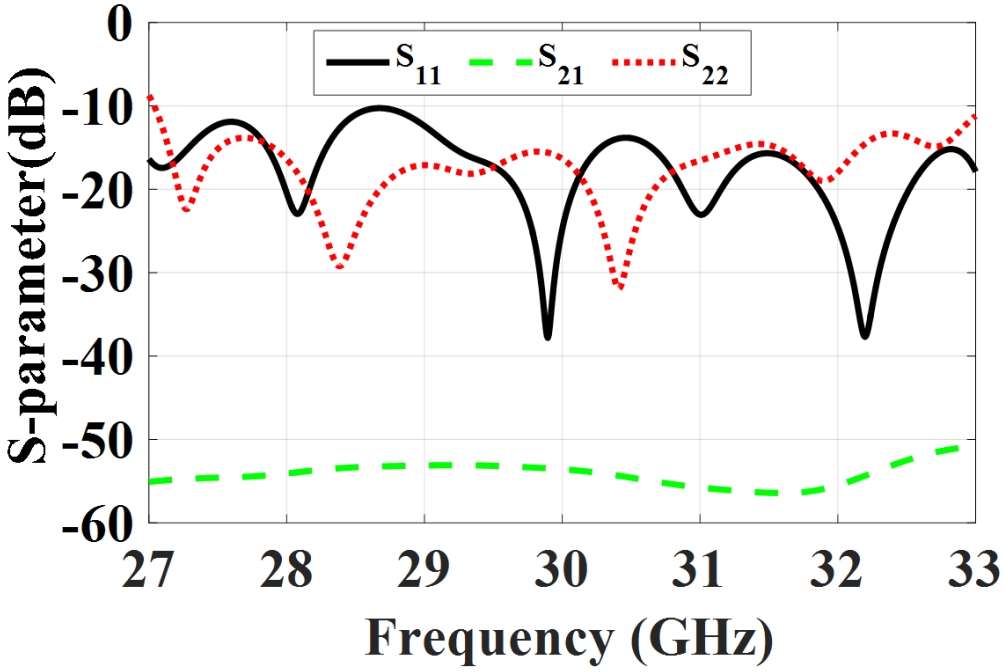

Figure 5.31: The S-parameter of the proposed dual polarized antenna array.

Table 5.7: Dimensions of the antenna array feedign power divivders

Parameters	w_s	l_s	l_t	s_st1	w_st2
Values	0.95	4.2	1.3	2.3	0.7
Parameters	w_c	w_{d1}	w_{d2}	w_r	l_{tr}
Values	1.7	1.74	1.54	1.37	1.6

power division with a stable 180^o phase difference. This will result in a stable broadside radiation pattern with low cross-polarization level and small inter-element spacing less than the free wavelength. This power divider formed by two layers coupled through a bow tie-shape slot with $\lambda/2$ length as shown in Fig. 5.29(a). To provide the proper coupling as well as the impedance bandwidth, the input power divider line is terminated with a matching stub as shown in Fig. 5.29(a). The coupling slot is incorporated with two opposite PRGW lines to provide equally split signals with 180^o phase difference to the output ports as shown in Fig. 5.29(a). Both PRGW lines located in the upper and bottom layers are designed using an EBG unit cell, which is printed on RT 6002 substrate with a relative dielectric constant of 2.94 and a thickness of 0.762 mm. The PRGW line and EBG unit cell characteristics and dimensions are addressed in the previous sections. The dimensions of the power divider are listed in Table 5.7.

The simulated S-parameters are shown in Fig. 5.29(b). This figure shows that the

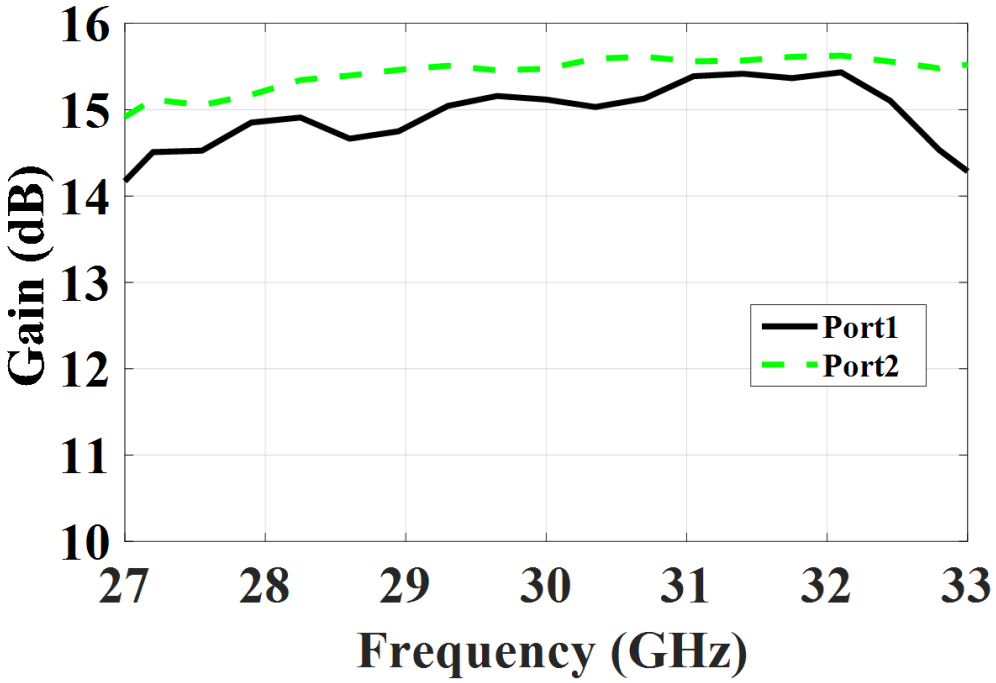

Figure 5.32: The gain of the proposed dual polarized antenna array.

proposed power divider achieves a deep matching level less than -17 dB over a 20 % relative bandwidth at 30 GHz. In addition, the power is divided equally into the two output ports with 180^o phase difference. In order to distribute the power to the four antenna elements, a 1 $\times$ 2 power divider is designed as shown in Fig. 5.30(a). Two matching transformers with length l_{tr} are used to provide a deep matching level through the whole operating bandwidth, where the power divider dimensions are listed in Table 5.7. The simulated S-parameters for the power divider is shown in Fig. 5.30(b), where a matching level less than -20 dB is achieved throughout the whole operating bandwidth.

All the previously mentioned components are assembled as shown in Fig. 5.28, where a global optimization is performed to achieve a matching level less than -10 dB for the antenna array. The simulated S-parameters for the antenna array is shown in Fig. 5.31, where simulated matching levels are less than -10 dB with an overlapped relative bandwidth of 20% at 30 GHz. Also, the isolation level higher than 50 dB is achieved over the whole operating band.

The gain of the proposed antenna array is simulated, where a gain of 15$\pm$1 dBi in the whole band is achieved as shown in Fig. 5.32. Also, the co-polar (CO-Pol.) and cross-polar (X-Pol.) radiation patterns are simulated at different frequencies for both polarizations. The simulated radiation patterns in both E- and H-planes for port 1 and

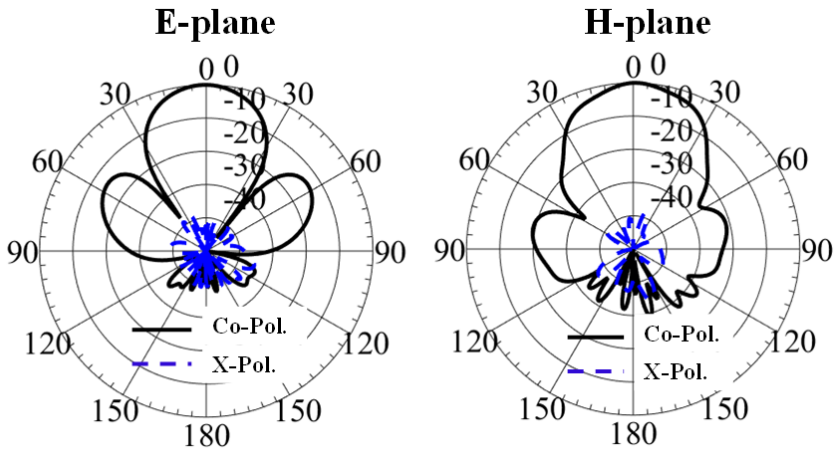

(a)

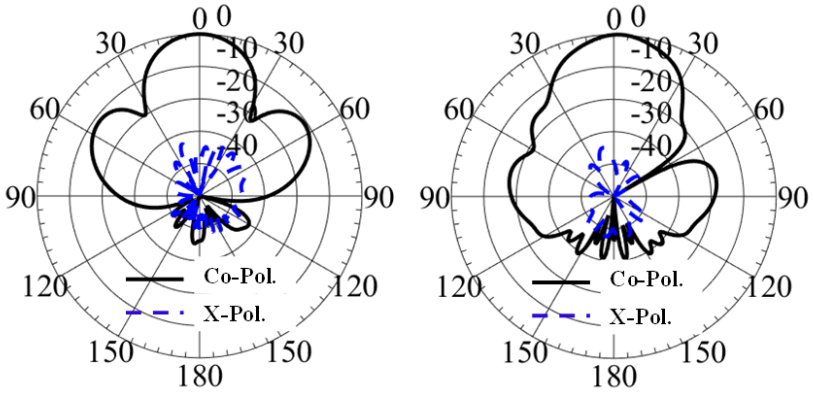

(b)

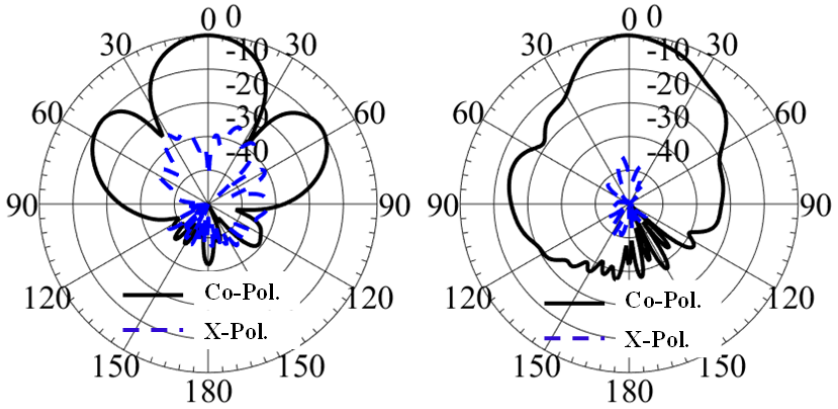

(c)

Figure 5.33: The simulated horizontal polarized (Port 1) radiation pattern of the proposed dual-polarized antenna array for several frequencies. (a) F=28 GHz. (b) F=30 GHz. (c) F=32 GHz.

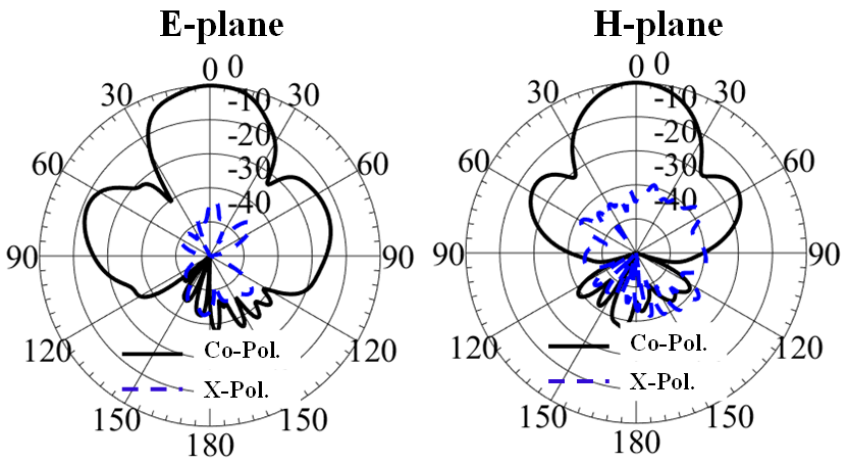

(a)

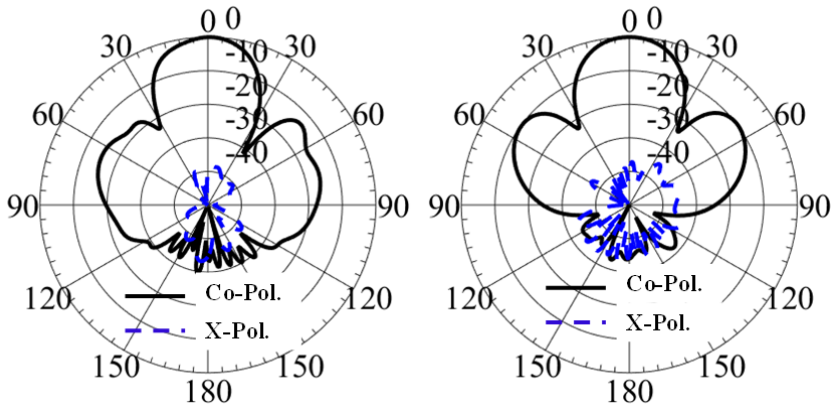

(b)

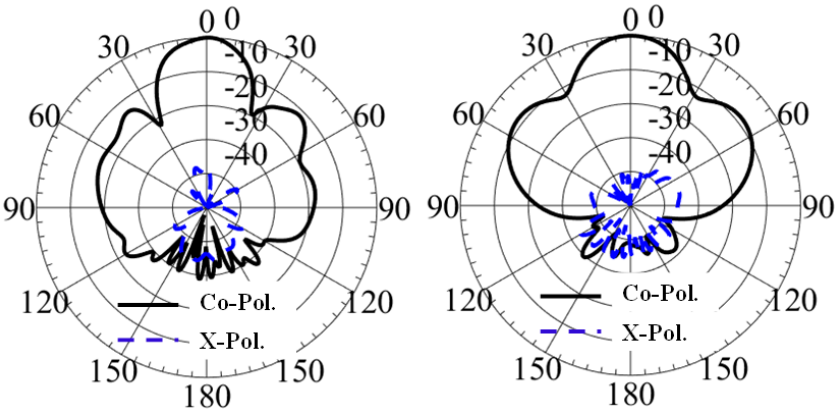

(c)

Figure 5.34: The simulated vertical polarized (Port 2) radiation pattern of the proposed dual-polarized antenna array for several frequencies when port 2 is excited . (a) F=28 GHz. (b) F=30 GHz. (c) F=32 GHz.

port 2 are depicted in Fig. 5.33 and Fig. 5.34, respectively. The proposed antenna array has a symmetrical radiation pattern with low cross-polarization levels less than -30 dB is achieved over the whole frequency band.

Chapter 6

Conclusion and Future Work

6.1 Conclusion

In this thesis, mmWave components and antennas are designed and implemented based on state of the art guiding structure such as printed ridge gap wave technology for mmWave wireless communication systems. The first part of this work has been presented several feeding structure components such as couplers and crossovers that have been designed and tested based on PRGW technology. These are considered the essential components to build beam switching system enabling the space diversity for the future mmWave wireless communications. Two different prototypes for 3-dB hybrid couplers based on PRGW technology have been proposed. The mathematical formulations and a systematic design procedure of the proposed couplers have been described. The proposed design approach has been used to achieve a compact low-loss PRGW hybrid couplers able to cover wide bandwidth up to 26 % at 30 GHz. Also, a design of crossover based on PRGW technology has been proposed. The proposed crossover has a compact size and designed to cover a 13 % relative bandwidth with more than 13.5 dB isolation levels. Design and testing of a wide bandwidth transition used to validate the proposed devices have been presented. The proposed devices have been fabricated and tested where the measured and simulated are in good agreement.

The second part has been presented beam switching mmWave antenna array designed to achieve high gain and wide bandwidth. A 4 $\times$ 4 wide bandwidth butler matrix implemented using only hybrid couplers designed in the first part have been proposed. The proposed network has a compact size and covers a 20 % relative bandwidth with a stable phase balance over the whole bandwidth. The proposed PRGW butler matrix has been used to feed a 2$\times$2 ME dipole antenna array to construct a 2-D scanning antenna array

features with a wide bandwidth of 20% and radiation efficiency higher than 84%. The proposed antenna array has been shown the ability to radiate 2-D beams, one in each quadrant at 35^o elevation angle. The proposed antenna array has been fabricated and measured, where a good agreement between the simulated and measured results has been achieved. In addition, a gain enhancement for the proposed ME-dipole two-dimensional scanning antenna array has been achieved. A hybrid gain enhancement technique including AMC mushroom shapes around the antenna array with a dielectric substrate lens located in the broadside direction has been proposed. A realized gain of 15 dB has been achieved over a 18.3 % relative operating bandwidth at 30 GHz. Also, the proposed scanning antenna array can radiate four beams with maximum radiation at 20^o from the broadside direction. Therefore, all of these features make the proposed scanning antenna array candidates for mmWave applications.

The final part has been focused on designing mmWave antenna arrays with different polarization techniques such as circular and dual polarization,where an improvement for the reliability and quality of the mmWave wireless communication link can be achieved . First, a differential feeding circularly polarized antenna array implemented with PRGW technology for mm-wave applications has been presented. The proposed antenna array is differentially fed, which offers the advantage of easy integration with differential mm-wave monolithic ICs. It is a planar structure realized by a rectangular aperture incorporated with a circular-shaped polarizer to achieve a CP radiation. The proposed antenna array has been fabricated and measured, where a measured bandwidth of 15.6% at 30 is achieved. The measured AR bandwidth and peak RHCP gain of the antenna array integrated with the differential feeding network are 10% and 13.5 dB, respectively. In addition, the proposed array has been achieved a high radiation efficiency of 84% over the entire bandwidth. This performance makes the proposed CP antenna array an an attractive candidate for practical millimeter-wave applications at 30 GHz frequency band. Second, a dual-polarized ME-dipole antenna based on PRGW technology has been presented. A cross-shaped dipole backed by a square AMC side walls cavity is deployed to achieve a radiating antenna with dual polarization. Two feeding PRGW lines located at different layers are used to excite the dual-polarized antenna through the square cavity. A cross-shaped slot is etched on the upper ground of the cavity to excited the ME-dipole antenna. The proposed antenna has been fabricated and measured where a good agree-

ment between the simulation and measured results is observed. The fabricated prototype has been shown an overlapped bandwidth of 23.4% at 30 GHz, where the isolation level between the two excited ports is higher than 20 dB over the whole bandwidth. A stable gain of 10±0.5 dB with low sidelobe level radiation patterns have been achieved through using an AMC surface around the ME-dipole antenna.

6.2 Future Work

The proposed work can be extended by exploring wider bandwidth hybrid couplers with stable amplitude balance based on printed ridge gap waveguide technology. Several techniques such as multilayer coupled patch resonator coupler or dielectric-loaded patch coupler can be deployed to achieve stable amplitude balance over a wide bandwidth. Also, the 1-D butler matrix implemented using coupler, crossover, and phase shifters can be developed based on PRGW technology. This requires to design phase shifters with stable phase balance based on PRGW technology. Furthermore, the weak coupling structure based on PRGW can be developed, which includes cross guide couplers, broad wall couplers, and loop couplers. Moreover, many nonreciprocal devices have to be designed based on the PRGW like circulators or differential phase shifters.

References

[1] Recommendation ITU-R. (2016, Jun.) Final acts of the world radiocommunication conference (WRC-15). [Online]. Available: https://www.itu.int

[2] C. X. Wang, F. Haider, X. Gao, X. H. You, Y. Yang, D. Yuan, H. M. Aggoune, H. Haas, S. Fletcher, and E. Hepsaydir, "Cellular architecture and key technologies for 5G wireless communication networks," *IEEE Communications Magazine*, vol. 52, no. 2, pp. 122–130, Feb. 2014.

[3] A. Hashimoto, H. Yoshino, and H. Atarashi, "Roadmap of IMT-advanced development," *IEEE Microwave Magazine*, vol. 9, no. 4, pp. 80–88, Aug. 2008.

[4] X. Li, A. Gani, R. Salleh, and O. Zakaria, "The future of mobile wireless communication networks," in *2009 International Conference on Communication Software and Networks*, Feb. 2009, pp. 554–557.

[5] A. Aryaputra and N. Bhuvaneshwari, "5G-the future of mobile network," in *Proceedings of the World Congress on Engineering*, vol. II, Oct. 2011, pp. 80–88.

[6] M. Tercero, P. von Wrycza, A. Amah, J. Widmer, M. Fresia, V. Frascolla, J. Lorca, T. Svensson, M. Hamon, S. Destouet Roblot, A. Vijay, M. Peter, V. Sgardoni, M. Hunukumbure, J. Luo, and N. Vucic, "5G systems: The mmmagic project perspective on use cases and challenges between 6-100 GHz," in *2016 IEEE Wireless Communications and Networking Conference*, Apr. 2016, pp. 1–6.

[7] GSMA. (2019, Jul.) 5G spectrum. [Online]. Available: www.gsma.com

[8] D. Liu, L. Wang, Y. Chen, M. Elkashlan, K. K. Wong, R. Schober, and L. Hanzo, "User association in 5G networks: A survey and an outlook," *IEEE Communications Surveys Tutorials*, vol. 18, no. 2, pp. 1018–1044, Aug. 2016.

[9] S. Ahmadi, *5G NR: Architecture, Technology, Implementation, and Operation of 3GPP New Radio Standards.* Elsevier Science, 2019.

[10] T. Bogale, X. Wang, and L. Le, "Chapter 9 - mmwave communication enabling techniques for 5g wireless systems: A link level perspective," in *mmWave Massive MIMO*, S. Mumtaz, J. Rodriguez, and L. Dai, Eds. Academic Press, 2017, pp. 195 – 225.

[11] D. M. Sheen, D. L. McMakin, and T. E. Hall, "Chapter 9 - detection of explosives by millimeter-wave imaging," in *Counterterrorist Detection Techniques of Explosives*, J. Yinon, Ed. Amsterdam: Elsevier Science B.V., 2007, pp. 237 – 277.

[12] GSMA. (2019, Oct.) Enabling IMT at WRC-19. [Online]. Available: www.gsma.com

[13] Recommendation ITU-R. (2019, Nov.) Final acts of the world radiocommunication conference (WRC-19). [Online]. Available: https://www.itu.int

[14] M. Medin and G. Louie, *The 5G Ecosystem: Risks and Opportunities for DoD*. Defense Innovation Board, Apr. 2019.

[15] K. Millar. (2014, Mar.) Britain, germany to collaborate on 5g next mobile network. [Online]. Available: https://phys.org

[16] Recommendation ITU-R. (2017, Nov.) Minimum requirements related to technical performance for IMT-2020 radio interface(s). [Online]. Available: https://www.itu.int

[17] J. C. Gallagher and M. E. DeVine. (2019, Jan.) Fifth-generation (5G) telecommunications technologies: Issues for congress. [Online]. Available: https://crsreports.congress.gov/

[18] B. P. S. Sahoo, C. Chou, C. Weng, and H. Wei, "Enabling millimeter-wave 5G networks for massive iot applications: A closer look at the issues impacting millimeter-waves in consumer devices under the 5G framework," *IEEE Consumer Electronics Magazine*, vol. 8, no. 1, pp. 49–54, Jan. 2019.

[19] E. Ali, M. Ismail, R. Nordin, and N. F. Abdulah, "Beamforming techniques for massive MIMO systems in 5G: overview, classification, and trends for future research," *Frontiers of Information Technology & Electronic Engineering*, vol. 18, no. 6, pp. 753–772, Jun. 2017.

[20] J.-K. Hong, "Performance analysis of dual-polarized massive MIMO system with human-care iot devices for cellular networks„" *Journal of Sensors*, vol. 2018, pp. 1–8, Apr. 2018.

[21] O. Jo, J. Kim, J. Yoon, D. Choi, and W. Hong, "Exploitation of dual-polarization diversity for 5G millimeter-wave MIMO beamforming systems," *IEEE Transactions on Antennas and Propagation*, vol. 65, no. 12, pp. 6646–6655, Dec. 2017.

[22] M. L. Coq, E. Rius, J. F. Favennec, C. Quendo, B. Potelon, L. Estagerie, P. Moroni, B. Bonnet, and A. E. Mostrah, "Miniaturized C-band SIW filters using high-permittivity ceramic substrates," *IEEE Transactions on Components, Packaging and Manufacturing Technology*, vol. 5, no. 5, pp. 620–626, May 2015.

[23] A. Ali, H. Aubert, N. Fonseca, and F. Coccetti, "Wideband two-layer SIW coupler: design and experiment," *Electronics Letters*, vol. 45, no. 13, pp. 687–689, Jun. 2009.

[24] S. I. Shamseldin, "Analysis and design of microwave devices based on ridge gap waveguide technology," Ph.D. dissertation, ECE Dept.,Concordia University, Montreal, Canada, 2016.

[25] M. S. Sorkherizi, A. Khaleghi, and P. S. Kildal, "Direct-coupled cavity filter in ridge gap waveguide," *IEEE Transactions on Components, Packaging and Manufacturing Technology*, vol. 4, no. 3, pp. 490–495, Mar. 2014.

[26] S. I. Shams and A. A. Kishk, "Printed texture with triangle flat pins for bandwidth enhancement of the ridge gap waveguide," *IEEE Transactions on Microwave Theory and Techniques*, vol. 65, no. 6, pp. 2093–2100, Jun. 2017.

[27] M. S. Sorkherizi, "Microwave filters based on new design concepts in several technologies with emphasis on the printed ridge gap waveguide technology," Ph.D. dissertation, ECE Dept.,Concordia University, Montreal, Canada, 2016.

[28] M. Sharifi Sorkherizi and A. A. Kishk, "Fully printed gap waveguide with facilitated design properties," *IEEE Microwave and Wireless Components Letters*, vol. 26, no. 9, pp. 657–659, Sept. 2016.

[29] S. S. Syed Nasser, W. Liu, and Z. N. Chen, "Wide bandwidth and enhanced gain of a low-profile dipole antenna achieved by integrated suspended metasurface," *IEEE*

Transactions on Antennas and Propagation, vol. 66, no. 3, pp. 1540–1544, March 2018.

[30] M. H. M. Shamim, H. Attia, M. S. Sharawi, and A. A. Kishk, "60 GHz circularly polarized dielectric resonator antenna fed by printed ridge gap waveguide," in *2017 IEEE 28th Annual International Symposium on Personal, Indoor, and Mobile Radio Communications (PIMRC)*, 2017, pp. 1–4.

[31] M. Sharifi Sorkherizi, A. Dadgarpour, and A. A. Kishk, "Planar high-efficiency antenna array using new printed ridge gap waveguide technology," *IEEE Transactions on Antennas and Propagation*, vol. 65, no. 7, pp. 3772–3776, July 2017.

[32] Li Ding and P. Mazumder, "On circuit techniques to improve noise immunity of cmos dynamic logic," *IEEE Transactions on Very Large Scale Integration (VLSI) Systems*, vol. 12, no. 9, pp. 910–925, Sept. 2004.

[33] B. S. W. R. Eisenstadt and B. M. Thompson, *Microwave Differential Circuit Design Using Mixed-Mode S-Parameters*. USA: Artech House, 2006.

[34] J. Xu, Z. N. Chen, and Q. Xianming, "A broadband circularly polarized antenna," in *2012 IEEE Asia-Pacific Conference on Antennas and Propagation*, Aug. 2012, pp. 43–44.

[35] J. Wang, Z. Lv, and X. Li, "Analysis of MIMO diversity improvement using circular polarized antenna," *International Journal of Antennas and Propagation*, vol. 2014, pp. 1–9, Feb. 2014.

[36] H. Lin and Y. Lin, "Millimeter-wave MIMO antennas with polarization and pattern diversity for 5G mobile communications: The corner design," in *2017 IEEE International Symposium on Antennas and Propagation USNC/URSI National Radio Science Meeting*, Jul. 2017, pp. 2577–2578.

[37] B. Lindmark and M. Nilsson, "On the available diversity gain from different dual-polarized antennas," *Selected Areas in Communications, IEEE Journal on*, vol. 19, pp. 287 – 294, Mar. 2001.

[38] M. M. M. Ali, S. I. Shams, and A. Sebak, "Printed ridge gap waveguide 3-dB coupler: Analysis and design procedure," *IEEE Access*, vol. 6, pp. 8501–8509, Dec. 2018.

[39] M. M. M. Ali, S. I. Shams and A. Sebak, "Ultra-wideband printed ridge gap waveguide hybrid directional coupler for millimetre wave applications," *IET Microwaves, Antennas and Propagation*, vol. 6, pp. 8501–8509, Jun. 2019.

[40] M. M. M. Ali and A. Sebak, "Compact printed ridge gap waveguide crossover for future 5G wireless communication system," *IEEE Microwave and Wireless Components Letters*, vol. 28, no. 7, pp. 549–551, Jul. 2018.

[41] M. M. M. Ali and A. Sebak, "2-D scanning magnetoelectric dipole antenna array fed by RGW butler matrix," *IEEE Transactions on Antennas and Propagation*, vol. 66, no. 11, pp. 6313–6321, Nov. 2018.

[42] M. M. M. Ali and A. Sebak, "Printed RGW circularly polarized differential feeding antenna array for 5G communications," *IEEE Transactions on Antennas and Propagation*, vol. 67, no. 5, pp. 3151–3160, May 2019.

[43] M. M. M. Ali, Islam Afifi and A. Sebak, "A dual polarized magneto-electric dipole antenna based on printed ridge gap waveguide technology," *in IEEE Transactions on Antennas and Propagation*, 2019.

[44] M. V. Schneider, "Microstrip lines for microwave integrated circuits," *Bell System Technical Journal*, vol. 48, no. 5, pp. 1421–1444, 1969.

[45] N. S. I. Robertson and M. Chongcheawchamnan, *Microwave and Millimetre-Wave Design for Wireless Communications*. New York: John Wiley and Sons Ltd, 2016.

[46] L. Y, *Microwave Devices and Circuits*. Pearson Education, 1989.

[47] I. B. R. Mongia and P. Bhartia, *RF and Microwave Coupled-Line Circuits*. Norwood, MA: Artech House,, 1999.

[48] E. Rajo-Iglesias, M. Ferrando-Rocher, and A. U. Zaman, "Gap waveguide technology for millimeter-wave antenna systems," *IEEE Communications Magazine*, vol. 56, no. 7, pp. 14–20, Jul. 2018.

[49] "Electromagnetic waves guided by corrugated conducting surfaces," *Bell Telephone Labs. Report MM-44-160-218*, vol. 2, no. 2, pp. 71–81, October 1944.

[50] P. S. Kildal, "Definition of artificially soft and hard surfaces for electromagnetic waves," *Electronics Letters*, vol. 24, no. 3, pp. 168–170, Feb. 1988.

[51] P. S. Kildal, E. Alfonso, A. Valero-Nogueira, and E. Rajo-Iglesias, "Local metamaterial-based waveguides in gaps between parallel metal plates," *IEEE Antennas and Wireless Propagation Letters*, vol. 8, pp. 84–87, Dec. 2009.

[52] S. I. Shams and A. A. Kishk, "Wideband coaxial to ridge gap waveguide transition," *IEEE Transactions on Microwave Theory and Techniques*, vol. 64, no. 12, pp. 4117–4125, Dec 2016.

[53] S.I.Shams and A. A. Kishk, "Wide band power divider based on ridge gap waveguide," in *Antenna Technology and Applied Electromagnetics (ANTEM), 2016 17th International Symposium on*. IEEE, 2016, pp. 1–2.

[54] S. I. Shams and A. A. Kishk, "Determining the stopband of a periodic bed of nails from the dispersion relation measurements prediction," *IEEE Transactions on Components, Packaging and Manufacturing Technology*, vol. 7, no. 4, pp. 621–629, 2017.

[55] A. Polemi, S. Maci, and P. S. Kildal, "Dispersion characteristics of a metamaterial-based parallel-plate ridge gap waveguide realized by bed of nails," *IEEE Transactions on Antennas and Propagation*, vol. 59, no. 3, pp. 904–913, Mar. 2011.

[56] J. B. Z. Sipus and S. Hrabar, "Per-simon kildal and design of electromagnetic structures: Outstanding combination of scientific concepts and engineering intuition," in *2017 IEEE Antennas and Propagation Society International Symposium*, Jul. 2017, pp. 1193–1196.

[57] A. Farahbakhsh, D. Zarifi, and A. U. Zaman, "60-GHz groove gap waveguide based wideband *h*-plane power dividers and transitions: For use in high-gain slot array antenna," *IEEE Transactions on Microwave Theory and Techniques*, vol. PP, no. 99, pp. 1–11, 2017.

[58] A. J. Sáez, A. Valero-Nogueira, J. I. Herranz, and B. Bernardo, "Single-layer cavity-backed slot array fed by groove gap waveguide," *IEEE Antennas and Wireless Propagation Letters*, vol. 15, 2016.

[59] J. I. H. Herruzo, A. Valero-Nogueira, S. M. Giner, and A. V. Jiménez, "Untilted narrow-wall slots excited by parasitic dipoles in groove gap waveguide technology," *IEEE Transactions on Antennas and Propagation*, vol. 63, no. 11, pp. 4759–4765, Nov 2015.

[60] A. A. Brazález, E. Rajo-Iglesias, J. L. Vázquez-Roy, A. Vosoogh, and P. S. Kildal, "Design and validation of microstrip gap waveguides and their transitions to rectangular waveguide, for millimeter-wave applications," *IEEE Transactions on Microwave Theory and Techniques*, vol. 63, no. 12, pp. 4035–4050, Dec 2015.

[61] E. Pucci, "Gap waveguide technology for millimeter wave applications and integration with antennas," Master's thesis, Department of Signals and Systems Chalmers University of Technology, 2013.

[62] A. A. Kishk and A. T. Hassan, "Design of large finite array antennas and its feeding network," in *2019 IEEE International Conference on Computational Electromagnetics (ICCEM)*, Mar. 2019, pp. 1–3.

[63] A. T. Hassan and A. A. Kishk, "Microstrip ridge gap waveguide hybrid coupler at 60 GHz," in *2018 IEEE International Symposium on Antennas and Propagation USNC/URSI National Radio Science Meeting*, Jul. 2018, pp. 427–428.

[64] A. T. Hassan, M. A. Moharram, and A. A. Kishk, "Empirical analysis formulae of microstrip ridge gap waveguide," in *2018 IEEE International Symposium on Antennas and Propagation USNC/URSI National Radio Science Meeting*, Jul. 2018, pp. 423–424.

[65] S. I. Shams, M. A. Abdelaal, and A. A. Kishk, "SIW magic tee fed by printed ridge gap waveguide design," in *Antenna Technology and Applied Electromagnetics (ANTEM), 2016 17th International Symposium on.* IEEE, 2016, pp. 1–2.

[66] Z. Pi, J. Choi, and R. Heath, "Millimeter-wave gigabit broadband evolution toward 5G: fixed access and backhaul," *IEEE Communications Magazine*, vol. 54, no. 4, pp. 138–144, April 2016.

[67] D. Panda and S. Shaikh, "Linear, non-linear adaptive beamforming algorithm for smart antenna system," Sept. 2015.

[68] A. Natarajan, A. Valdes-Garcia, B. Sadhu, S. K. Reynolds, and B. D. Parker, "*w*-band dual-polarization phased-array transceiver front-end in sige bicmos," *IEEE Transactions on Microwave Theory and Techniques*, vol. 63, no. 6, pp. 1989–2002, June 2015.

[69] P. Chen, W. Hong, Z. Kuai, and J. Xu, "A double layer substrate integrated waveguide blass matrix for beamforming applications," *IEEE Microwave and Wireless Components Letters*, vol. 19, no. 6, pp. 374–376, June 2009.

[70] Y. Gao, M. Khaliel, F. Zheng, and T. Kaiser, "Rotman lens based hybrid analog–digital beamforming in massive mimo systems: Array architectures, beam selection algorithms and experiments," *IEEE Transactions on Vehicular Technology*, vol. 66, no. 10, pp. 9134–9148, Oct 2017.

[71] A. Darvazehban, O. Manoochehri, M. A. Salari, P. Dehkhoda, and A. Tavakoli, "Ultra-wideband scanning antenna array with rotman lens," *IEEE Transactions on Microwave Theory and Techniques*, vol. 65, no. 9, pp. 3435–3442, Sep. 2017.

[72] T. Djerafi, N. J. G. Fonseca, and K. Wu, "Broadband substrate integrated waveguide 4×4 nolen matrix based on coupler delay compensation," *IEEE Transactions on Microwave Theory and Techniques*, vol. 59, pp. 1740–1745, 2011.

[73] Q. Yang, Y. Ban, K. Kang, C. Sim, and G. Wu, "SIW multibeam array for 5G mobile devices," *IEEE Access*, vol. 4, pp. 2788–2796, 2016.

[74] A. B. Guntupalli, T. Djerafi, and K. Wu, "Two-dimensional scanning antenna array driven by integrated waveguide phase shifter," *IEEE Transactions on Antennas and Propagation*, vol. 62, no. 3, pp. 1117–1124, March 2014.

[75] Y. Cao, K. Chin, W. Che, W. Yang, and E. S. Li, "A compact 38 GHz multibeam antenna array with multifolded butler matrix for 5G applications," *IEEE Antennas and Wireless Propagation Letters*, vol. 16, pp. 2996–2999, 2017.

[76] J. Lian, Y. Ban, Q. Yang, B. Fu, Z. Yu, and L. Sun, "Planar millimeter-wave 2-D beam-scanning multibeam array antenna fed by compact SIW beam-forming network," *IEEE Transactions on Antennas and Propagation*, vol. 66, no. 3, pp. 1299–1310, March 2018.

[77] Y. J. Cheng, W. Hong, and K. Wu, "Millimeter-wave multibeam antenna based on eight-port hybrid," *IEEE Microwave and Wireless Components Letters*, vol. 19, no. 4, pp. 212–214, April 2009.

[78] C. Dall'Omo, T. Monediere, B. Jecko, F. Lamour, I. Wolk, and M. Elkael, "Design and realization of a 4×4 microstrip butler matrix without any crossing in millimeter waves," *Microwave and Optical Technology Letters*, vol. 38, no. 6, pp. 462–465, 2003.

[79] W. F. Moulder, W. Khalil, and J. L. Volakis, "60-GHz two-dimensionally scanning array employing wideband planar switched beam network," *IEEE Antennas and Wireless Propagation Letters*, vol. 9, pp. 818–821, 2010.

[80] Y. Li and K. Luk, "A multibeam end-fire magnetoelectric dipole antenna array for millimeter-wave applications," *IEEE Transactions on Antennas and Propagation*, vol. 64, no. 7, pp. 2894–2904, July 2016.

[81] F. C. Suarez, D. C. Mendez, and M. Baquero-Escudero, "Rotman lens with ridge gap waveguide technology for millimeter wave applications," *2013 7th European Conference on Antennas and Propagation (EuCAP)*, pp. 4006–4009, 2013.

[82] A. Dadgarpour, M. S. Sorkherizi, T. A. Denidni, and A. A. Kishk, "Passive beam switching and dual-beam radiation slot antenna loaded with enz medium and excited through ridge gap waveguide at millimeter-waves," *IEEE Transactions on Antennas and Propagation*, vol. 65, no. 1, pp. 92–102, Jan 2017.

[83] J. Pourahmadazar and T. Denidni, "V-band printed ridge gap waveguide phased array antenna with $\pm 40^\circ$ scanning angular sector and etsi class ii radiation pat-

tern," in *2018 18th International Symposium on Antenna Technology and Applied Electromagnetics (ANTEM)*, Aug 2018, pp. 1–2.

[84] S. I. Shams, M. A. Abdelaal, and A. A. Kishk, "Broadside uniform leaky-wave slot array fed by ridge gap splitted line," in *2015 IEEE International Symposium on Antennas and Propagation USNC/URSI National Radio Science Meeting*, 2015, pp. 2467–2468.

[85] H. L. Ting, S. K. Hsu, and T. L. Wu, "A novel and compact eight-port forward-wave directional coupler with arbitrary coupling level design using four-mode control technology," *IEEE Transactions on Microwave Theory and Techniques*, vol. 65, no. 2, pp. 467–475, Feb. 2017.

[86] S. Y. Zheng, J. H. Deng, Y. M. Pan, and W. S. Chan, "Circular sector patch hybrid coupler with an arbitrary coupling coefficient and phase difference," *IEEE Transactions on Microwave Theory and Techniques*, vol. 61, no. 5, pp. 1781–1792, May 2013.

[87] T. Kawai and I. Ohta, "Planar-circuit-type 3-dB quadrature hybrids," *IEEE Transactions on Microwave Theory and Techniques*, vol. 42, no. 12, pp. 2462–2467, Dec. 1994.

[88] X. F. Ye, S. Y. Zheng, and Y. M. Pan, "A compact millimeter-wave patch quadrature coupler with a wide range of coupling coefficients," *IEEE Microwave and Wireless Components Letters*, vol. 26, no. 3, pp. 165–167, Mar. 2016.

[89] M. G. Pischenko, D. G. Pischenko, and M. B. Manuilov, "Wide band strip-line microwave directional coupler for high power operation," in *2016 International Conference on Actual Problems of Electron Devices Engineering (APEDE)*, vol. 1, Sept. 2016, pp. 1–4.

[90] L. T. Hildebrand, "Results for a simple compact narrow-wall directional coupler," *IEEE Microwave and Guided Wave Letters*, vol. 10, no. 6, pp. 231–232, Jun. 2000.

[91] H. J. Riblet, "The short-slot hybrid junction," *Proceedings of the IRE*, vol. 40, no. 2, pp. 180–184, Feb. 1952.

[92] T. Djerafi and K. Wu, "Super-compact substrate integrated waveguide cruciform directional coupler," *IEEE Microwave and Wireless Components Letters*, vol. 17, no. 11, pp. 757–759, Nov. 2007.

[93] T. Li and W. Dou, "Substrate integrated waveguide 3 dB directional coupler based on air-filled vias," *Electronics Letters*, vol. 53, no. 9, pp. 611–613, May 2017.

[94] B. Liu, W. Hong, Y. Zhang, H. J. Tang, X. Yin, and K. Wu, "Half mode substrate integrated waveguide 180° 3-dB directional couplers," *IEEE Transactions on Microwave Theory and Techniques*, vol. 55, no. 12, pp. 2586–2592, Dec. 2007.

[95] Y. Li and K. M. Luk, "60-GHz dual-polarized two-dimensional switch-beam wideband antenna array of aperture-coupled magneto-electric dipoles," *IEEE Transactions on Antennas and Propagation*, vol. 64, no. 2, pp. 554–563, Feb. 2016.

[96] X. C. F. H. L. Han, K. Wu, "Accurate and efficient design technique for wideband substrate integrated waveguide directional couplers," *International Journal of RF and Microwave Computer-Aided Engineering*, vol. 22, no. 2, pp. 248–259, Mar. 2012.

[97] A. Doghri, T. Djerafi, A. Ghiotto, and K. Wu, "Substrate integrated waveguide directional couplers for compact three-dimensional integrated circuits," *IEEE Transactions on Microwave Theory and Techniques*, vol. 63, no. 1, pp. 209–221, Jan. 2015.

[98] T. P. V. J. M. D. F. Parment, A. Ghiotto and K. Wu, "Air-filled substrate integrated waveguide for low-loss and high power-handling millimeter-wave substrate integrated circuits," *IEEE Trans. Microw. Theory Techn.*, pp. 1228–1238, Apr. 2015.

[99] S. I. Shams and A. A. Kishk, "Design of 3-dB hybrid coupler based on RGW technology," *IEEE Transactions on Microwave Theory and Techniques*, vol. PP, no. 99, pp. 1–7, 2017.

[100] D. Zarifi and A. R. Shater, "Design of a 3-dB directional coupler based on groove gap waveguide technology," *Microwave and Optical Technology Letters*, vol. 59, no. 7, pp. 1597–1600, 2017.

[101] M. Farahani, M. Akbari, M. Nedil, T. A. Denidni, and A. R. Sebak, "A novel low-loss millimeter-wave 3-dB 90 ridge-gap coupler using large aperture progressive phase compensation," *IEEE Access*, vol. 5, pp. 9610–9618, 2017.

[102] D. Shen, K. Wang, and X. Zhang, "A substrate integrated gap waveguide based wideband 3-dB coupler for 5G applications," *IEEE Access*, vol. 6, pp. 66 798–66 806, 2018.

[103] J. S. Wight, W. J. Chudobiak, and V. Makios, "A microstrip and stripline crossover structure (letters)," *IEEE Transactions on Microwave Theory and Techniques*, vol. 24, no. 5, pp. 270–270, May 1976.

[104] K. Murai, H. Ikeuchi, T. Kawai, M. Kishihara, and I. Ohta, "Broadband design method of SIW directional couplers," in *2011 China-Japan Joint Microwave Conference*, April 2011, pp. 1–4.

[105] N. J. G. F. T. Djerafi and K. Wu, "Design and implementation of a planar 4x4 butler matrix in SIW technology for wide band high power applications," *Progress In Electromagnetics Research B*, vol. 35, pp. 29–51, May 2011.

[106] A. B. Guntupalli, T. Djerafi, and K. Wu, "Ultra-compact millimeter-wave substrate integrated waveguide crossover structure utilizing simultaneous electric and magnetic coupling," in *2012 IEEE/MTT-S International Microwave Symposium Digest*, June 2012, pp. 1–3.

[107] S. Y. Zheng and X. F. Ye, "Ultra-compact wideband millimeter-wave crossover using slotted SIW structure," in *2016 IEEE International Workshop on Electromagnetics: Applications and Student Innovation Competition (iWEM)*, May 2016, pp. 1–2.

[108] N. Ashraf, A. A. Kishk, and A. Sebak, "Broadband millimeter-wave beamforming components augmented with amc packaging," *IEEE Microwave and Wireless Components Letters*, vol. 28, no. 10, pp. 879–881, Oct 2018.

[109] S. Birgermajer, N. Janković, V. Crnojević-Bengin, M. Bozzi, and V. Radonić, "Forward-wave 0 dB directional coupler based on microstrip-ridge gap waveguide technology," in *2017 13th International Conference on Advanced Technologies, Systems and Services in Telecommunications (TELSIKS)*, Oct 2017, pp. 154–157.

[110] G. B. Abdelsayed, S. I. Shams, and A. Allam, "Triple-band circularly polarized slotted patch antenna for gps and umts systems," in *Microwave Symposium (MMS), 2010 Mediterranean*. IEEE, 2010, pp. 448–451.

[111] N. Ashraf, O. M. Haraz, M. M. M. Ali, M. A. Ashraf, and S. A. S. Alshebili, "Optimized broadband and dual-band printed slot antennas for future millimeter wave mobile communication," *AEU-International Journal of Electronics and Communications*, vol. 70, no. 3, pp. 257–264, 2016.

[112] M. Azer, S. I. Shams, and A. Allam, "Compact double-sided printed omni-directional ultra wideband antenna," in *Antenna Technology and Applied Electromagnetics & the American Electromagnetics Conference (ANTEM-AMEREM), 2010 14th International Symposium on*. IEEE, 2010, pp. 1–4.

[113] M. M .M .Ali and A. A . R.Saad and E. E. M.Khaled, "A design of miniaturized ultra–wideband printed slot antenna with 3.5/5.5 GHz dual band–notched characteristics: analysis and implementation," *Progress In Electromagnetics Research B*, vol. 52, pp. 37–56, 2013.

[114] M. M .M .Ali, A. A. . R.Saad, and E. E. M.Khaled, "Implementation and justification of a triple frequency-notched uwb proximity-fed antenna with shunt stubs," *Microwave and Optical Technology Letters*, vol. 56, no. 3, pp. 646–654, 2014.

[115] M. M .M .Ali and A. A . R.Saad and E. E. M.Khaled, "A microstrip-fed printed slot antenna for 3G/Bluetooth/WiMAX and uwb applications with 3.6 GHz band rejection," in *PIERS Proceedings*, 2013, pp. 588–592.

[116] O. Hassan, S. I. Shams, and A. Allam, "Dual-band circularly polarized antenna with cpw feeding structure," in *Microwave Conference Proceedings (APMC), 2010 Asia-Pacific*. IEEE, 2010, pp. 2052–2055.

[117] A. A. R. Saad and M .M. M. Ali and E. E. E .Khaled, "Curve-fitting formulas for fast determination of frequency band-notched response of uwb antennas," *Session 1A6 SC1&4: Antenna Modeling and Simulation*, p. 80, 2013.

[118] H. Awadalla, S. I. Shams, and A. Amma, "A compact, symmetric u-shaped monopole for ultra wide band operation," in *Radio Science Conference (NRSC), 2011 28th National*. IEEE, 2011, pp. 1–7.

[119] A. A. R. Saad, M. M. M. Ali, and E. E. E. .Khaled, "Prediction formulas for a notched frequency response of a printed ultra-wideband antenna loaded with notching resonators," *The Journal of Engineering*, vol. 1, no. 1, 2013.

[120] H. M. Mansour, M. H. Sharaf, S. I. Shams, and A. M. Allam, "Novel lotus shaped antenna for ultra wideband communication systems," in *Antennas and Propagation Conference (LAPC), 2012 Loughborough*. IEEE, 2012, pp. 1–4.

[121] M. M. M. .Ali, O. Haraz, I. Elshafiey, S. Alshebeili, and A.-R. Sebak, "Efficient single-band and dual-band antennas for microwave imaging and hyperthermia treatment of brain tumors," in *Control System, Computing and Engineering (ICCSCE), 2014 IEEE International Conference on*. IEEE, 2014, pp. 597–600.

[122] M. M. M. Ali and A.-R. Sebak, "Dual band (28/38 GHz) cpw slot directive antenna for future 5G cellular applications," in *Antennas and Propagation (APSURSI), 2016 IEEE International Symposium on*. IEEE, 2016, pp. 399–400.

[123] D. J. Bisharat, S. Liao, and Q. Xue, "High gain and low cost differentially fed circularly polarized planar aperture antenna for broadband millimeter-wave applications," *IEEE Transactions on Antennas and Propagation*, vol. 64, no. 1, pp. 33–42, Jan. 2016.

[124] S. Liao, P. Wu, K. M. Shum, and Q. Xue, "Differentially fed planar aperture antenna with high gain and wide bandwidth for millimeter-wave application," *IEEE Transactions on Antennas and Propagation*, vol. 63, no. 3, pp. 966–977, Mar. 2015.

[125] Q. Xue, S. W. Liao, and J. H. Xu, "A differentially-driven dual-polarized magneto-electric dipole antenna," *IEEE Transactions on Antennas and Propagation*, vol. 61, no. 1, pp. 425–430, Jan. 2013.

[126] H. Jin, K. Chin, W. Che, C. Chang, H. Li, and Q. Xue, "Differential-fed patch antenna arrays with low cross polarization and wide bandwidths," *IEEE Antennas and Wireless Propagation Letters*, vol. 13, pp. 1069–1072, 2014.

[127] A. Bisognin, D. Titz, F. Ferrero, C. Luxey, G. Jacquemod, R. Pilard, F. Gianesello, D. Gloria, and P. Brachat, "Differential feeding technique for mm-wave series-fed antenna-array," *Electronics Letters*, vol. 49, no. 15, pp. 918–919, July 2013.

[128] H. Jin, W. Che, K. Chin, G. Shen, W. Yang, and Q. Xue, "60-GHz ltcc differential-fed patch antenna array with high gain by using soft-surface structures," *IEEE Transactions on Antennas and Propagation*, vol. 65, no. 1, pp. 206–216, Jan 2017.

[129] S. Liao, P. Wu, K. M. Shum, and Q. Xue, "Differentially fed planar aperture antenna with high gain and wide bandwidth for millimeter-wave application," *IEEE Transactions on Antennas and Propagation*, vol. 63, no. 3, pp. 966–977, March 2015.

[130] D. J. Bisharat, S. Liao, and Q. Xue, "High gain and low cost differentially fed circularly polarized planar aperture antenna for broadband millimeter-wave applications," *IEEE Transactions on Antennas and Propagation*, vol. 64, no. 1, pp. 33–42, Jan 2016.

[131] A. Vosoogh, P. S. Kildal, and V. Vassilev, "Wideband and high-gain corporate-fed gap waveguide slot array antenna with etsi class ii radiation pattern in v -band," *IEEE Transactions on Antennas and Propagation*, vol. 65, no. 4, pp. 1823–1831, Apr. 2017.

[132] A. U. Zaman and P. S. Kildal, "Wide-band slot antenna arrays with single-layer corporate-feed network in ridge gap waveguide technology," *IEEE Transactions on Antennas and Propagation*, vol. 62, no. 6, pp. 2992–3001, Jun. 2014.

[133] J. Liu, A. Vosoogh, A. U. Zaman, and J. Yang, "Design and fabrication of a high-gain 60-GHz cavity-backed slot antenna array fed by inverted microstrip gap waveguide," *IEEE Transactions on Antennas and Propagation*, vol. 65, no. 4, pp. 2117–2122, April 2017.

[134] E. Pucci, E. Rajo-Iglesias, J. L. Vázquez-Roy, and P. S. Kildal, "Planar dual-mode horn array with corporate-feed network in inverted microstrip gap waveguide," *IEEE Transactions on Antennas and Propagation*, vol. 62, no. 7, pp. 3534–3542, July 2014.

[135] A. Vosoogh, A. A. Brazález, and P. S. Kildal, "A v-band inverted microstrip gap waveguide end-coupled bandpass filter," *IEEE Microwave and Wireless Components Letters*, vol. 26, no. 4, pp. 261–263, April 2016.

[136] S. M. Sifat, M. M. M. Ali, S. I. Shams, and A. Sebak, "High gain bow-tie slot antenna array loaded with grooves based on printed ridge gap waveguide technology," *IEEE Access*, vol. 7, pp. 36 177–36 185, Mar. 2019.

[137] J. S. Chieh, B. Pham, A. Pham, G. Kannell, and A. Pidwerbetsky, "Millimeter-wave dual-polarized high-isolation antennas and arrays on organic substrates," *IEEE Transactions on Antennas and Propagation*, vol. 61, no. 12, pp. 5948–5957, Dec 2013.

[138] Z. Chen, H. Liu, J. Yu, and X. Chen, "High gain, broadband and dual-polarized substrate integrated waveguide cavity-backed slot antenna array for 60 GHz band," *IEEE Access*, vol. 6, pp. 31 012–31 022, 2018.

[139] M. Ferrando-Rocher, A. U. Zaman, J. Yang, and A. Valero-Nogueira, "A dual-polarized slotted-waveguide antenna based on gap waveguide technology," in *2017 11th European Conference on Antennas and Propagation (EUCAP)*, March 2017, pp. 3726–3727.

[140] M. Ferrando-Rocher, J. I. Herranz-Herruzo, A. Valero-Nogueira, B. Bernardo-Clemente, A. U. Zaman, and J. Yang, "8×8 ka-band dual-polarized array antenna based on gap waveguide technology," *IEEE Transactions on Antennas and Propagation*, pp. 1–1, 2019.

[141] CST Microwave Studio, "Computer simulation technology 2017."

[142] C. G. Montgomery and M. E. H. Robert, *Principles of microwave circuits*. London, U.K. : Peter Peregrinus on behalf of the Institution of Electrical Engineers, 1987.

[143] K.-L. Chan, F. A. Alhargan, and S. R. Judah, "A quadrature-hybrid design using a four-port elliptic patch," *IEEE Transactions on Microwave Theory and Techniques*, vol. 45, no. 2, pp. 307–310, Feb. 1997.

[144] S. I. Shams and A. A. Kishk, "Double cone ultra wide band unit cell in ridge gap waveguides," in *2014 IEEE Antennas and Propagation Society International Symposium (APSURSI)*, 2014, pp. 1768–1769.

[145] S. I. Shams and A. A. Kishk, "Ridge gap waveguide to microstrip line transition with perforated substrate," in *2014 USNC-URSI Radio Science Meeting (Joint with AP-S Symposium)*, 2014, pp. 215–215.

[146] M. M. M. Ali and S. I. Shams and A. Sebak, "Low loss and ultra flat rectangular waveguide harmonic coupler," *IEEE Access*, vol. 6, pp. 38 736–38 744, Aug. 2018.

[147] M. M. M. Ali and S. I. Shams and A. Sebak and A. A. Kishk, "Rectangular waveguide cross-guide couplers: Accurate model for full-band operation," *IEEE Microwave and Wireless Components Letters*, vol. 28, no. 7, pp. 561–563, Jul. 2018.

[148] S. I. Shams, M. Elsaadany, G. Saad, and A. A. Kishk, "Compact wideband dual loop coupler with high power handling capability for radar applications," *IEEE Microwave and Wireless Components Letters*, vol. 27, no. 10, pp. 900–902, Oct. 2017.

[149] M. M. M. Ali, Islam Afifi and A. Sebak, "Design of compact hybrid directional coupler based on printed RGW technology," *Submitted in Journal of Infrared, Millimeter, and Terahertz Waves*, 2019.

[150] I. Afifi and M. M. M. Ali and A. R. Sebak, "Analysis and design of a 30 GHz printed ridge gap ring-crossover," in *2019 USNC-URSI Radio Science Meeting (Joint with AP-S Symposium)*, Jul. 2019, pp. 65–66.

[151] M. M. M. Ali, I. Afifi and A. R. Sebak, "Design of printed RGW crossover for millimeter wave beam switching network," in *2019 USNC-URSI Radio Science Meeting (Joint with AP-S Symposium)*, Jul. 2019, pp. 63–64.

[152] W. El-Halwagy, R. Mirzavand, J. Melzer, M. Hossain, and P. Mousavi, "Investigation of wideband substrate-integrated vertically-polarized electric dipole antenna and arrays for mm-wave 5G mobile devices," *IEEE Access*, vol. 6, pp. 2145–2157, 2018.

[153] W. Hong, K. Baek, and S. Ko, "Millimeter-wave 5G antennas for smartphones: Overview and experimental demonstration," *IEEE Transactions on Antennas and Propagation*, vol. 65, no. 12, pp. 6250–6261, Dec 2017.

[154] E. Pucci, E. Rajo-Iglesias, and P. S. Kildal, "New microstrip gap waveguide on mushroom-type ebg for packaging of microwave components," *IEEE Microwave and Wireless Components Letters*, vol. 22, no. 3, pp. 129–131, 2012.

[155] H. Raza, J. Yang, P. S. Kildal, and E. A. Alos, "Microstrip-ridge gap waveguide:study of losses, bends, and transition to wr-15," *IEEE Transactions on Microwave Theory and Techniques*, vol. 62, no. 9, pp. 1943–1952, Sept. 2014.

[156] A. B. Guntupalli and K. Wu, "60-GHz circularly polarized antenna array made in low-cost fabrication process," *IEEE Antennas and Wireless Propagation Letters*, vol. 13, pp. 864–867, 2014.

[157] D. Guan, Y. Zhang, Z. Qian, and J. Zhang, "Compact circular polarised SIW array antenna with high gain and conical-beam," *Electronics Letters*, vol. 51, no. 24, pp. 1962–1964, 2015.

[158] B. Y. Toh, R. Cahill, and V. F. Fusco, "Understanding and measuring circular polarization," *IEEE Transactions on Education*, vol. 46, no. 3, pp. 313–318, Aug 2003.

[159] R. Głogowski, J. Zürcher, C. Peixeiro, and J. R. Mosig, "A low-loss planar ka-band antenna subarray for space applications," *IEEE Transactions on Antennas and Propagation*, vol. 61, no. 9, pp. 4549–4557, Sep. 2013.

[160] J. Wu, Y. J. Cheng, and Y. Fan, "Millimeter-wave wideband high-efficiency circularly polarized planar array antenna," *IEEE Transactions on Antennas and Propagation*, vol. 64, no. 2, pp. 535–542, Feb 2016.

[161] B. Zhang, Y. P. Zhang, D. Titz, F. Ferrero, and C. Luxey, "A circularly-polarized array antenna using linearly-polarized sub grid arrays for highly-integrated 60-GHz radio," *IEEE Transactions on Antennas and Propagation*, vol. 61, no. 1, pp. 436–439, Jan 2013.

[162] Z. Zhao, Y. Cui, and R. Li, "A simple circularly polarlized antenna array for millimeter-wave applications," in *2017 International Symposium on Antennas and Propagation (ISAP)*, Oct 2017, pp. 1–2.

[163] J. Xi, B. Cao, H. Wang, and Y. Huang, "A novel 77 GHz circular polarization slot antenna using ridge gap waveguide technology," in *2015 Asia-Pacific Microwave Conference (APMC)*, vol. 3, Dec 2015, pp. 1–3.

[164] A. Chlavin, "A new antenna feed having equal E -and H-plane patterns," *Transactions of the IRE Professional Group on Antennas and Propagation*, vol. 2, no. 3, pp. 113–119, July 1954.

[165] A. Clavin, "An improved element for use in array antennas," in *1975 5th European Microwave Conference*, Sep. 1975, pp. 97–101.

[166] K. Luk and H. Wong, "A new wideband unidirectional antenna element," *Int J Microwave Opt Technol*, vol. 1, 01 2006.

[167] D. Z. Xujun Yang, Lei Ge and C.-Y.-D. Sim, "Magnetoelectric dipole antenna with dual polarization and high isolation," *Wireless Communications and Mobile Computing*, no. 12, pp. 1–7, Apr. 2013.

[168] B. Q. Wu and K. Luk, "A broadband dual-polarized magneto-electric dipole antenna with simple feeds," *IEEE Antennas and Wireless Propagation Letters*, vol. 8, pp. 60–63, 2009.

[169] D. Pozar, *Microwave Engineering*. Wiley, 1997.

[170] M. E. de Cos and F. Las-Heras, "Novel flexible artificial magnetic conductor," *International Journal of Antennas and Propagation*, vol. 1, pp. 1–7, 2012.

[171] P. P. de la Torre, J. Fernández, and M. Sierra-Castañer, "Characterization of artificial magnetic conductor strips for parallel plate planar antennas," *Microwave and Optical Technology Letters*, vol. 50, no. 2, pp. 498–504, 2008.

[172] D. Sievenpiper, Lijun Zhang, R. F. J. Broas, N. G. Alexopolous, and E. Yablonovitch, "High-impedance electromagnetic surfaces with a forbidden frequency band," *IEEE Transactions on Microwave Theory and Techniques*, vol. 47, no. 11, pp. 2059–2074, Nov 1999.

List of Publications

Journal Papers

1. **Mohamed Mamdouh M. Ali**, Islam Afifi, and Abdel-Razik Sebak, "A Dual Polarized Magneto-Electric Dipole Antenna Based on Printed Ridge Gap Waveguide Technology," *Accepted in IEEE Transactions on Antennas and Propagation*, April. 2020.

2. **Mohamed Mamdouh M. Ali** , Shoukry I. Shams and Abdelrazik Sebak, "Ultra-wideband printed ridge gap waveguide hybrid directional coupler for millimetre wave applications," in *IET Microwaves, Antennas and Propagation*, vol. 13, no. 8, pp. 1181-1187, 2019.

3. Syed M. Sifat , **Mohamed Mamdouh M. Ali** And Shoukry I. Shams and Abdel-Razik Sebak, "High Gain Bow-Tie Slot Antenna Array Loaded With Grooves Based on Printed Ridge Gap Waveguide Technology," in *IEEE Access*, vol. 7, pp. 36177-36185, 2019.

4. **Mohamed Mamdouh M. Ali** and Abdelrazik Sebak, "Printed RGW Circularly Polarized Differential Feeding Antenna Array for 5G Communications," in *IEEE Transactions on Antennas and Propagation*, vol. 67, no. 5, pp. 3151-3160, May 2019.

5. Islam Afifi, **Mohamed Mamdouh M. Ali** and Abdel-Razik Sebak, "Analysis and Design of a Wideband Coaxial Transition to Metal and Printed Ridge Gap Waveguide," in *IEEE Access*, vol. 6, pp. 70698-70706, 2018.

6. **Mohamed Mamdouh M. Ali** and Abdel-Razik Sebak, "2-D Scanning Magneto-electric Dipole Antenna Array Fed by RGW Butler Matrix," in *IEEE Transactions on Antennas and Propagation*, vol. 66, no. 11, pp. 6313-6321, Nov. 2018.

7. **Mohamed Mamdouh M. Ali** , Shoukry I. Shams and Abdel-razik Sebak, "Low

Loss and Ultra Flat Rectangular Waveguide Harmonic Coupler," in *IEEE Access*, vol. 6, pp. 38736-38744, 2018.

8. **Mohamed Mamdouh M. Ali** , Shoukry I. Shams and Abdel-Razik Sebak, "Printed Ridge Gap Waveguide 3-dB Coupler: Analysis and Design Procedure," in *IEEE Access*, vol. 6, pp. 8501-8509, 2018.

9. **Mohamed Mamdouh M. Ali** ,Shoukry I. Shams , Abdelrazik Sebak, and Ahmed A. Kishk, "Rectangular Waveguide Cross-Guide Couplers: Accurate Model for Full-Band Operation," in *IEEE Microwave and Wireless Components Letters*, vol. 28, no. 7, pp. 561-563, July 2018.

10. **Mohamed Mamdouh M. Ali** and Abdel-Razik Sebak, "Compact Printed Ridge Gap Waveguide Crossover for Future 5G Wireless Communication System," in *IEEE Microwave and Wireless Components Letters*, vol. 28, no. 7, pp. 549-551, July 2018.

11. Mohammed Akbari, **Mohamed Mamdouh M. Ali**, Mohammadmahdi Farahani , Abdel-Razik Sebak and Tayeb A. Denidni, "Spatially mutual coupling reduction between CP-MIMO antennas using FSS superstrate," in *Electronics Letters*, vol. 53, no. 8, pp. 516-518, 13 4 2017.

Conference Papers

1. Shoukry I. Shams, **Mohamed Mamdouh M. Ali**, Mahmoud Elsaadany, Ghyslain Gagnon, A. M. M. A. Allam, Diaa E. Fawzy and A. R. Sebak, "Interfacing Wideband Amplifiers using Ridge Gap Waveguide for mm-Wave Systems," *International Conference On Electrical And Electronics Engineering (ICEEE2020)*, Antalya, Turkey, April. 2020.

2. Mahmoud Elsaadany, **Mohamed Mamdouh M. Ali**, Shoukry I. Shams , Ghyslain Gagnon, A. M. M. A. Allam, Diaa E. Fawzy and A. R. Sebak, "On the Design of Reconfigurable Wideband Ridge Gap Waveguide Amplifier Modules," *International Conference On Electrical And Electronics Engineering (ICEEE2020)*, Antalya, Turkey, April. 2020.

3. **Mohamed Mamdouh M. Ali**, Shoukry Shams, Mahmoud Elsaadany, Abdelrazik Sebak,"Printed RGW 3-dB Backward Coupler for Millimeter Wave Applications," *in 2020 IEEE International Symposium on Antennas and Propagation and North American Radio Science Meeting in Montreal*, Quebec, Canada, July 2020.

4. **Mohamed Mamdouh M. Ali**, Shoukry Shams, Mahmoud Elsaadany, Abdelrazik Sebak,"Full Band Dielectric Loaded Hybrid Coupler Based on Printed RGW Technology," *in 2020 IEEE International Symposium on Antennas and Propagation and North American Radio Science Meeting in Montreal*, Quebec, Canada, July 2020.

5. Osama Haraz, Waleed Saad, **Mohamed Mamdouh M. Ali**, Abdel-Razik Sebak,"On the Diversity Combining Techniques of MIMO Channel in Wireless Communications," *in 2020 IEEE International Symposium on Antennas and Propagation and North American Radio Science Meeting in Montreal*, Quebec, Canada, July 2020.

6. Osama Haraz, Mohamed Mamdouh, Abdel-Razik Sebak,"Millimeter-Wave PRGW ME Dipole Antenna with Surface Mounted Conical Horn," *in 2020 IEEE International Symposium on Antennas and Propagation and North American Radio Science Meeting in Montreal*, Quebec, Canada, July 2020.

7. I. Afifi, **Mohamed Mamdouh M. Ali**and A. R. Sebak, "Analysis and design of a 30 GHz printed ridge gap Ring-crossover," *2019 USNC-URSI Radio Science Meeting (Joint with AP-S Symposium)*, Atlanta, GA, USA, 2019, pp. 65-66.

8. **Mohamed Mamdouh M. Ali**, I. Afifi and A. R. Sebak, "Design of Printed RGW Crossover for Millimeter Wave Beam Switching Network," *2019 USNC-URSI Radio Science Meeting (Joint with AP-S Symposium)*, Atlanta, GA, USA, 2019, pp. 63-64.

9. **Mohamed Mamdouh M. Ali** , Shoukry I. Shams and Abdel-Razik Sebak, "Reconfigurable Antenna Based on Printed Ridge Gap Waveguide Technology," *2018 18th International Symposium on Antenna Technology and Applied Electromagnetics (ANTEM)*, Waterloo, ON, 2018, pp. 1-2.

10. Shoukry I. Shams, **Mohamed Mamdouh M. Ali** and Abdel-Razik Sebak., "Reconfigurable Guiding Structure Based on Printed Ridge Gap Waveguide Technol-

ogy," *2018 18th International Symposium on Antenna Technology and Applied Electromagnetics (ANTEM)*, Waterloo, ON, 2018, pp. 1-2.

11. Islam Afifi, **Mohamed Mamdouh M. Ali** and Abdel-Razik Sebak, "Wideband Printed Ridge Gap Semi-Log Periodic Structure Antenna for Millimeter Wave Applications," *2018 18th International Symposium on Antenna Technology and Applied Electromagnetics (ANTEM)*, Waterloo, ON, 2018, pp. 1-2.

12. **Mohamed Mamdouh M. Ali** and Abdel-Razik Sebak, "Directive antennas for future 5G mobile wireless communications," *2017 XXXIInd General Assembly and Scientific Symposium of the International Union of Radio Science (URSI GASS)*, Montreal, QC, 2017, pp. 1-4.

13. **Mohamed Mamdouh M. Ali** and Abdel-Razik Sebak, "4×2-slot element for 30-GHz planar array antenna realized using SIW cavity and fed by microstrip line line-ridge gap waveguide," *2017 IEEE International Symposium on Antennas and Propagation and USNC/URSI National Radio Science Meeting*, San Diego, CA, 2017, pp. 2149-2150.

14. **Mohamed Mamdouh M. Ali** and Abdel-Razik Sebak, "Dual band (28/38 GHz) CPW slot directive antenna for future 5G cellular applications," *2016 IEEE International Symposium on Antennas and Propagation (APSURSI)*, Fajardo, 2016, pp. 399-400.

15. **Mohamed Mamdouh M. Ali** and Abdel-Razik Sebak, "Design of compact millimeter wave massive MIMO dual-band (28/38 GHz) antenna array for future 5G communication systems," *2016 17th International Symposium on Antenna Technology and Applied Electromagnetics (ANTEM)*, Montreal, QC, 2016, pp. 1-2.

16. **Mohamed Mamdouh M. Ali** , Osama Haraz , Saleh Alshebeili and Abdel-Razik Sebak, "Broadband printed slot antenna for the fifth generation (5G) mobile and wireless communications," *2016 17th International Symposium on Antenna Technology and Applied Electromagnetics (ANTEM)*, Montreal, QC, 2016, pp. 1-2.

17. **Mohamed Mamdouh M. Ali** and Abdel-Razik Sebak, "Compact UWB high gain fermi taper slot antenna for future 5G communication systems," *2016 17th Interna-*

tional Symposium on Antenna Technology and Applied Electromagnetics (ANTEM), Montreal, QC, 2016, pp. 1-2.